Impact of Climate Variability and Weather Extremes on Terrestrial and Aquatic Systems

By

Atefeh Hosseini

M.S., University of Nebraska-Lincoln, 2012
B.S., Allameh Mohaddes Nouri University, 2002

Submitted to the graduate degree program in Department of Civil, Environmental, and Architectural Engineering and the Graduate Faculty of the University of Kansas in partial fulfillment of the requirements for the degree of Doctor of Philosophy.

Chair: Joshua Roundy

Ted Harris

Edward Peltier

Admin Husic

Amy Hansen

Nathaniel Brunsell

Date Defended: July 18, 2023

The dissertation committee for Atefeh Hosseini certifies that this is the approved version of the following dissertation:

Impact of Climate Variability and Weather Extremes on Terrestrial and Aquatic Systems

Chair: Joshua Roundy

Date Accepted: August 25, 2023

Abstract

Inland freshwater ecosystems have been experiencing rapid and notable transformations in direct response to both climate shifts and human-induced stressors during recent decades. Land Surface Models (LSMs) play a vital role in providing information on various aspects of the Earth's surface, including hydrological processes, biophysical characteristics, and biogeochemical dynamics. Over time, LSMs have evolved from simplified depictions of land surface biophysics to incorporate a diverse range of interrelated processes, including modified vegetation dynamics, groundwater interactions, and hydrological processes. Given the profound impact of hydrological processes on a multitude of biophysical and biogeochemical mechanisms within the Earth system, the inclusion of lakes and human-made reservoirs in land surface models (LSMs) is currently in its nascent stages. To enhance our understanding of the impact of hydrometeorological changes on water quality and to address the limitations in representing inland water bodies within Land Surface Models (LSMs), three research studies were conducted. These studies employed the Noah land surface model (Noah-MP) with multiple parameterization options and the General Lake Model (GLM); models were used individually and in combination. In the first study, the influence of vegetation dynamics is thoroughly examined, with specific attention given to six different configurations of leaf area index (LAI) and vegetation fraction (FVEG) and the impact on streamflow. The main objective was to evaluate how these configurations impact the representation of eco-hydrological processes in a semi-arid region primarily characterized by grasslands. Additionally, the study aims to analyze the performance of streamflow simulation and the capability to predict drought conditions at scales beyond the site level. The results indicate that the incoming net radiation plays a crucial role in constraining the total evaporation process in energy-limited environments. It was observed that an overestimation of latent heat (LE) led to an underestimation of streamflow. Furthermore, the analysis indicated that all of the newer version (Noah-MP 4.0.1) vegetation physics demonstrated a higher degree of accuracy in reproducing spatial patterns of drought compared to the older version 3.6. These findings are then used to select the optimal Noah-MP model configuration which is used in the last chapter. The second study focused on quantifying the impact of atmospheric stilling on polymictic reservoirs, aiming to enhance predictions of the phytoplankton community composition. High-resolution temporal in-situ data from Marion Reservoir in Kansas were employed to identify the biotic and abiotic factors that influence the composition and dynamics of phytoplankton in shallow reservoirs. The study revealed that a combination of rising air temperatures, calm weather conditions, and light penetration depth emerged as the primary drivers responsible for triggering algal blooms. Additionally, the internal nutrient loading during anoxic conditions was found to have a direct impact on the intensification of harmful cyanobacterial blooms (CyanoHABs). The last chapter then focuses on the integration of the General Lake Model (GLM) with a Noah-MP to improve the prediction of lake thermodynamic patterns, particularly in shallow lakes and reservoirs. Remarkably, the simulation of lake thermal dynamics, driven by the forcings from the North American Land Data Assimilation System-2 (NLDAS-2) and incorporating modeled surface runoff from Noah-MP, exhibited a capacity to reproduce reservoir thermal regimes that surpassed field measurements, albeit marginally. Overall, this dissertation offers a thorough assessment of the performance of the state-of-the-art land surface model, Noah-MP, providing valuable insights into the integration of the GLM within this framework at Marion Reservoir in Kansas.

Acknowledgments

I would like to express my deepest gratitude to my Ph.D. advisor, Dr. Joshua Roundy, and my co-advisor, Dr. Ted Harris. Without their unwavering guidance, invaluable expertise, and continuous support, this work would not have been possible. I am immensely thankful to my committee members: Dr. Nathaniel Brunsell, Dr. Edward Peltier, Dr. Admin Husic, and Dr. Ar. Amy Hansen. Their diligent review of my work, insightful feedback, and constructive suggestions have played a pivotal role in refining the quality and depth of this research. I would like to extend a special acknowledgment to David Mocko from the Hydrological Sciences Laboratory of NASA Goddard Space Flight Center. His exceptional assistance in implementing the new vegetation component in the Noah-MP model has significantly contributed to the advancement of this study.

Some individuals not only help you in achieving your academic goals but also become mentors in your life, and Dr. Gabriel Katul and Dr. Wilfred Konrad are prime examples. I am immensely grateful for their invaluable guidance throughout these years.

I extend my appreciation to Dr. Jude Kasten for generously providing us with bathymetric data. The inclusion of this data has significantly enriched the analysis and findings of our research, enhancing its overall quality and depth. Further, there are so many people at the Kansas Biological Survey and Center for Ecological Research who helped me in field data collection and laboratory analysis: Debbie Baker, Don Huggins, Javier Omar Morales, Karah M. Kniola, Rebecca Kessler, Adeline Kelly, Luke Ungerer, and Logan Hagan-McAnany. Two parts of this thesis (Chapters 3 and 4) were funded by a grant from the Kansas Department of Health and Environment (KDHE). The opportunities offered by KDHE helped me gain a wider understanding of the reservoir water cycle and lake ecology.

I would like to extend my sincere appreciation to Dr. Yuqi Zhang, my fellow Ph.D. student, for her collaborative spirit throughout this academic journey. Together, we navigated the challenges of research, providing mutual encouragement and motivation.

Last, but certainly not least, I would like to express my deepest gratitude to my family members, both in remembrance and to those who remain my unwavering support on this earthly path. I also extend my heartfelt appreciation to my friends scattered across the globe, whose unwavering spiritual support, encouragement, and belief in my abilities have consistently served as the wellspring of strength and inspiration propelling me through this arduous academic expedition.

Table of Contents

List of Figures

List of Tables

Chapter 1: Introduction

Understanding the intricate ways in which climate and climate change affect living systems relies heavily on accurately representing land surface processes in models, encompassing both terrestrial and aquatic systems. The complex and interrelated nature of processes, such as dynamic vegetation distributions, soil moisture dynamics, and surface hydrological processes, has continuously evolved from their initial simplistic biophysical configurations to meet the diverse and wide-ranging needs of user communities (Fisher and Koven 2020). Accurate real-time water quality prediction plays a crucial role in empowering local environmental managers to effectively handle upcoming events and emergencies. Providing timely and precise information enables them to develop and implement the best management practices necessary to safeguard the environment and mitigate potential risks (Sha et al. 2021). Natural lakes and man-made reservoirs hold more than 87 percent of inland freshwater (Gleick, 1993). However, their complex dynamics are often simplified or overlooked in land surface models, which can limit our understanding of the intricate interactions between water bodies and the surrounding environment.

The integration of reservoirs into land surface models represents a significant advancement that enhances our capacity to simulate ungauged reservoirs worldwide. This integration provides a valuable opportunity to deepen our understanding of the historical dynamics of water resource systems and to improve the assessment and prediction of their future vulnerability to climate and environmental changes.

1.1 Objectives and Research Questions

My dissertation is driven by the overarching objective of integrating the General Lake Model (GLM) into the Noah-MP framework to provide a tool for real-time forecasting of Kansas lake conditions. This objective is broken up into three underlying objectives each with its own set of research questions as follows:

1.1.1 *Objective 1*: Quantify the impact of vegetation configuration on the hydrologic prediction within Noah-MP

- Which Noah-MP vegetation configurations provide the best representation of eco-hydrological processes (e.g. energy, water, and carbon fluxes) in a semi-arid grassland-dominated region?
- Do the differences in vegetation configuration within Noah-Mp change its ability to predict drought at the site-level and regional scale?

1.1.2 *Objective* 2: Analysis of hydrodynamic and biological behaviors of eutrophic reservoir

- How does the water column stability impact physical and chemical variables (e.g., thermocline depth, light availability, and water column nutrient concentrations)?
- Which biotic and abiotic factors trigger phytoplankton composition and dynamics in shallow reservoirs?

1.1.3 *Objective* 3: Role of input drivers in simulation of shallow inland aquatic systems

- To what extent is GLM capable of accurately reproducing the water balance and thermodynamics of lakes, particularly in the context of shallow lakes characterized by substantial variations in water stages, when crucial forcing data and inflow measurements are unavailable?

To accomplish this goal, I adopted a comprehensive approach that incorporated process-based models, meticulous collection of high temporal resolution data, and advanced statistical analysis for quantifying uncertainty.

This dissertation represents the first attempt to integrate the widely-used General Lake Model (GLM) with the Noah-MP land surface model (LSM) in the state of Kansas. The first objective was to evaluate different configurations of the Noah-MP model, incorporating leaf area index (LAI) and vegetated fraction (FVEG) options. This evaluation was conducted using Eddy Covariance (EC) measurements collected between 2008 and 2018 from two instrumented grassland sites located in Kansas. After identifying the Noah-MP configuration that produced the most accurate representation of simulated streamflow within the designated domain, we then employed the selected Noah-MP version to generate the required streamflow inputs for running the GLM model. Marion Reservoir, a well-monitored hypereutrophic discontinuous polymictic waterbody in central Kansas, was chosen as the focal point of my intensive two-year (2021-2022) study. First, I investigated the impact of key meteorological factors on the thermal and dissolved oxygen (DO) cycles within the lake. Through this research, I utilized high-frequency measurements to gain a comprehensive understanding of how water column mixing influences the dynamics of dissolved oxygen (DO), nutrients, and metals and subsequently affects the emergence and propagation of harmful cyanobacterial algal blooms (CyanoHABs). Following initial investigations, I proceeded to run GLM using two distinct forcing drivers and inflow data. The first model run involved utilizing measured forcing and inflow data provided by the United States

Army Corps of Engineers (USACE). In the second simulation, I employed forcing drivers obtained from NLDAS-2 and Noah-MP simulated streamflow data.

1.2 Scope of Dissertation Chapters

This dissertation is structured into five chapters. Chapter 2 presents an in-depth analysis investigating the influence of vegetation phenology on the simulation of energy, water, and carbon fluxes in a semi-arid grassland-dominated region. This analysis entails utilizing different versions of the Noah-MP model, each characterized by variations in Leaf Area Index (LAI) and Fraction of Vegetation (FVEG) options. The chapter also aims to evaluate the capability of each model configuration in distinguishing drought coverage beyond the local site level and assess their ability to accurately capture the magnitude of surface runoff. Chapter 3 then investigates alterations in the physical conditions of the lake, such as water temperature, dissolved oxygen (DO), thermal stratification, water balance, and mixing behavior using field measurements obtained from two intensive sampling campaigns conducted in 2021 and 2022. Furthermore, it offers detailed insights into the emergence and intensification of cyanobacteria blooms within Marion Reservoir, located in central Kansas. In Chapter 4, GLM simulations are conducted by utilizing both measured and modeled inputs to assess the accuracy of the model to represent lake hydrodynamic processes, including water balance and thermal stratification. These evaluations are carried out under two distinct input scenarios, with the additional aim of replicating complex patterns and fluctuations in water temperatures, even in situations where essential meteorological and stream flow field measurements are unavailable. Lastly, Chapter 5 synthesizes the outcomes of this thesis and gives an outlook for future research. Each chapter is formatted as a journal article complete with an introduction, material and methods, results, conclusion, and discussions.

Chapter 2: Understanding the Impact of Vegetation Dynamics on the Water Cycle in the Noah-MP Model

Hosseini, A., Mocko, D.M., Brunsell, N.A., Kumar, S.V., Mahanama, S., Arsenault, K. and Roundy, J.K., 2022. Understanding the impact of vegetation dynamics on the water cycle in the Noah-MP model. Frontiers in Water, 4, p.925852.

2.1 Abstract

The impact of extreme climate events, especially prolonged drought, on ecosystem response, can influence the land-atmosphere interactions and modify local and regional weather and climate. To investigate the impact of vegetation dynamics on the simulation of energy, water, and carbon exchange at the land surface and streamflow, especially during drought conditions, we compared the performance of multiple versions of the Noah-Multiphysics land surface model (both Noah-MP LSM, version 3.6 and 4.0.1) with default configurations as well as various vegetation physics options, including dynamic or input leaf area index (LAI) and the fractional vegetated area (FVEG). At the site level, simulated water and energy fluxes from each version were compared to flux tower (EC) measurements and remote sensing data from Moderate-Resolution Imaging Spectroradiometer (MODIS) at well-characterized natural grassland sites in Kansas from 2008 to 2018. The ability of each version to reproduce annual mean river flows was compared to gauged observations at USGS stations over 11 years (2008-2018). Model performance in replicating spatial patterns during extreme events was assessed by comparing simulated soil moisture (SM) percentiles over the state of Kansas to the U.S. Drought Monitor (USDM). Results from these comparisons indicate that: (a) even though there were differences in the Latent Heat (LE) components (i.e., transpiration, canopy evaporation, and soil evaporation), the total LE is mostly insensitive to variations in LAI across all model versions. This indicates that the incoming net radiation limits the total evaporation as the presence of adequate soil moisture allows for higher

soil evaporation when LAI limits the transpiration. (b) regardless of the model version, the precipitation forcing largely dictates the accuracy of evapotranspiration simulation; (c) Overestimation of LE resulted in underestimation of streamflow, particularly over land surface type dominated by a combination of grasses and cropland in the western and central part of the state (e) all of the tested Noah-MP 4.0.1 vegetation physics produced spatial patterns of drought that more closely matched the USDM as compared to version 3.6. These findings have important relevance for applications of large-scale ecosystem-atmosphere feedback in water, carbon, and energy exchange.

2.2 Introduction

Monitoring the impacts of climate change and anthropogenic activities on terrestrial hydrology requires analyzing and predicting the patterns of water supply and carbon sequestration along with underlying surface perturbations and changes in moisture and heat budgets. Evapotranspiration (ET) as a key component of the hydrological cycle is responsible for approximately more than 60 percent of the precipitation received by the land surface (Jasechko et al., 2013; Z. Wei et al., 2017). Transpiration from plants makes up a key component of terrestrial ET that regulates land-atmosphere interaction through the coupling of the carbon-water cycles and surface energy balance. On a global scale, plant transpiration accounts for more than four-fifths of the entire global evaporation (Schlesinger & Jasechko, 2014). This emphasizes the important role of vegetation in coupling the water and energy cycle within the soil-plant-atmosphere system (Claussen et al., 2013).

With further rises in global and regional temperatures and increased variations in regional precipitation patterns, water availability is a dominant factor that limits evapotranspiration.

Modeling ecosystem behavior using in situ and remotely sensed observations provides a means to identify dominant processes that affect land surface-climate interactions in terms of heat, water, and carbon exchanges. Land surface models (LSMs), such as the Noah Multi-Parameterization options (Noah-MP), provide a framework to develop a process-level understanding of the interactions across the surface-atmosphere interface at various spatio-temporal resolutions (Niu et al., 2011). The Noah-MP model was built as an improved version of the earlier Noah model (Ek et al., 2003). Several studies (Gao et al., 2015; Gayler et al., 2014; Yang et al., 2011; Zheng et al., 2015a, 2015b) demonstrated apparent improvements in the simulation of surface fluxes and temperature, groundwater dynamics, and hydrological variables (e.g., soil moisture, snow water equivalent, and runoff) of Noah-MP over the legacy Noah LSM through validations with local and global measurements. Noah-MP is based on mass and energy balance and coupled water and carbon cycles (Cuntz et al., 2016). There are multiple physics options that impact the flux of water and energy to the atmosphere in Noah-MP, such as stomatal conductance, hydrological processes within the canopy and the soil, and canopy radiative transfer. However, the complex interaction between sub-processes like ET and canopy resistance is simplified within the original model which leads to further limitations for LSMs to accurately simulate land-climate interaction at seasonal to inter-decadal time scales, especially during prolonged drought (Ma et al., 2017).

One of the major physical mechanism enhancements in the Noah-MP model is the dynamic vegetation model that allows for the prognostic representation of plant phenology, Leaf Area Index (LAI), and canopy stomatal resistance. Vegetation dynamics in the Noah-MP modeling system include plant photosynthesis, respiration, and partitioning of assimilated carbon among plant parts, including leaves, roots, and wood which can represent seasonal and long-term changes in vegetation phenology and carbon exchanges over the land surface (De Kauwe et al., 2017; Gim et al., 2017; Ise et al., 2010). The incorporation of vegetation dynamic and photosynthesis-based stomatal resistance in the Noah-MP LSM enables the exploration of the carbon partitioning in the plant compartments (e.g., leaves, roots, and stems) and captures a prognostic representation of vegetation growth and senescence via canopy states such as LAI. In addition, Noah-MP allows separation of two-stream radiative transfer treatment through the canopy for representing a 3-dimensional canopy structure that includes Jarvis and Ball-Berry photosynthesis-based stomatal resistance (Ball et al., 1987; G. Collatz et al., 1992; G. J. Collatz et al., 1991). The Ball–Berry stomatal resistance option together with a dynamic vegetation model (Dickinson et al., 1998) simulates carbon partitioning to various parts of vegetation and soil carbon pools. The model can represent the difference between C3 and C4 photosynthesis pathways and defines vegetation class-specific parameters for plant assimilation and respiration (Arsenault et al., 2018; Chang et al., 2020; Niu et al., 2011). Although land memory processes (e.g., a multi-layer snowpack, an unconfined aquifer model for groundwater dynamics, and soil evaporation) have been improved in Noah-MP, the predictive skill of the model is still largely affected by vegetation processes (e.g., components of plant transpiration, an interactive vegetation canopy layer, and evaporation of the canopy interception) (Wei et al., 2010). The influence of these interconnected processes impacts the water budget and surface energy balance equations and an imbalance in one component will affect simulation results in multiple ways.

These errors in representing the water, energy, and carbon cycle in the model may be more pronounced in transitional zones that exhibit sharp changes in precipitation and land cover as the dynamic vegetation and LAI in the model could play a more pivotal role in surface hydrological components like evaporation, soil moisture, and runoff. The objective of this study is to carry out a set of model runs and analyses over the state of Kansas which has a strong east-to-west gradient of precipitation and land cover type. The analysis is broken up into three main parts: (i) Assess the impact of vegetation phenology for different versions of the Noah-MP with various levels of complexity to simulate energy, water, and carbon fluxes in a semi-arid grassland-dominated region; (ii) Evaluate the capability of each model to distinguish drought coverage beyond the site level; (iii) Compare simulated streamflow with United States Geological Survey (USGS) gauge measurements to assess each model version's ability to capture the magnitude of surface runoff and identify possible causes for poor performance in modeled estimates over the domain.

2.3 Data, Models & Methods

2.3.1 Data

This study uses eddy covariance (EC) data collected from two Ameriflux sites located on well-characterized natural grassland sites in northeastern Kansas (Figure 2-1). One site (at the Konza Prairie Biological Station, KON) is located in an annually burned, non-grazed, watershed in an upland topographic area and is dominated by perennial C4 grass species. This location has rocky, thin soils of the Florence series with an average annual precipitation of 870 mm (https://www.neonscience.org/field-sites/konz), approximately 75 percent of which happens during the growing season (April–September) (Brunsell et al., 2017; Logan & Brunsell, 2015). The second site, located at the University of Kansas Field Station (KFS), is a restored prairie that was used extensively as agricultural land between the 1940s and the 1960s and was a hayfield until 1987. Currently, this site contains a mixture of C3 forbs and C4 grasses with a small fraction of woody vegetation and is burned approximately every four years. The site has a mean annual precipitation of 990 (mm) (https://www.neonscience.org/field-sites/ukfs) with soils classified as fine, montmorillonite, mesic aquic argiudolls (Brunsell et al., 2008, 2011, 2013; Kaste et al., 2006).

Both locations are prone to the rapid onset of drought (Roy Chowdhury et al., 2019). Tower measurements at both sites were collected using the eddy covariance technique (Baldocchi et al., 2001). Data were measured at each site from towers at 3 m height above the surface. Three-dimensional wind components, temperature, humidity, and carbon dioxide concentration are collected at 20 Hz using a triaxial sonic anemometer (CSAT-3, Campbell Scientific, Logan UT, USA) and a LiCor infrared gas analyzer (LI-7500, Li-Cor, Lincoln, NE, USA) (Brunsell et al., 2011). Half-hourly data are processed according to Ameriflux standards and are described in these references (Brunsell et al., 2013; De Oliveira et al., 2018), with missing values of the fluxes gap filled following the procedure described in this reference (Reichstein et al., 2005). The REddyProc package (https://github.com/bgctw/REddyProc) is used as a post-processing tool to partition half-hourly net ecosystem exchange (NEE) into the Gross primary production (GPP) and ecosystem respiration. Average daily rainfall measurements at 10 sites across Konza prairie from Long-term ecological research (LTER) data sets (http://www.konza.ksu.edu) and daily precipitation measurements from National Resources Conservation Service (NRCS) (https://websoilsurvey.sc.egov.usda.gov) at KFS site were used as gauge measurements to compare with North American Land Data Assimilation System (NLDAS-2) (Xia et al., 2012) precipitation data.

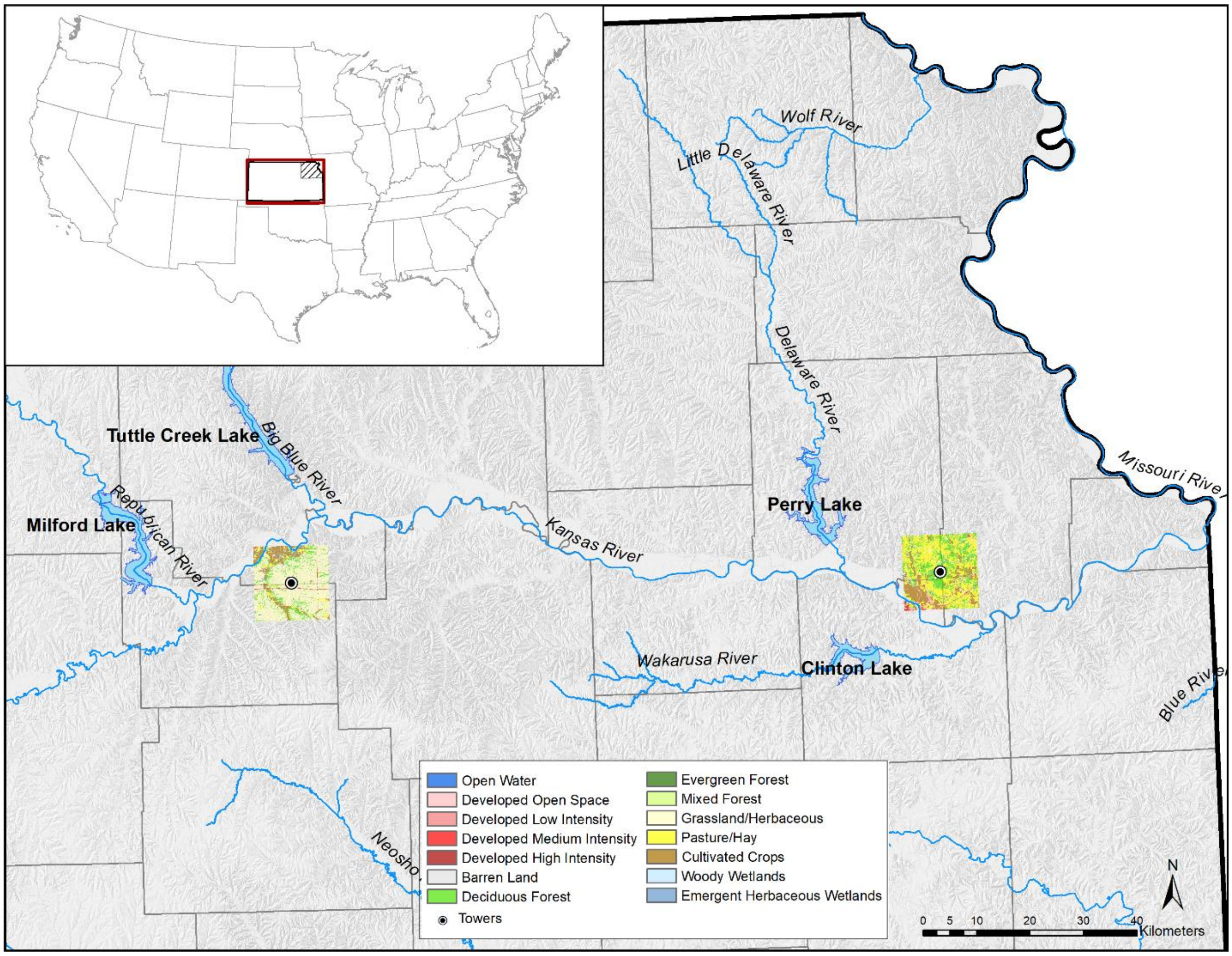

Figure 2-1:
Study area representing Noah-multi parameterization (MP) grid (black square) over the National Land Cover Database (NLCD) around Kansas Field Station (KFS) and Konza Prairie Biological Station (KON) tower locations (black dots). The red rectangular box represents the simulation domain.

In addition to EC data, satellite, and USGS streamflow data are used to evaluate the water-vegetation relationship in the model over a larger spatial area. The satellite estimates of latent heat (LE) from MOD16A2 (Running et al., 2021), GPP product MOD17A2H (Running et al., 2015), and LAI are from collection 6 TERRA/AQUA-MODIS L4 MCD15A2H.006 (Myneni et al., 2015). All of the MODIS variables are retrieved at an 8-day temporal resolution and 500m spatial resolution. The satellite measurements were extracted for the pixel that contains the flux towers for the period 1 January 2008 to 31 December 2018, to compare the MODIS estimates of LE and

GPP against those from the flux tower. We acknowledge that there are several ET estimates developed using models and remote sensing datasets including GLEAM, ALEXI, PT-JPL, etc. All these estimates have uncertainties of their own stemming from modeling and data fusion assumptions and none of these products can be considered a true ET reference. MODIS LE is a widely used product and was selected because the basic measurements are from the same platform as that of LAI used in the model simulations. Observed streamflow from USGS gauges (https://waterdata.usgs.gov) was also used to assess model-simulated streamflow across the model domain. The gauges were screened to only include basins that are entirely within the model domain and have no upstream reservoir operations. This resulted in 31 basins that range from 10 to 4000 km2 drainage areas.

2.3.2 Model Configurations

The Noah-MP model simulations were run using the open-source NASA Land Information System (LIS) (Kumar et al., 2006; Kumar et al., 2019). To test the importance of vegetation dynamics on the water, energy, and carbon fluxes as well as streamflow, we configured six sets of physics options of land-only (uncoupled) Noah-MP with the default set of parameters (each model vegetation configuration summarized in Table 2-1). All six model configurations used the same forcing data from the NLDAS-2. The NLDAS-2 data set includes precipitation (mm/s), downward shortwave and longwave radiation (W/m^2), near-surface air temperature (K), wind (m/s), humidity (kg/kg), and surface pressure (hPa). The NLDAS-2 data set utilizes a combination of ground-based rain gauges, radar, satellite observations, and model-generated precipitation, based on the NCEP North American Regional Reanalysis (NARR); (Mesinger et al., 2006) over the U.S. to produce a high resolution (1-hourly 12.5-km) gridded precipitation and surface meteorological data set. The land cover classification and soil texture types used in this experiment are from the 30 arc-second data of the U.S. Geological Survey (USGS) 24-category vegetation (land use) and the hybrid State Soil Geographic (STATSGO) / Food and Agriculture Organization (FAO) soil texture data sets, respectively, both of which are maintained by the NCAR/RAL (Research Application Laboratory, National Center for Atmospheric Research) (https://ral.ucar.edu/solutions/products/noah-multiparameterization-land-surface-model-noah-mp-lsm). For some configurations, a monthly gridded 0.144-deg FVEG climatology produced by National Oceanic and Atmospheric Administration (NOAA) – National Environmental Satellite, Data, and Information Service (NESDIS) (also available from RAL) was used as input. All model runs span the entire state of Kansas (37°– 40°N, 102°– 95°W) at a spatial resolution of 1/8° grid (∼12.5 km) and an hourly temporal resolution. The soil layer thicknesses in the models consist of four layers with thicknesses of 0.1, 0.3, 0.6, and 1 meter from top to bottom with a total soil depth of 2.0 meters. To avoid the impact of initial conditions (e.g., soil moisture) on water fluxes, energy fluxes, and state variables in the model, a 5.6-year (July 2002 - Dec 2007) spin-up was run for each model version.

Table 2-1*:*

Description of each Noah-MP configuration option used in this study.

Model ID	**Model Version**	**LAI**	**FVEG**
V3-LD-FD	3.6. VegOn	Dynamic	Dynamic (Calculated as a function of the LAI and SAI)
V4-LD-FX	4.0.1. VegOn.Opt 5	Dynamic	Annual Maximum of the Gridded Monthly Climatology
V4-LC-FX	4.0.1. VegOff.Opt 4	Look-up table by month and vegetation class	Annual Maximum of the Gridded Monthly Climatology
V4-LM-FC	4.0.1. VegOff.Opt 7	MODIS	Gridded Monthly Climatology
V4-LM-FD	4.0.1. VegOff.Opt 8	MODIS	Dynamic (Calculated as a function of the LAI and SAI)
V4-LM-FX	4.0.1. VegOff.Opt 9	MODIS	Annual Maximum of the Gridded Monthly Climatology

The gridded runoff and baseflow from the Noah-MP model were used in conjunction with a hydrologic routing model that mimics the movement of water through the natural stream channels, based on topography and stream channel characteristics. The routing model utilized the 30 arcsec (approximately 1 km) HydroSHEDS topography dataset (Lehner et al., 2008) and a slope-adjusted velocity parameterization based on the work of (Gong et al., 2009). Although this routing algorithm only solves for continuity and not momentum, it provides a computationally efficient method that has been utilized in several hydrologic monitoring and forecasting applications (Sheffield et al., 2013; Yuan et al., 2015).

Two important vegetation characteristics within the Noah-MP model are LAI and the greenness FVEG. Within the model, the greenness fraction represents the percentage of the grid that is covered with vegetation and the LAI represents the vertical thickness of the vegetation and therefore the total evaporative surface area. The Noah-MP model simulations differ in the way LAI and FVEG are calculated in the model. The Noah-MP model can be run with dynamic vegetation either off or on. When it is turned on, LAI, Stem Area Index (SAI), and FVEG are predicted from the vegetation model of (Dickinson et al., 1998) with default parameters, and the Ball-Berry (Ball et al., 1987) model is used for stomatal resistance.

To help organize and analyze the different model versions, a three-part naming convention is used (Vx-Lx-Fx) where the first part denotes the model version (Vx), the second part denotes the LAI source (Lx) and the third part denotes the FVEG source (Fx). The Noah-MP model version in this analysis will be version 3.6 (V3) or version 4.0.1 (V4). There are three options for the LAI source which include: dynamically calculated by the model (LD), from a Noah-MP look-up table climatology by month and by vegetation class (LC), and LAI from 8-day MODIS measurements interpolated into a daily input variable (LM). There are also three options for FVEG which include:

dynamically calculated by the model (FD), the monthly climatology input gridded dataset (FC), and the annual maximum of the gridded monthly climatology at each grid point (FX). Using this convention, the V3-LD-FD model run uses version 3.6 with LAI and FVEG from a dynamic simulation of carbon uptake and partitioning. A summary of the six different Noah-MP model versions is given in Table *2-1*. In these runs, V3-LD-FD and V4-LD-FX both use dynamic vegetation to compute LAI and SAI; however, V4-LD-FX does not calculate FVEG but instead uses the annual maximum FVEG from the monthly climatological gridded data. V4-LC-FX does not use dynamic vegetation, instead, LAI is based on the monthly look-up table values and FVEG is based on the annual maximum FVEG from the monthly climatological gridded data. It should be noted that the values of monthly climatology FVEG and the look-up table LAI prescribed for each land use type vary among months but have no interannual variability. Versions V4-LM-FC, V4-LM-FD, and V4-LM-FX use LAI from MODIS real-time data. The difference among these models lies in FVEG configurations. This combination of model simulations will facilitate the assessment of the representation of vegetation in the Noah-MP model and its impact on surface fluxes and streamflow in the model. The simplified representation of the groundwater and runoff option (SIMGM) was used in all configurations.

2.3.3 Methods

Simulation results are compared with eddy covariance (EC) flux measurements of water and energy, time series of soil moisture, and MODIS LAI observations. While ground observations from flux towers (e.g., Ameriflux network) are preferable to satellite-based observations, the absence of field measurements of LAI necessitates a comparison with satellite retrievals of LAI. We aggregated LE, GPP, NEE, and LAI data sets to monthly composites averaged over the entire study period for both model and observations. Due to the focus of this work on the effects of vegetation dynamics on the near-surface flux exchanges, we highlighted the growing season period (from April to September) at both sites. It should be noted that the MODIS LAI input data was upscaled from the finer resolution of the data product (500 m) up to the model resolution (1/8° grid or ~12.5 km) via averaging. Model comparisons with the EC data are made by comparing the model grid cell that covers the tower locations as shown in Figure 2-1. The model performance for LE and GPP fluxes was evaluated and summarized in Taylor diagrams using the Pearson correlation coefficient (r), normalized standard deviations (sd), and root-mean-square error (RMSE).

To quantitatively assess the simulated streamflow with the USGS gauge observations and model outputs for LE with MODIS, the Kling-Gupta efficiency (KGE) was used as a dimensionless performance metric. It is defined as:

$$KGE = 1 - \sqrt{(r-1)^2 + \left(\frac{\mu_s}{\mu_o} - 1\right)^2 + \left(\frac{\sigma_s}{\sigma_o} - 1\right)^2} \qquad \text{(Eq. 1)}$$

where r is the Pearson correlation coefficient, μ, and σ are the mean and standard deviation of the simulated (s) and observed (o) values, respectively. KGE can range between –∞ to 1 with the value equal to one indicating a perfect match between model simulations and observations. The advantage of the KGE is that it accounts for correlation, variability, and bias of simulated time series and equally weights each metric. Compared to traditional fit metrics such as root mean squared error (RMSE) or Nash-Sutcliffe Efficiency (NSE); (Nash & Sutcliffe, 1970), KGE provides more insight into the model skill and the ability to evaluate different components of overall error (Fowler et al., 2018; Ghimire et al., 2020; Gupta et al., 2009). A meaningful benchmark for the KGE is one in which the observed mean is used as a predictor and yields a KGE score of $1 - \sqrt{2} \approx -0.41$ (Knoben et al., 2019). Therefore, in evaluating the streamflow and LE, the benchmark of -0.41 is considered a lower limit (i.e., minimum KGE threshold), and values below that are not directly quantified but considered poor model simulations. To eliminate water resource management effects on the results, reservoirs with storage greater than 10 percent of the mean annual streamflow from the USGS were not considered in the analysis.

To identify drought events across the state of Kansas, two drought events, 2012 and 2018 were selected based on the data archive from the U.S. Drought Monitor (USDM). The event in 2012 was the most severe and widespread drought in Kansas since 1988 in terms of both duration and spatial coverage (Anandhi & Knapp, 2016), while the 2018 drought was milder and less extensive (Chen et al., 2020). In the model, the percentile of the top 1-meter SM (root zone) is used as an indicator of drought-induced water stress. The percentile is calculated as a 30-day moving average for each day of the year using the top 1-m SM with the percentile distribution based on a 14-day moving window centered on the target day over the 11-year simulation period. The US drought monitor was compared to simulated SM based on the following percentiles: greater than 31 is considered no drought, between 21-30 is considered abnormally dry (D0), 11-20 is considered moderate drought (D1), 6-10 is considered severe drought (D2), 3-5 is considered extreme drought (D3) and 0-2 is considered exceptional drought (D4) as in USDM drought severity classification (M. J. Hayes et al., 2012). The model representation of drought is then compared with the weekly USDM maps.

2.4 Results

2.4.1 Overall Model Performance

Site level. The differences in simulated land surface water and carbon fluxes, between the sites, are compared against the tower observations to evaluate the performance of the different model configurations. Comparisons among year-round daily LE and GPP from different model versions at both KON and KFS sites are summarized in the Taylor diagrams where the EC data are used as a reference (Figure 2-2). Overall, there is no significant difference among models in capturing LE at both sites. At KON, LE output from all models falls over the normalized standard deviation of 1 which indicates that all models could regenerate variability in the data compared to the measurements. Whereas at KFS, simulated LE from all models have more variability than the measurements (since they extended beyond the solid line with sd=1). GPP products from V3-LD-FD and V4-LD-FX are close to each other but V4-LD-FX is slightly closer to the observed point. The dominant factor contributing to biases in modeled LE and GPP is the choice of LAI and FVEG (Figure 2-2). Both MODIS LE and GPP were calculated using observed or gap-filled climatological LAI in MODIS collection 6 to maximize the available reliable data. Therefore, potentially poor-quality LAI could influence LE and GPP and may dampen their inter-annual variability. The correlation coefficients for LE and GPP at the KON site range from 0.75 to 0.80 and 0.60-0.70 for the simulations, while LE and GPP correlation coefficients at the KFS site are slightly lower, 0.70-0.75 and 0.45-0.58 respectively (Figure 2-2). At each site RMSE values for LE and GPP (presented with gray arcs in Figure 2-2) are similar. But compared to KON site, RMSE increased from 0.75 to about 1 at KFS site, which reveals a higher degree of agreement between simulated LE and GPP from different model versions and field measurements at KON site. One of the reasons for the differences in the two locations is that the dominant land cover type at the KON grid cell in the model is consistent with dryland cropland and pasture as compared to KFS grid cell which is mainly characterized as cropland/grassland mosaic.

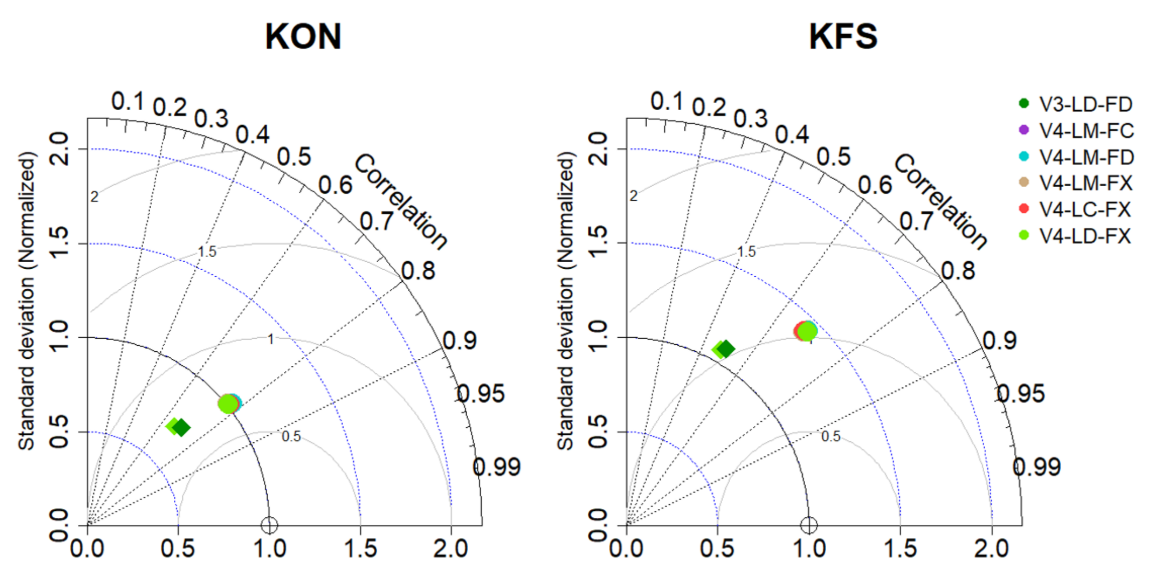

Figure 2-2:
Taylor diagrams for comparing model performance: (circles) latent heat (LE) and (diamonds) gross primary production (GPP) from both KON and KFS sites. The radial distance from the origin is the normalized standard deviation and the correlation coefficient is displayed as the azimuthal position. All statistics are calculated on a daily time scale from 2008 to 2018 and colors represent different models consistent with the color codes.

Seasonal Fluxes. To take a wider view of the role of dynamic phenology and the ability of the models to simulate the water and carbon cycle, 11-year average seasonal cycles of climatological fluxes are summarized in Figure 2-3 and Figure 2-4. It should be noted that the results of all model configurations, using MODIS LAI as input are qualitatively very close in all output variables at seasonal cycles at the two study sites. Therefore, LAI and FVEG model outputs nearly overlap each other (purple, cyan, and tan lines). At the KON site, all model configurations overestimate the climatological latent heat during the early growing season (Mar-Apr). However, the difference between EC measurements and all model simulations decreases substantially in the middle of the growing season (June) when leaves are fully developed, and fluxes are large and continue until the end of the year. Accordingly, at the KFS site, all configurations overestimated

LE during the early growing season with the largest positive bias in June (Figure 2-3). Model performance is reflected in 11-year averaged KGE scores between simulated and MODIS LE for different model versions at each site. At KON and KFS sites, V4-LM-FX model provides a better fit (with KGE = 0.345 and KGE = 0.737, respectively) between simulated and measured LE. At KFS, all model versions overestimate LE in comparison to EC observations but again V4-LM-FC and V4-LD-FX provide a better match with more accuracy leading to higher KGE values. Although the difference between simulated LE from all versions at both sites increases rapidly at the beginning of the growing season, this deviation becomes smaller particularly at KON site during the later growth stages. The peak value of modeled LE at both sites happens in June which is consistent with the measurements. Observed LE values from the early vegetative stage (April to July) represent sharp (at KON) and gradual (at KFS) rise and moderate decline during the late season from August to September at both sites. Simulated sensible heat fluxes (H) from all model versions were less at both sites for the first six months of the year compared to the EC measurements. These differences diminished from the middle of the growing season until the end of the year and the simulated H pattern became more consistent with the observations, especially at KFS site. The results of two versions of the model (i.e., V3-LD-FD and V4-LD-FX) compared with MODIS and EC measurements of GPP are also presented. Both versions of the model were able to reproduce the trend of carbon uptake compared to the flux measurements. Except for three months in the middle of the growing season (June-August) at KON site and one month (August) at KFS site, both models overestimate GPP. Like LE, peak simulated GPP happens in June which is almost 50 percent larger at KON than KFS site (Figure 2-3).

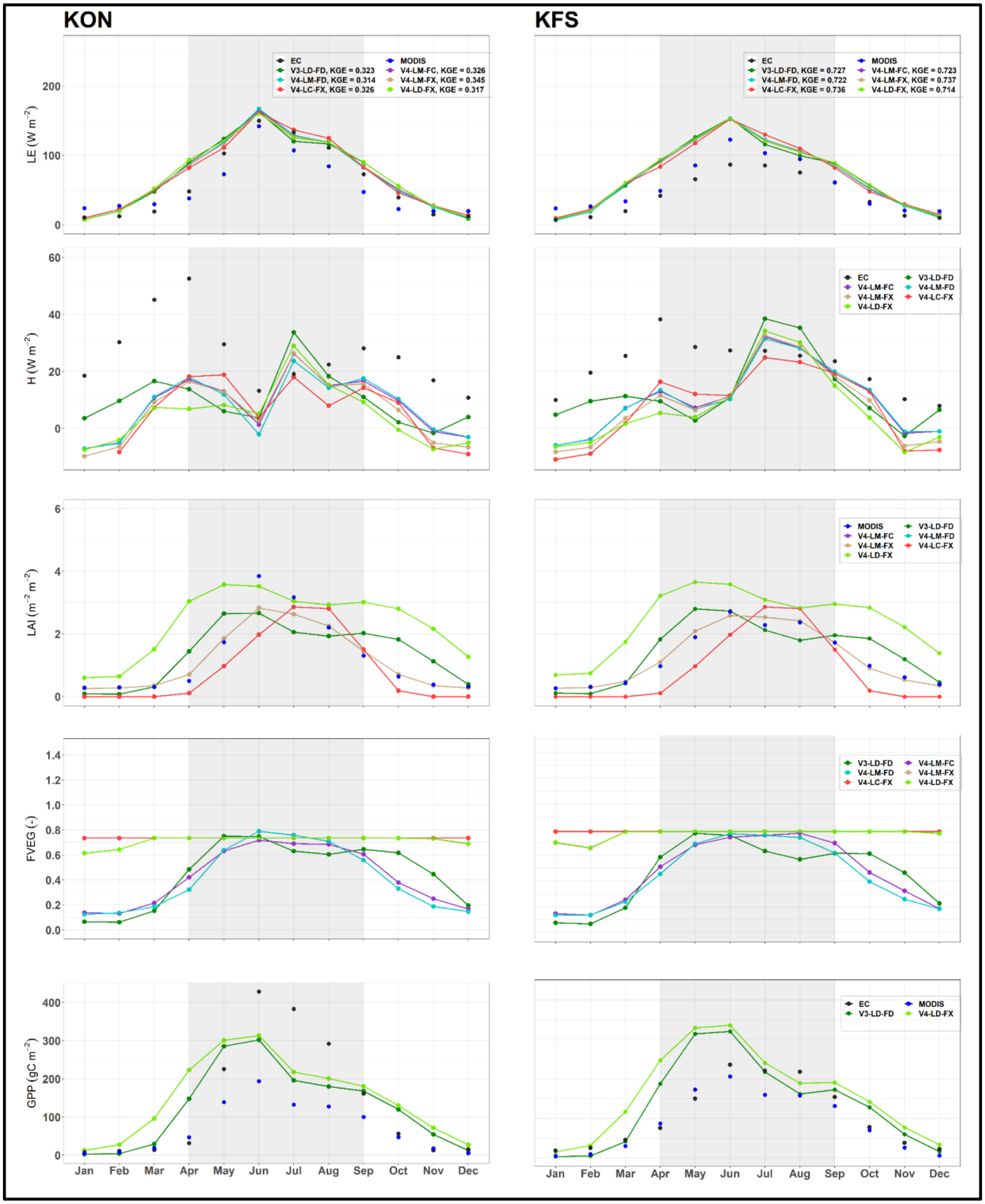

Figure 2-3:
Seasonal climatology of simulated LE, leaf area index (LAI), fractional vegetated area (FVEG), and GPP from different Noah-MP configurations vs. MODIS and EC measurements during the 11-year study period for KON and KFS sites. Gray-shaded areas denote the growing season.

Note that upscaling finer grid cells to coarser resolution resulted in a difference between the MODIS LAI value for a single tower pixel and MODIS measurements used in the model (divergence between all the MODIS-derived LAI model versions and blue dots, Figure 2-3). In addition, the difference among green vegetation fraction of versions using maximum climatology FVEG in winter months (January, February, and December) reflects the canopy height variation relative to the snow depth. When snow cover is higher than the vegetation height, FVEG will drop below its maximum value in the model.

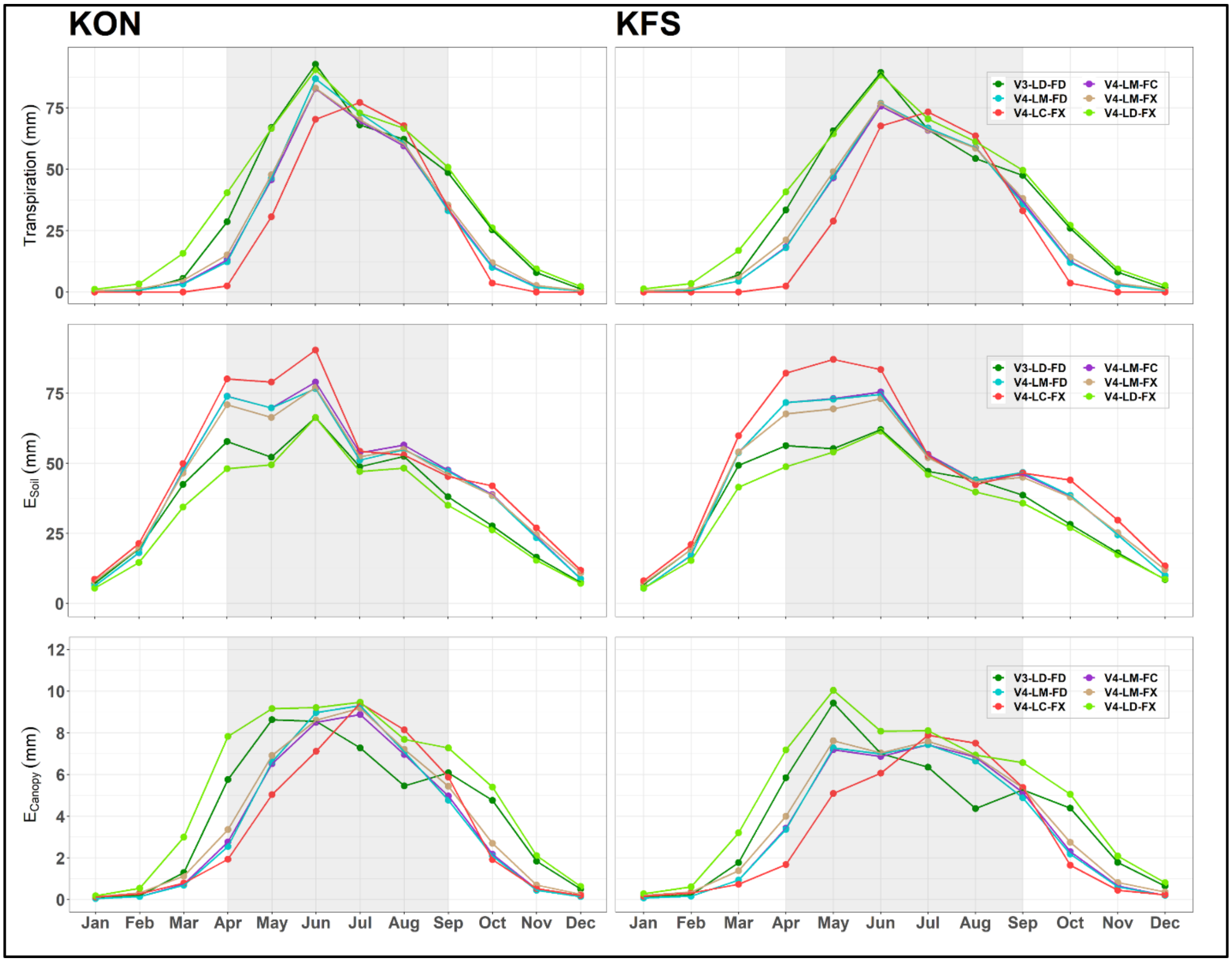

Figure 2-4:
Seasonal climatology of simulated Transpiration, E_{canopy}*, and* E_{soil} *from different Noah-MP configurations vs. MODIS and EC measurements during the 11-year study period for KON and KFS sites. Gray-shaded areas denote the growing season.*

One of the main takeaways from Figure 2-3 is that there is little deviation in the latent heat flux across model configurations despite the fact that the models vary substantially in their representation of LAI. To explore this in more detail, the components of LE including transpiration, soil evaporation (E_{soil}), and canopy evaporation (E_{canopy}) are shown in Figure 2-4. It is important to note that the units in Figure 2-4 are mm (evaporation), not w/m2 (latent heat flux) as in Figure 2-3. Despite the insensitivity of LE to the impact of vegetative properties at both sites, there is a distinct difference among individual components of LE for each model configuration. Specifically, transpiration and canopy evaporation vary directly with LAI, and models that show higher initial LAI, show a larger transpiration and canopy evaporation. It should be noted that canopy evaporation is relatively small (about 10 times smaller) as compared to the other components. Even though there is a high connection between model LAI and transpiration and canopy evaporation, this is offset by much lower soil evaporation. This tradeoff between soil transpiration, canopy evaporation, and soil evaporation results in little difference between the total LE in all model simulations and indicates that models are primarily operating in an energy-controlled regime.

Simulated Fluxes During Drought Events. Figure 2-5 presents the diurnal time series of measured and NLDAS-2 forcing precipitation, SM percentile, simulated transpiration, and simulated versus measured LE throughout two selected drought years (2012 and 2018). The simulation results of both sites show a nearly similar pattern, therefore, only the results for KON will be discussed. For all model versions, LE converges together when there is a precipitation event according to the NLDAS-2 atmospheric forcing data which indicates that all versions have a similar behavior when the soil is well watered. The large differences between modeled and measured LE values generally occur during inconsistencies between daily gauge measurements and NLDAS-2 rainfall forcing data. Top 1-m SM percentiles from all model versions slightly diverge from each other during the late winter and early spring but they show a very similar behavior throughout the growing season in both years. Despite the subtle variation, among SM percentiles from all model versions in the rest of 2018, there is a noticeable contrast among SM percentiles throughout the fall and winter of 2012. The behavior and magnitude of transpiration are almost identical in all the MODIS-LAI-based models and the pattern is very similar to the model versions with dynamic vegetation (e.g., V3-LD-FD and V4-LD-FX). However, there is a distinct separation between V3-LD-FD and V4-LD-FX, especially during the summer and early fall. Version with prescribed LAI (V4-LC-FX) failed to capture seasonal variability of LAI and FVEG and express a different transpiration pattern compared to the other version.

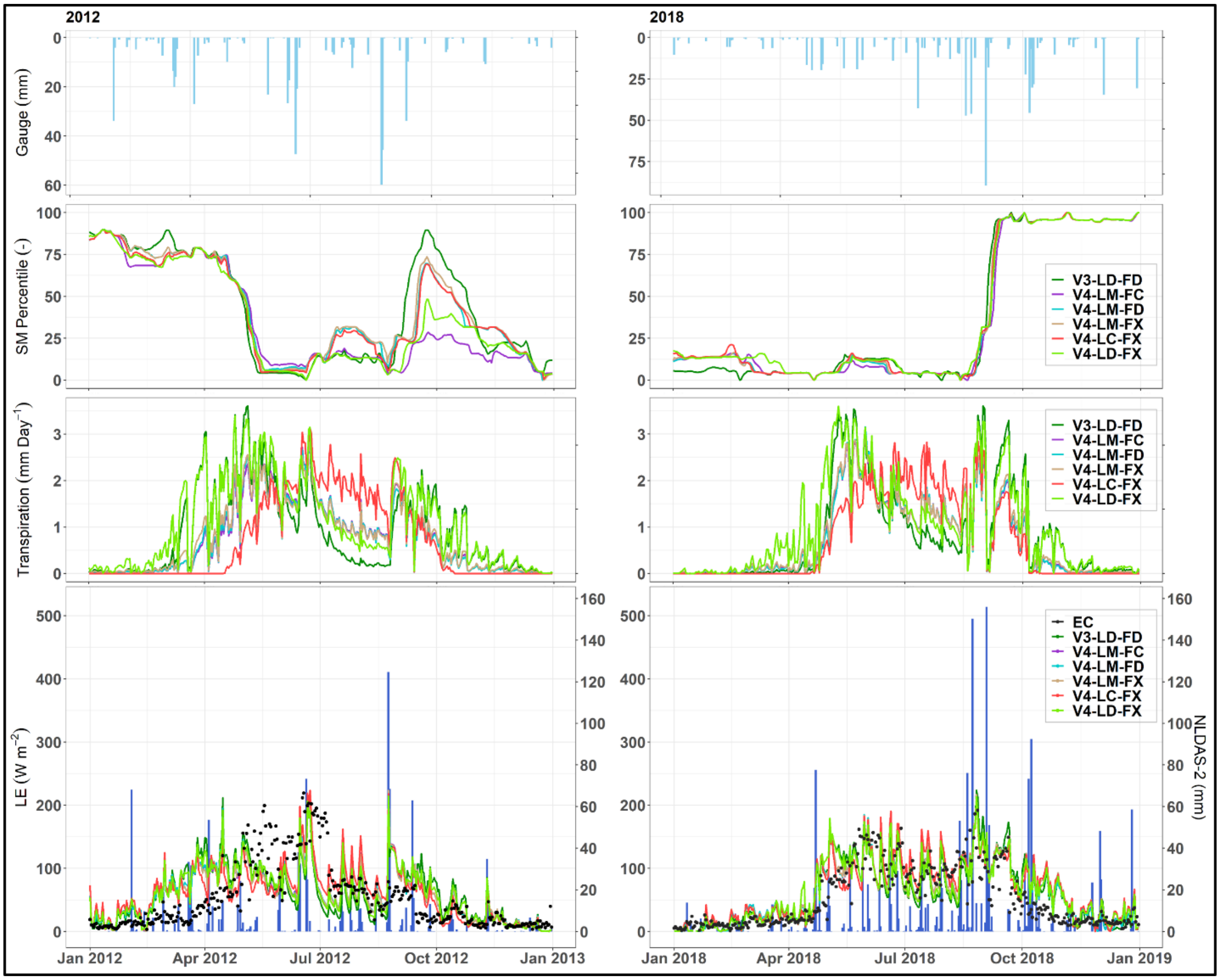

Figure 2-5:

Precipitation, top 1-m soil moisture percentile, transpiration, and LE at the KON site for two selected drought years (2012, left; and 2018, right). (Top panels) Gauge precipitation measurements at the site; (Second row) top 1-m soil moisture percentile; (Third row) Transpiration; (Bottom panels) Comparison of average daily simulated LE from all different Noah MP configurations (various colored lines) vs. EC measurements (black dots) and NLDAS-2 precipitation forcing (blue bars).

As shown in Figure 2-6, both V3-LD-FD and V4-LD-FX capture the general trend of LAI during the drought years. Except for a few months at the beginning of the growing season, V4-LD-FX overestimates LAI during both events. However, V3-LD-FD underestimates LAI in the middle and late growing season. Both leaf onset and LAI ramp-up occur much faster compared to MODIS-LAI measurements in both V3-LD-FD and V4-LD-FX models in 2012 and V4-LD-FX in

2018 which leads to higher LE during the growing season length. Measured and forcing precipitation were generally close to each other from January to April in both years. From the early growing season, NLDAS-2 starts to produce more precipitation, particularly in 2018 which results in a higher cumulative precipitation difference between the forcing and gauge measurements (Figure 2-6, third panel). There is a good agreement between all model versions simulated and in-situ measurements of SM in the top 10 cm, but this agreement faded after June during the 2018 event. The overestimation of soil moisture depletion during drying phases was greater in V4-LC-FX than in other versions. This version assumes fixed vegetation conditions for each year which leads to relatively higher ET loss estimates in both dry years, and a sharper decline of soil moisture at deeper layers (30-100 cm), especially during maximum plant development. Whereas dynamic LAI phenology in other versions simulates changes in leaf area and reproduces more realistic drought-induced vegetative stress and SM trends.

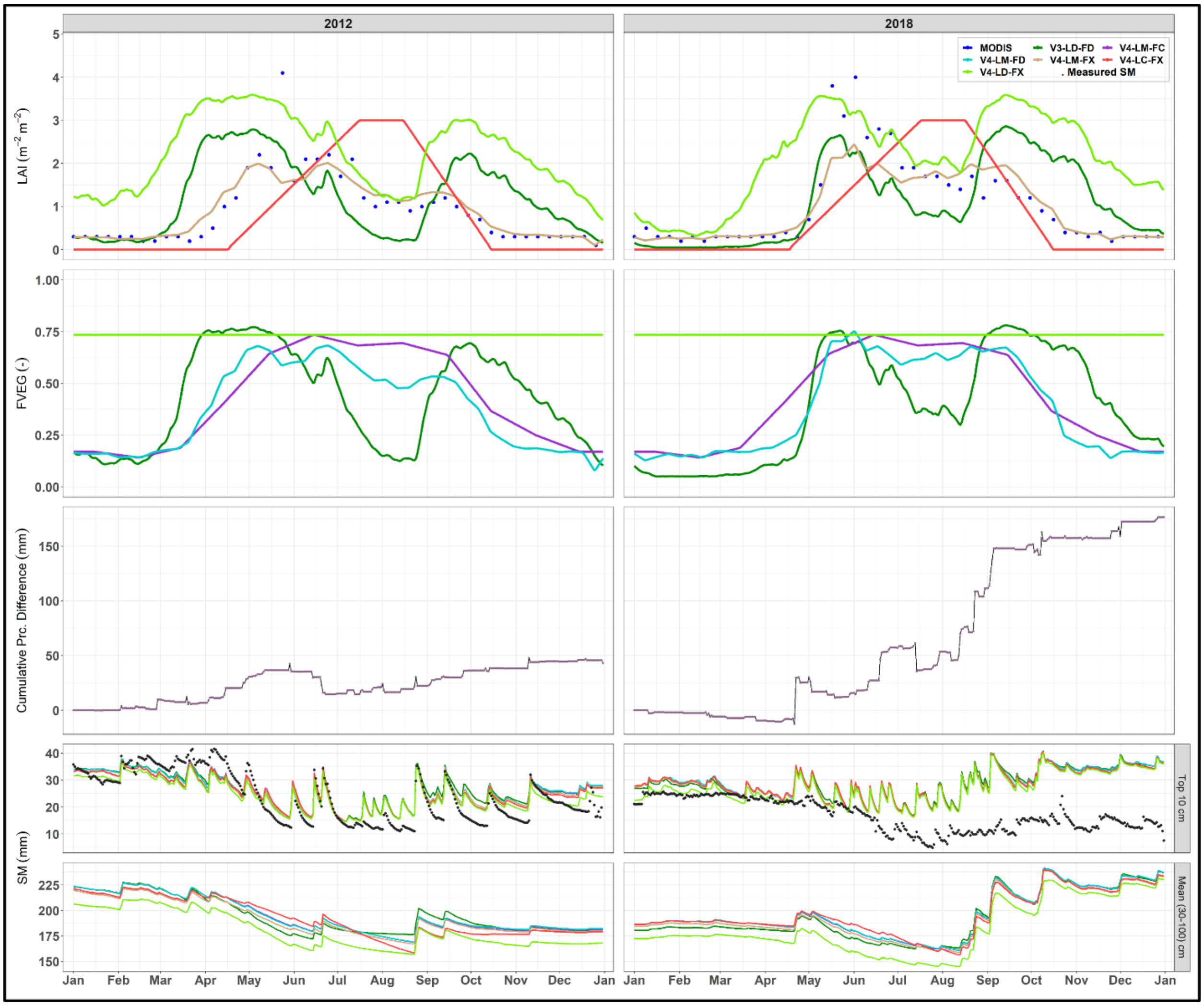

Figure 2-6:

Comparison of average daily simulated LAI from all different Noah-MP configurations vs. MODIS measurement. (Top panel), simulated FVEG (second panel), and simulated soil moisture for the top layer (10 cm) compared to the field measurements (black dots) and average soil moisture for the three bottom soil depths (30, 60, and 100 cm) (bottom panels) throughout the selected drought years (i.e., 2012 and 2018) at the KON site.

Domain Level. *Latent Heat Flux.* Figure 2-7 shows the spatial distribution of the 11-year domain-averaged mean seasonal KGE values between simulated and MODIS LE for the different model versions. The overall spatial patterns are consistent for all model versions with the highest values in the eastern part of the state and low values in the western portion of the state. A comparison of MODIS and modeled climatology indicated that all model versions overestimate

LE over the entire state, particularly in the central and western parts of the state (see Figure 2-8). Analyzing the components of KGE reveals that, except for small areas in the middle and southwest of the state, the overall correlation component is very close to unity over the entire region (Figure 2-9). This reflects the ability of the model to reproduce the timing and shape of the seasonal cycle as measured with no clear tendency for systematic errors (Figure 2-10). The areas with a higher ratio of the simulated and observed standard deviation corresponded with lower KGE values. In the central and east parts of the state, the ratio of the simulated mean and observed mean (bias ratio) for the latent heat flux is closer to one (Figure 2-11). This spatial pattern is more evident in MODIS-retrieved LAI versions (i.e., V4-LM-FC, V4-LM-FD, and V4-LM-FX). The large variability in LE from all the model versions other than MODIS in the western portion of the state indicates that the limitation of the model is mainly governed by the overestimation of variability.

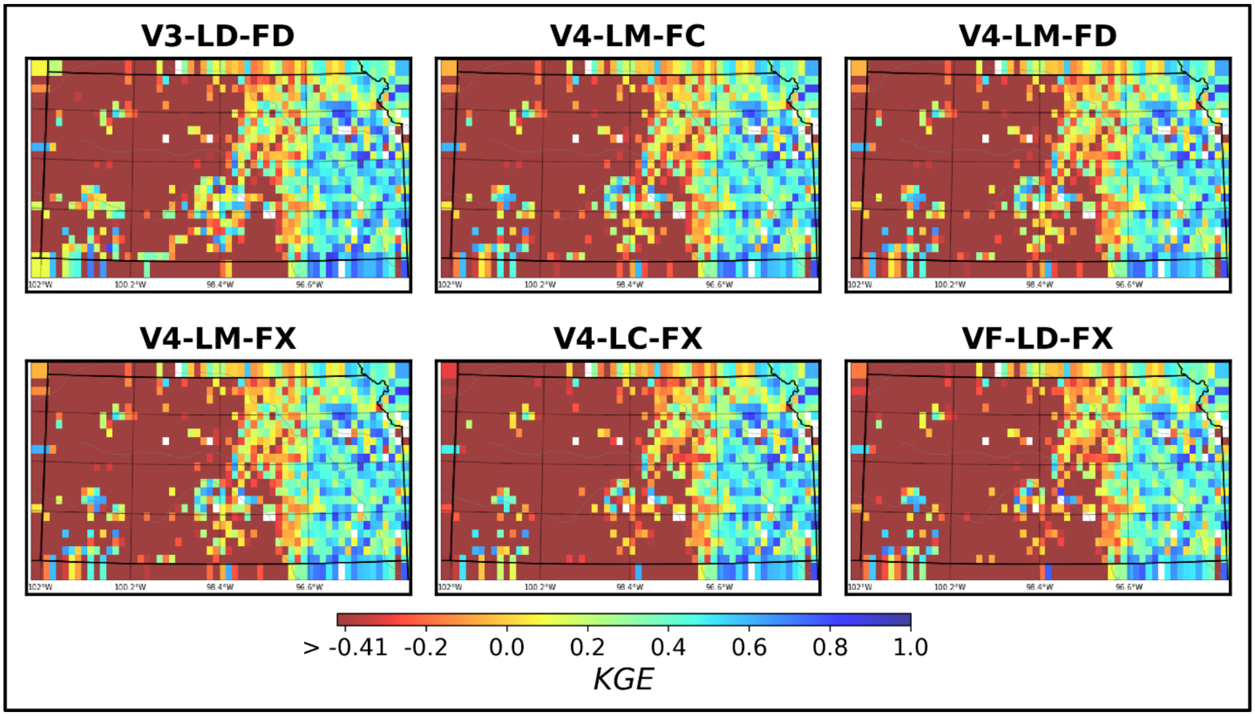

Figure 2-7:
Spatial distribution of seasonally averaged Kling-Gupta efficiency (KGE) of LE flux (W/m^2) between each Noah-MP configuration and MODIS. For the three assessment criteria, a value of 1 indicates a perfect agreement between MODIS and the simulations. The minimum threshold is set to −0.41 for any KGE values ≤ −0.41.

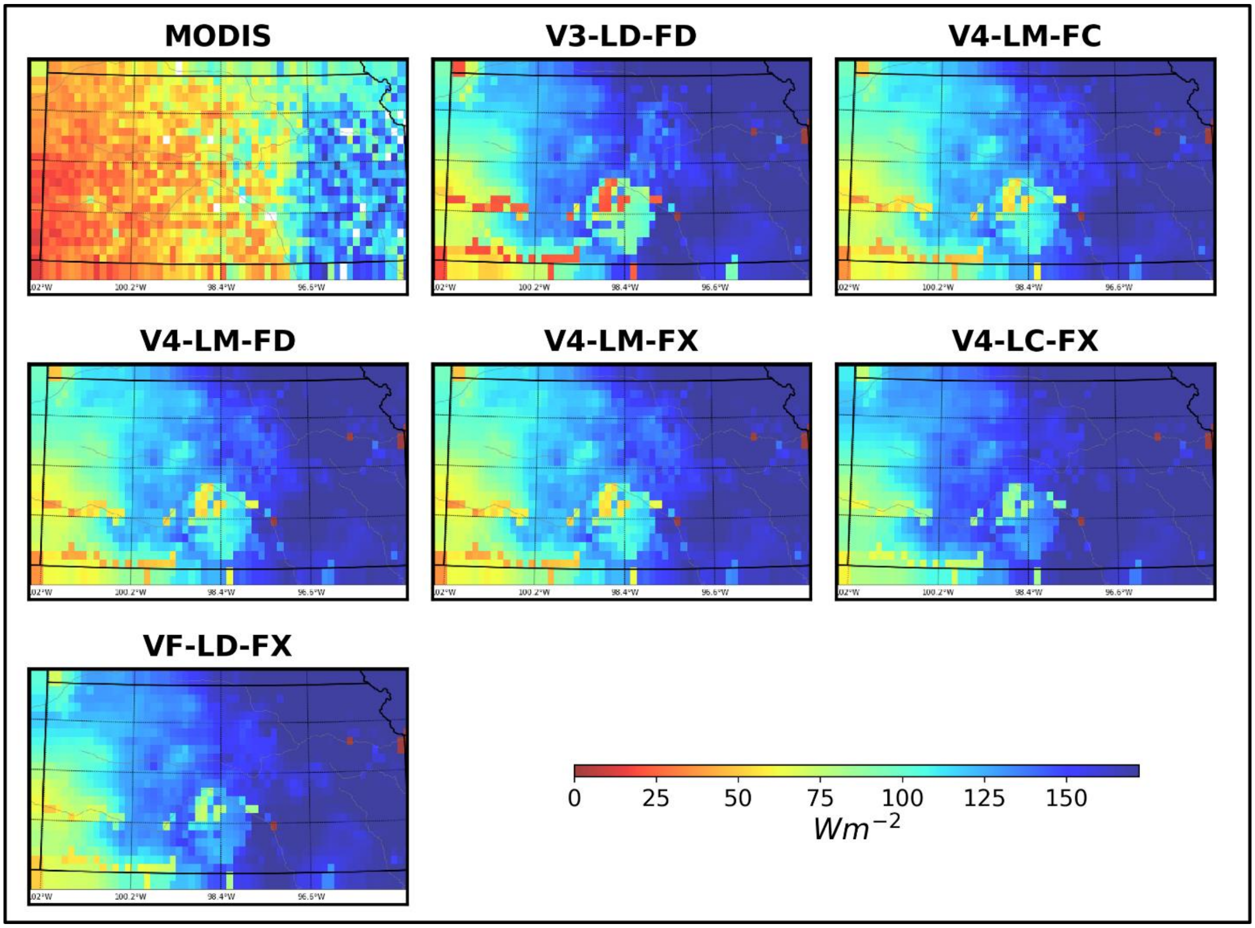

Figure 2-8:

Spatial comparison of climatological (11-year mean annual) latent heat (W/m^2) from all different Noah-MP configurations with MODIS for June.

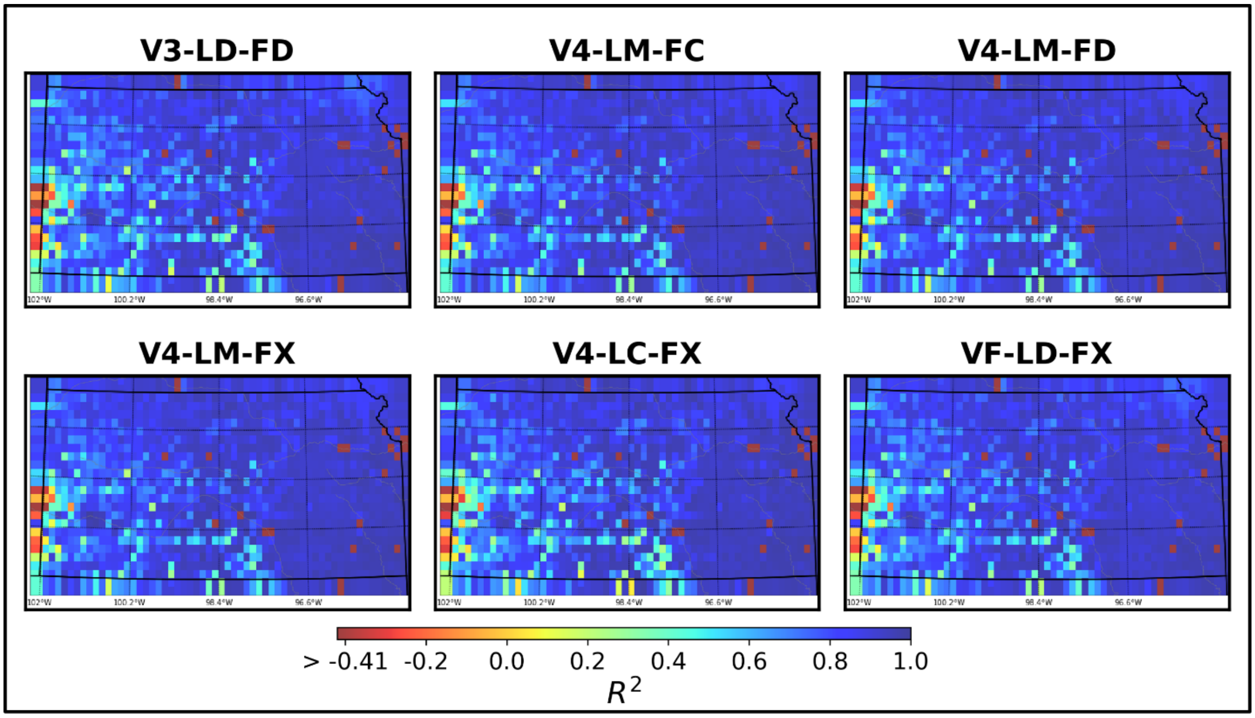

Figure 2-9:
Spatial distribution of Pearson correlation coefficient (r) component of seasonally averaged Kling-Gupta efficiency (KGE) of latent heat flux (W/m^2) between each Noah-MP configuration and MODIS. Values closer to one indicate better model performance.

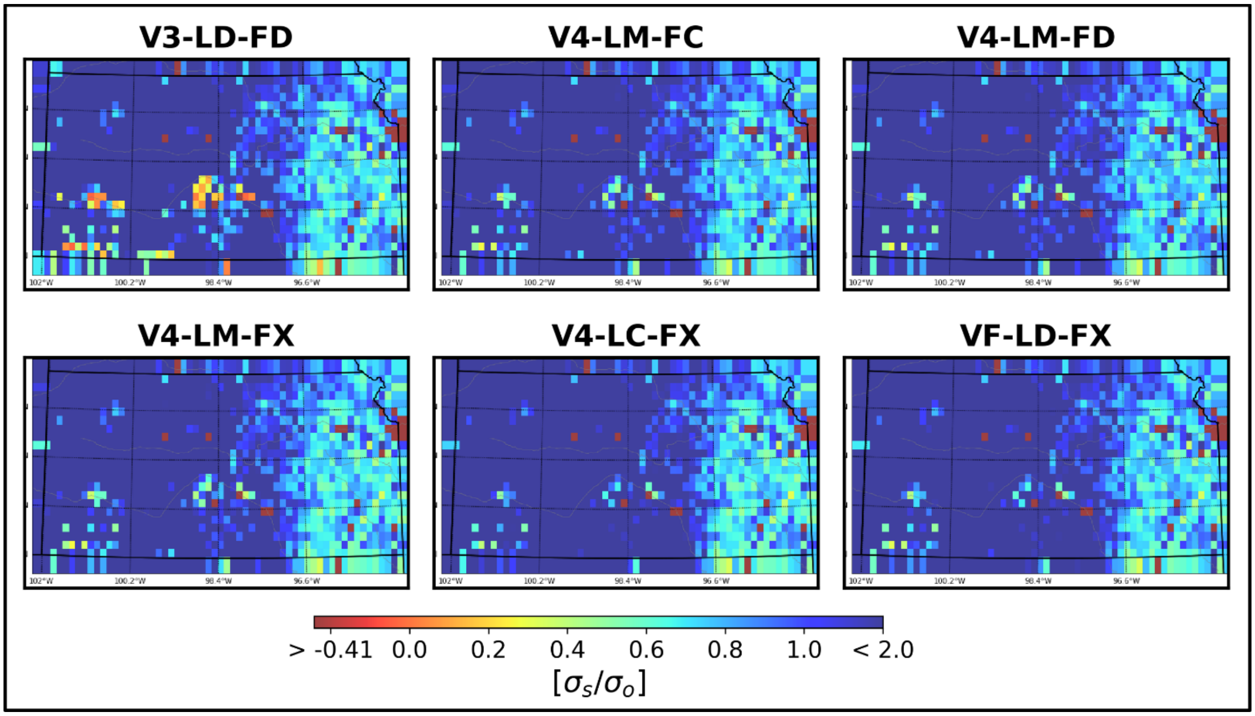

Figure 2-10:

Spatial distribution of variability ratio (σs / σo) component of seasonally averaged Kling-Gupta efficiency (KGE) of latent heat flux (W/m^2) between each Noah-MP configuration and MODIS. Values closer to one indicate better model performance.

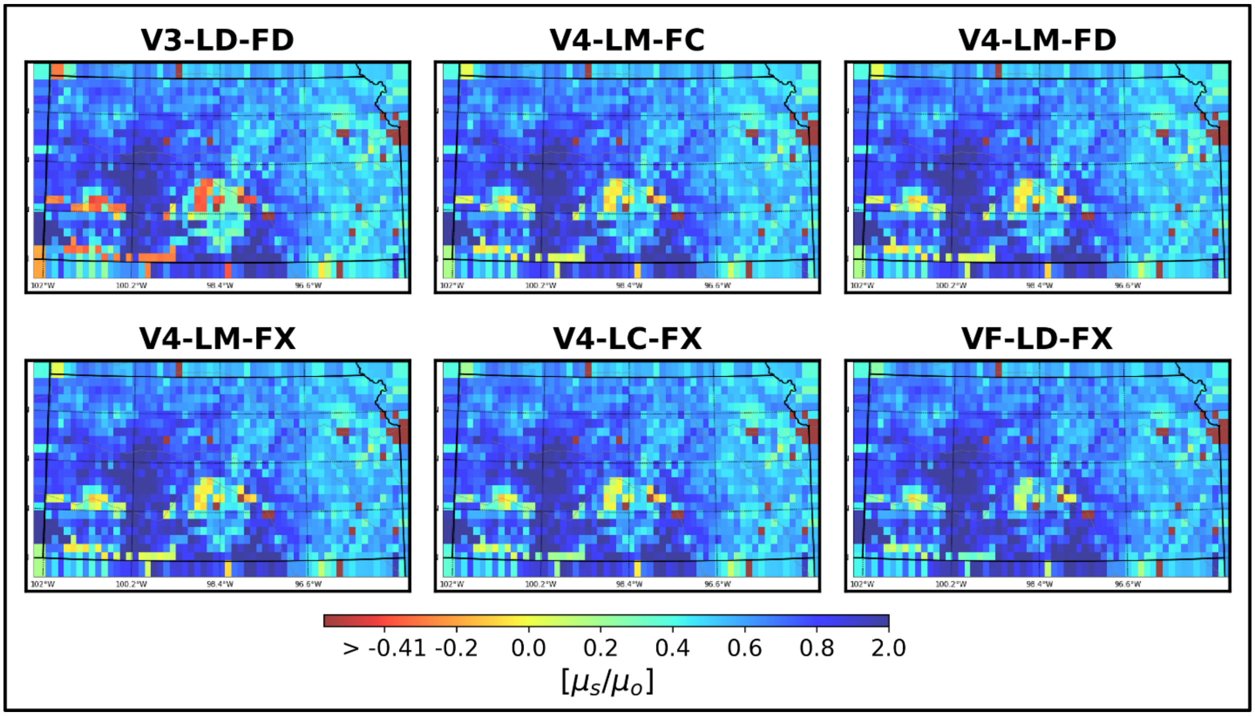

Figure 2-11:
Spatial distribution of bias ratio (μs/ μo) component of seasonally averaged Kling-Gupta efficiency (KGE) of latent heat flux (W/m^2) between each Noah-MP configuration and MODIS. Values closer to one indicate better model performance.

To further evaluate each model's performance, Figure 2-12 shows the 11-year climatological averaged LE of three selected grid cells. The three grid cells were selected based on average KGE values across all model runs. The difference among simulated LE from all versions is not very noticeable at the selected grid cells with minimum and maximum KGE values although this divergence becomes more pronounced at the location with a minimum KGE value. The peak of the LE at the grid cell with the highest KGE value happens in June which is consistent with the MODIS measurements (Figure 2-12a). At the selected grid with a minimum KGE value, MODIS LE is very low and does not vary over the year, but all model versions demonstrate a similar but higher LE (Figure 2-12b). The primary land cover type at this grid cell is comprised of sedimentary rocks. This issue could be attributed to the MODIS inaccuracy and model limitations in land cover type identification. The low and quite constant MODIS LE values could reflect the absence of water in this unvegetated rocky area. There is a distinct separation among model versions with different LAI and FVEG options at the grid cell with the minimum threshold KGE value which reflects the sensitivity of heterogeneous land-use and spatial locations to LAI and FVEG inputs (Figure 2-12c). In addition, at the grid cell with minimum threshold KGE value LE from MODIS is shifted to an earlier time (between May and June). Interestingly, LE products from MODIS never dipped below 15 (W/m^2) even in the wintertime compared to much lower EC measured values (≈ 5 W/m^2), which could reflect the limitation of the MODIS LE data (Miranda et al., 2017).

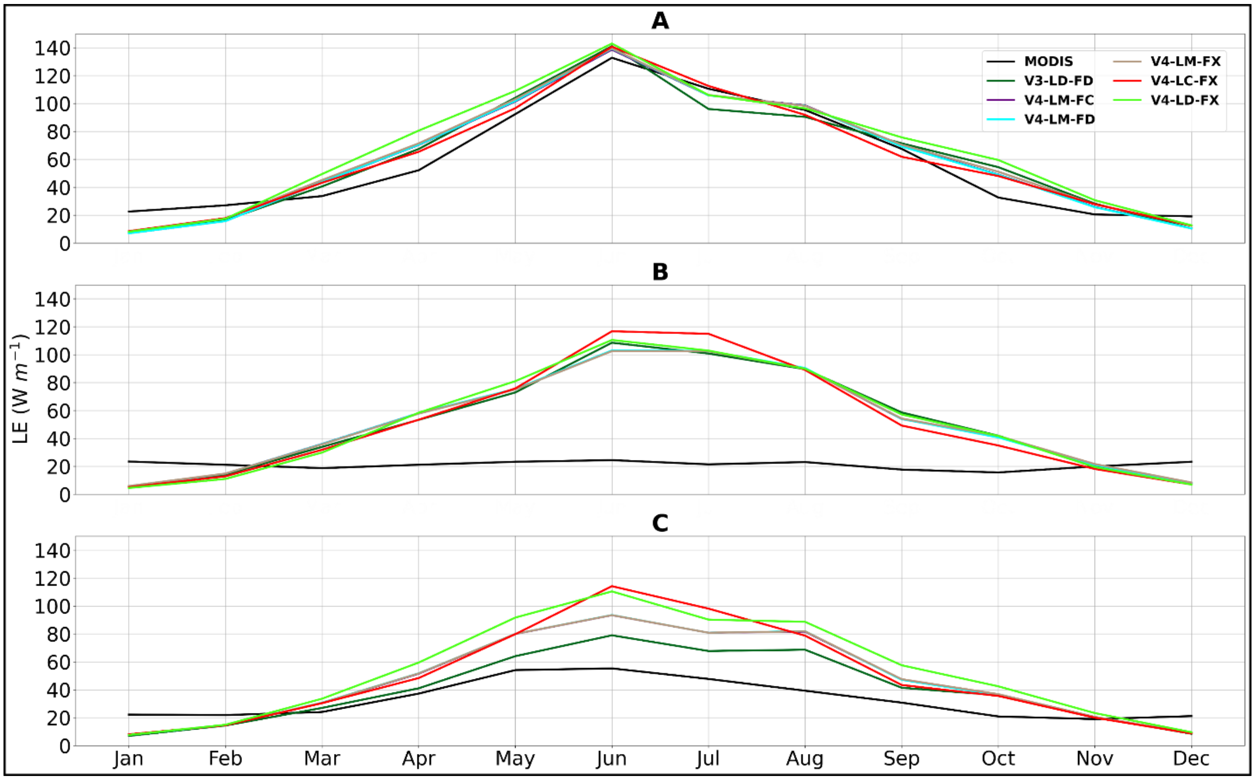

Figure 2-12:
Climatological LE from all different Noah-MP configurations vs. MODIS across the selected domain for the entire study period (2008–2018) (A) for grid cell with the highest KGE value (0.90) located in the western part of the state and the dominant land cover type is classified as grassland, (B) for grid cell with minimum KGE threshold (−11.87) located in the eastern part of the state and the dominant land cover type is classified as cropland/grassland mosaic, (C) grid cell with minimum threshold KGE value (−0.42) located in the south-central region of the state and the dominant land cover type is classified as grassland. Here, colors represent different models consistent with the color codes.

Monthly Streamflow. To further explore the impact of vegetative dynamics on surface fluxes and the water balance, we evaluate the model's performance for simulating the annual streamflow at 31 basins across the study domain. The median KGE values of the annual average streamflow for all model versions are given in Figure 2-13. The KGE scores vary among the different models and the study basins. Some gauges consistently perform better or worse than the others in all the models (e.g., the gauges denoted with letters a, b, and c in Figure 2-13) but most of the gauges do not demonstrate a consistent KGE score across the model configurations. As shown in Figure 2-13 (lower right), box plots compare the KGE statistics across the model configurations and indicate that the configurations that use measured MODIS-LAI (LM) result in slightly higher KGE values as compared to other configurations. However, there is no significant difference in model performance among the six configurations, in terms of KGE for simulated annual streamflow with all versions reflecting the same spatial variations in streamflow across the domain. Although not shown, the majority of basins have a correlation coefficient (r) closer to the ideal value of unity and there was no basin with a negative correlation. The bias ratio between average values for modeled (μs) and measured (μo) discharge and variability component (σs / σo) is less than one for most of the gauges. This represents an underestimation of discharge with lower variability in simulations. The notable underprediction in streamflow could be the result of an overestimation of evaporation (Figure 2-3) or a simplified representation of groundwater dynamics in Noah-MP which represents recharge and discharge processes in an unconfined aquifer.

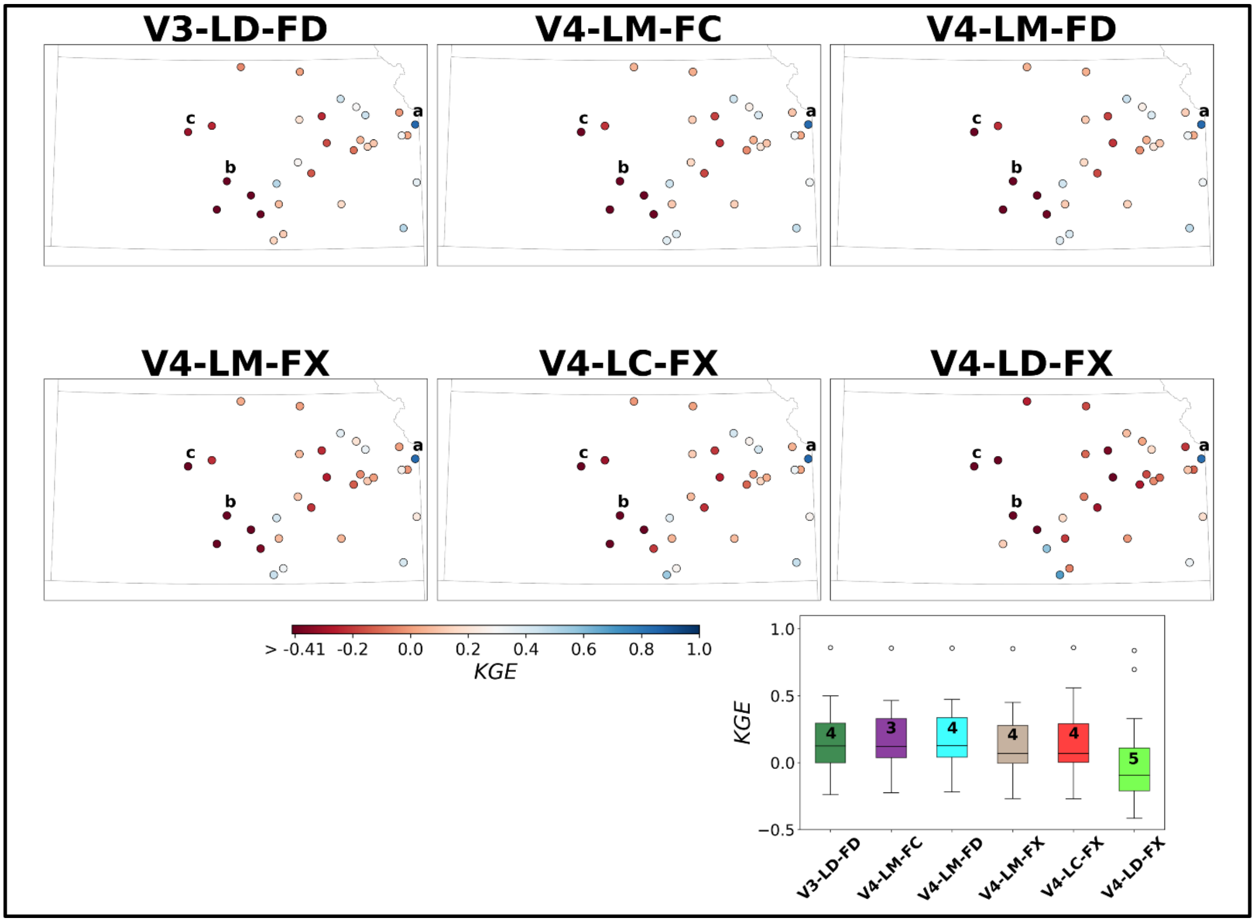

Figure 2-13:

Map of streamflow prediction performance using KGE for 31 selected basins across the model domain, and boxplots of each model configuration with the range from −0.41 to 1. The numbers on the boxplots represent the total number of gauges below the minimum KGE benchmark value (−0.41). Locations of USGS gauges with maximum (a), minimum (b), and minimum threshold (c) average KGE in this figure are marked on the map.

To further illustrate the streamflow behavior for each model configuration, the mean monthly time series of simulated streamflow for selected gauges with the highest, lowest, and minimum KGE values are shown in Figure 2-14. Overall, there was a good agreement between all model version simulations and USGS measurements at the mean monthly time-step for the selected gauge with the highest KGE value (Indian Creek, Overland Park, KS). This gauge is in the northeast part of the state, suggesting good model performances over the subhumid to humid regions of Kansas (Figure 2-14a). Other gauges with minimum mean KGE value (Rattlesnake

Creek near Zenith, KS), and minimum threshold KGE value (Big Creek near Hays, KS) are in the central part of Kansas (gauge locations indicated in Figure 2-13). At Rattlesnake Creek, all model versions overestimate the monthly averaged runoff regime (Figure 2-14b). At Big Creek, simulated runoff followed the trend of the USGS observations reasonably well until 2016 but after that, the simulated streamflow exhibited considerable underestimation of peak low magnitudes (Figure 2-14c). This could reflect a significant difference between climatic characteristics in the eastern versus western part of Kansas. Generally, the western part of the state is characterized by a semiarid climate with hot, dry summer and cold, windy winter and the eastern part tends to be considerably more humid, with sultry summer and cold winter months. This west-east climatic contrast impacts the generation of surface runoff and evaporation which is closely related to rainfall intensity. In addition to spatial patterns in precipitation gradient, in the west and central areas of Kansas, excessive groundwater pumping may lower the water table below the stream-water surface, causing the stream to lose water to the underlying aquifer and decrease the groundwater seepage to the stream. In addition, catchment size and land use characteristics may also affect the runoff retention time. Hydrographs indicate that all the model versions tend to consistently underestimate the peak streamflow in the west and central parts of Kansas.

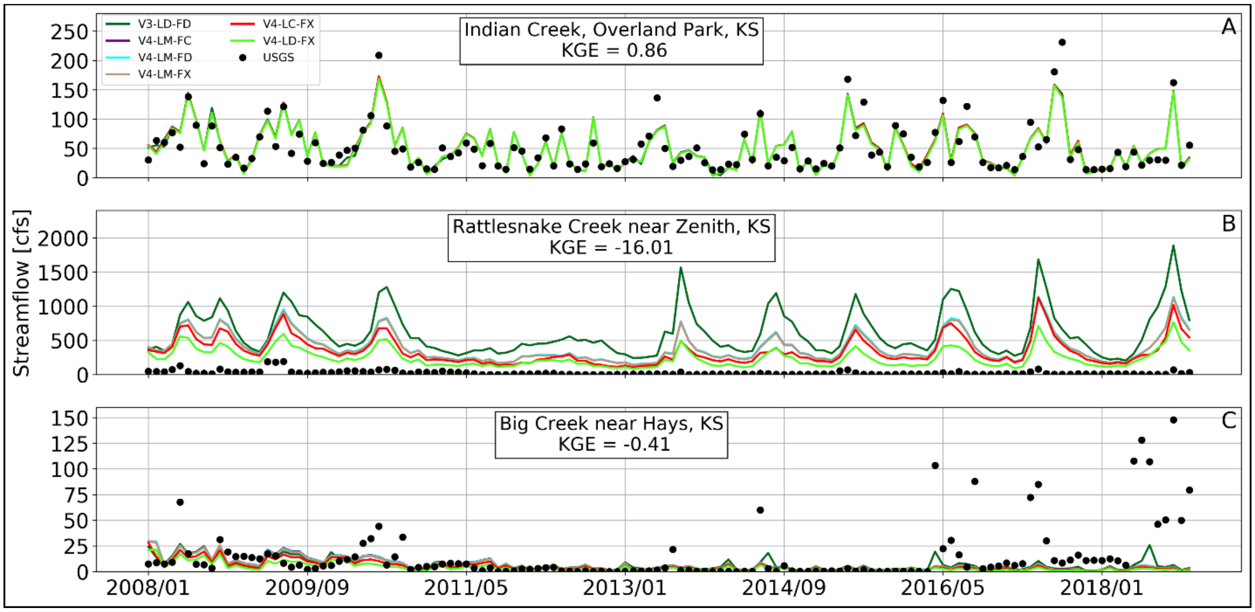

Figure 2-14:
Comparison of monthly simulated streamflow time series with USGS gauge measurements for selected gauges with (A) maximum average KGE (Indian Creek, Overland Park, KS), (B) minimum threshold KGE, (Rattlesnake Creek near Zenith, KS), and (C) minimum average KGE value (Big Creek near Hays, KS).

Model Performance Evaluation During Drought. To investigate the impact of vegetation representation in simulating rapidly emerging severe drought conditions, the simulated top 1-m SM percentile from different model versions over the state of Kansas were compared with USDM drought categories for two selected drought events in 2012 and 2018 (Figure 2-15). It is necessary to note that some disagreements between the model SM Percentiles and USDM are expected since the USDM drought is based on many factors like county-level information on drought, expert opinion of a drought's current impact on a region, precipitation, streamflow, reservoir levels, snowpack, and groundwater (Sehgal & Sridhar, 2019). Furthermore, the model SM percentiles were calculated using only the 11-year simulation period. Despite these differences, a general agreement is expected and the USDM can still provide a good comparison to assess the ability of the model to detect drought. In August 2012, exceptional drought (D4 category) covered most of the west and portions of the east part of the state. In August 2018, only some areas in northeast

Kansas were affected by the D4 category drought. It can be observed that the top 1-m SM percentile maps from all model configurations in 2012 show much lower drought conditions over the entire state, while USDM indicates exceptional drought over much of Kansas. But both V3-LD-FD and V4-LD-FX versions present a closer spatial resemblance between the model and the USDM map. This is interesting since, despite slight differences among all the 4.0.1 versions, they could replicate the majority of the drought-affected areas in 2018 events. Underestimation of drought magnitude in the large pocket in the central and western part of Kansas during the 2012 event is likely associated with the model's ability to imitate rapidly developing droughts like in 2012. Overall, the behavior of the gridded SM percentile is reasonably consistent with the drought categories on USDM maps in 2018 but there are some differences in the case of severe drought areas.

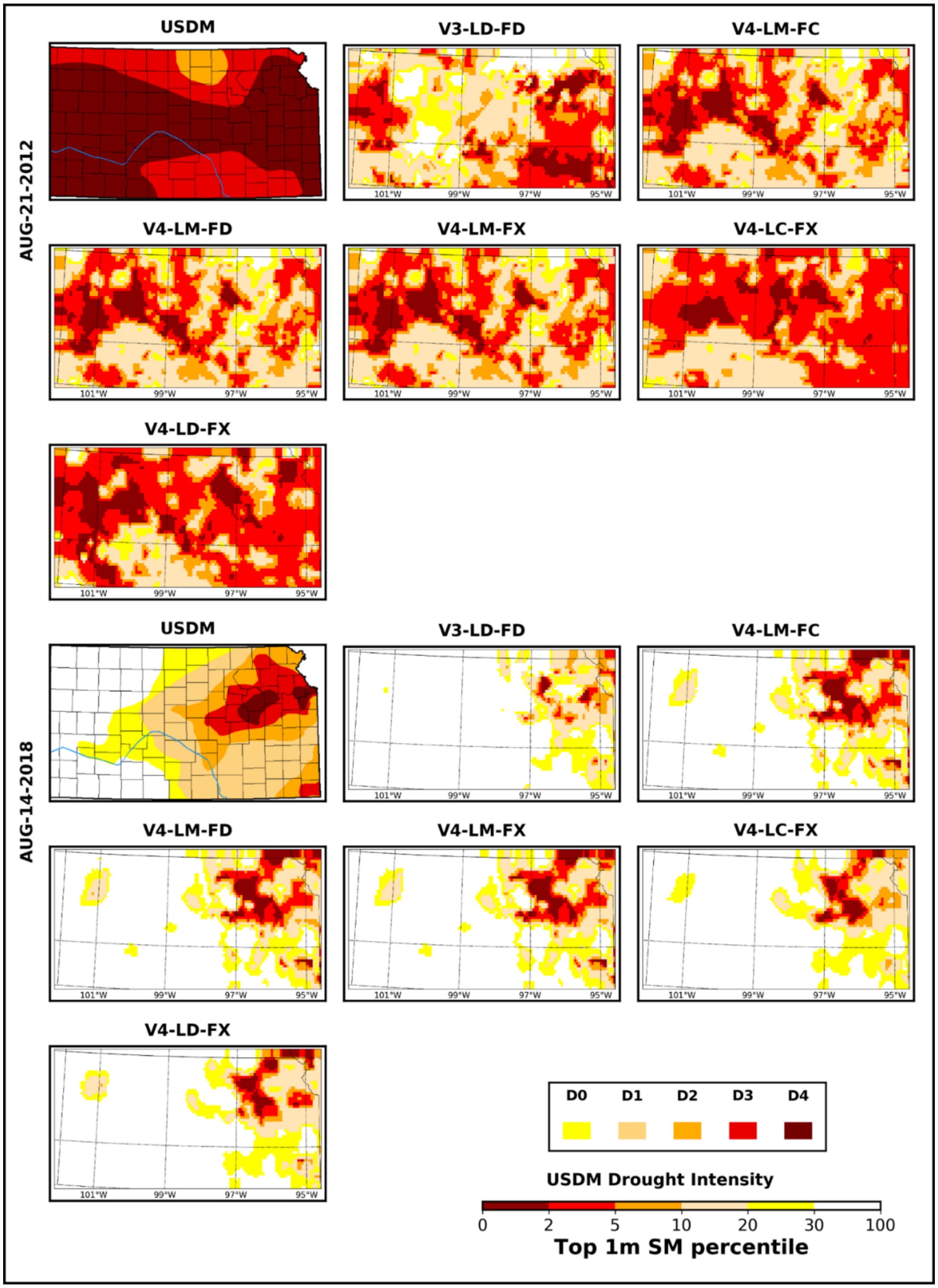

Figure 2-15:
The US Drought Monitor (USDM) and the modeled soil moisture percentile for the top 1 meter of the soil over the state of Kansas on 21 August 2012, and 14 August 2018. Colors indicate drought categories defined by the USDM, from abnormally dry (yellow) to exceptional drought (dark red).

2.4.2 Sources of Uncertainties

Overestimation of evaporation (LE) fluxes in the model could be ascribed to uncertainties in the MODIS LAI data and model biases in soil moisture, groundwater storage, or representation of vegetation within the model. In theory, large negative or positive biases in model-predicted storage are most likely mitigated by overestimation (underestimation) of both outgoing fluxes (i.e., runoff and evaporation) to close water balance in long-term averages (Lin et al., 2018). To understand the possible tendencies in long-term water budget on how changes in one component affect the estimation of the other mutually dependent hydrologic processes, we used a simple water balance equation:

$$\boldsymbol{P} = \boldsymbol{E} + \boldsymbol{Q} \qquad \text{(Eq. 2)}$$

where P is precipitation, E is evaporation, and Q is runoff. In this equation, all variables are expressed as an 11-year average, and change in storage is considered negligible under the assumption that there is no trend in storage change and that year-to-year variations cancel each other out over a long period. Since there was no statistically significant difference among the other version outcomes, the result of V4-LD-FX is presented here (Figure 2-12 and Figure 2-13). In Figure 2-16, each dot represents one of the 31 selected drainage areas of the USGS gauges within the study domain. The color scheme presents an 11-year average NLDAS-2 annual precipitation. The estimated average evaporation from all models and water balance is expected to show a very close relationship, but it is noted that there are more dispersions around the line with a slope of unity compared to the model versus water balance evaporation (Figure 2-16). This deviation pattern is even more evident for basins with drier conditions (average annual precipitation < 900 mm), especially in MODIS versus water balance evaporation comparison (Figure 2-16b). It is apparent that both the model and water budget overestimate evaporation in comparison to the

MODIS data, but the model exhibits the highest level of prediction accuracy (R^2 = 0.80). These results are consistent with the findings reported by the authors here in this reference (Brunsell et al., 2021). Among all versions, V3-LD-FD presents the lowest agreement between Noah-MP and water balance versus MODIS evaporation (R^2 = 0.73 and R^2 = 0.48 respectively).

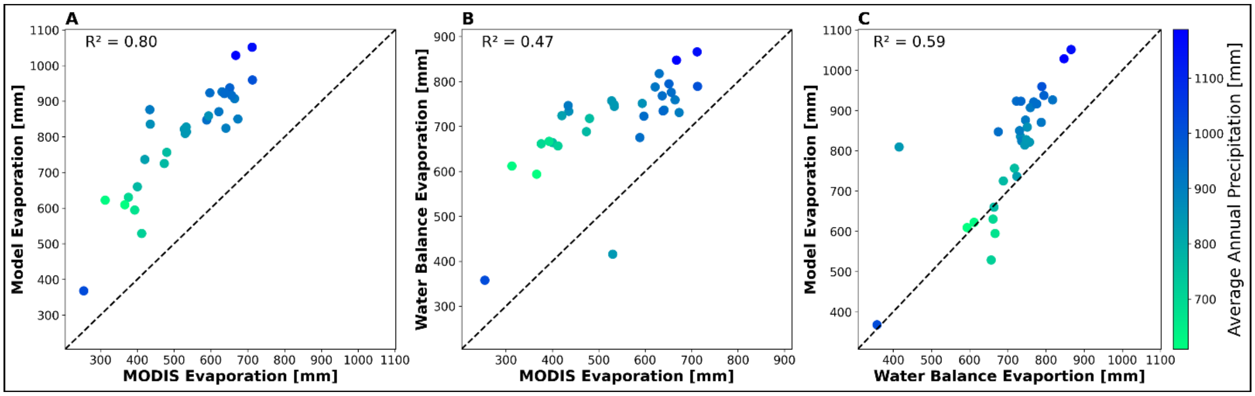

Figure 2-16:
Scatter plots of V4-LD-FX version (A) Noah-MP evaporation vs. MODIS, (B) estimated evaporation from water budget vs. MODIS, and (C) estimated evaporation from water budget vs. model for 31 selected basins using an 11-year average. The color bar indicates the 11-year average precipitation (mm) over selected basins within the domain from higher (blue) to lower (green) values.

Figure 2-17 illustrates the relationship between USGS gauge measurements with averaged runoff estimations of V4-LD-FX for the 31 selected drainage areas and the color bar indicates the difference between water balance and model streamflow. We observed that streamflow is reasonable by model simulations (R^2= 0.49). However simulated streamflow is underestimated compared to USGS measurements. The results of surface runoff analysis suggest that overestimation of evaporation is characterized by underestimation of peak-flow magnitudes which indicates more water should be retained in the soil layers instead of evaporating into the atmosphere. This might also be attributed to a poor estimation of the model parameters or due to an interaction of the model parameters that had a significant effect on the dominating processes in that flow range. Here again, we noticed that V3-LD-FD exhibits less agreement between Noah-MP and USGS gauge measurements ($R^2 = 0.30$) among all models.

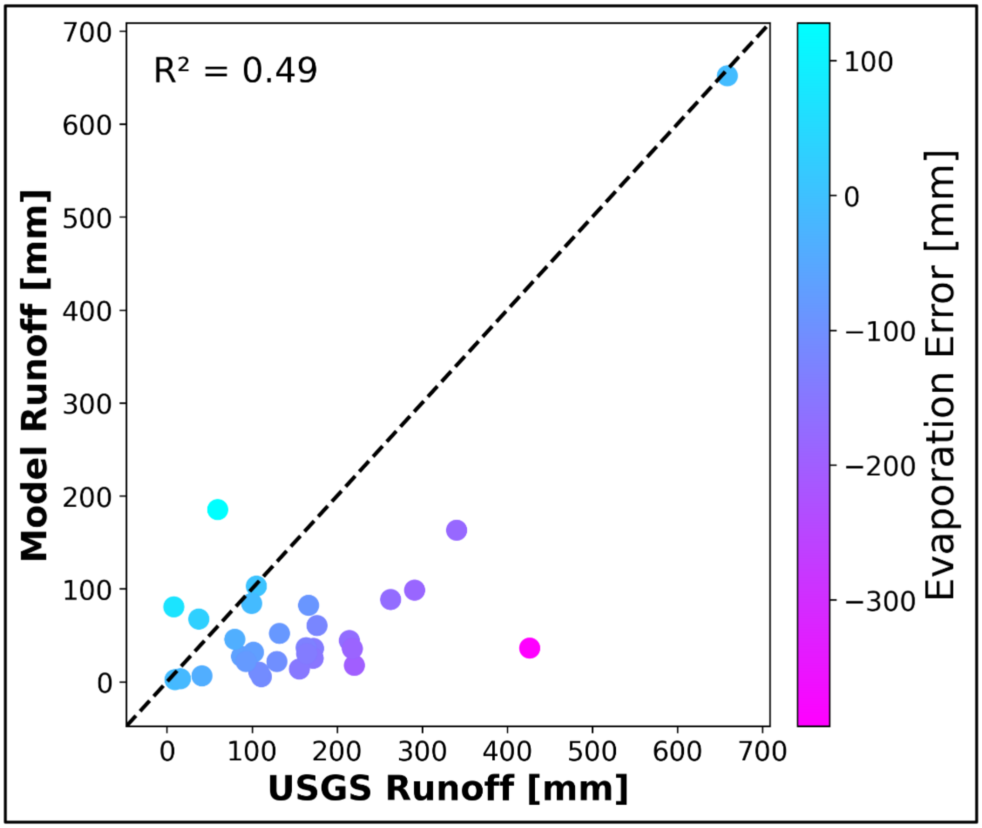

Figure 2-17:
Comparison of V4-LD-FX version vs. USGS gauge streamflow measurements for 31 selected basins. The color bar presents the difference in simulated and water budget evaporation during the 11-year average.

The extreme point on the lower-left corner of the scatter plots (Figure 2-16a-c) does not follow the same pattern on the precipitation gradient. This point represents a basin on the northeastern border of the state that is heavily urbanized. Despite a relatively high 11-year average precipitation, the rate of the LE is very low. Significant low evaporation at this basin is a compound result of the reduction in LAI and diminishing of transpiration from vegetation and evaporation lost from canopy interception which promotes wetter soil conditions and greater surface runoff.

This is also noticeable in the close value of all models' averaged runoff to the USGS measurement (extreme upper-right point in Figure 2-17). In addition, impervious land covers in urban areas have a pronounced effect on bare soil evaporation.

Figure 2-18 compares the ability of the model to simulate LE as KGE score versus the 11-year annual average of NLDAS-2 meteorological forcing (i.e., air temperature, precipitation, specific humidity, wind speed, downward shortwave (SW) and longwave (LW) radiation) for the dominant USGS land cover categories across the model domain. Surface pressure was excluded from this analysis due to its undetectable impact on the relationship between LE performance and land cover type. Due to a similar pattern among all model version outcomes, the result of V4-LD-FX is presented here. Cropland/grassland mosaic and grassland land cover types exhibit lower KGE values in hot and dry conditions (low precipitation and humidity and high shortwave radiation). The impact of wind speed and air temperature on specific land cover type were not very clear. Only dryland cropland and pasture (DCP) present relatively lower KGE in response to higher air temperature. Based on the USGS land-cover category, much of the western part of the state is classified as cropland/grassland mosaic and grassland in the model. Irrigated croplands impact the thermodynamics of the sensible and latent heat fluxes. Moreover, with the high level of soil water content, LE becomes independent of the soil moisture in an energy-limited evapotranspiration regime. Evaporation links the water balance to the surface energy balance with the heterogeneity of the landscape being accounted for by land cover type in the model. Therefore, an investigation of land cover–precipitation feedback and its impact on model performance is suggested for future studies.

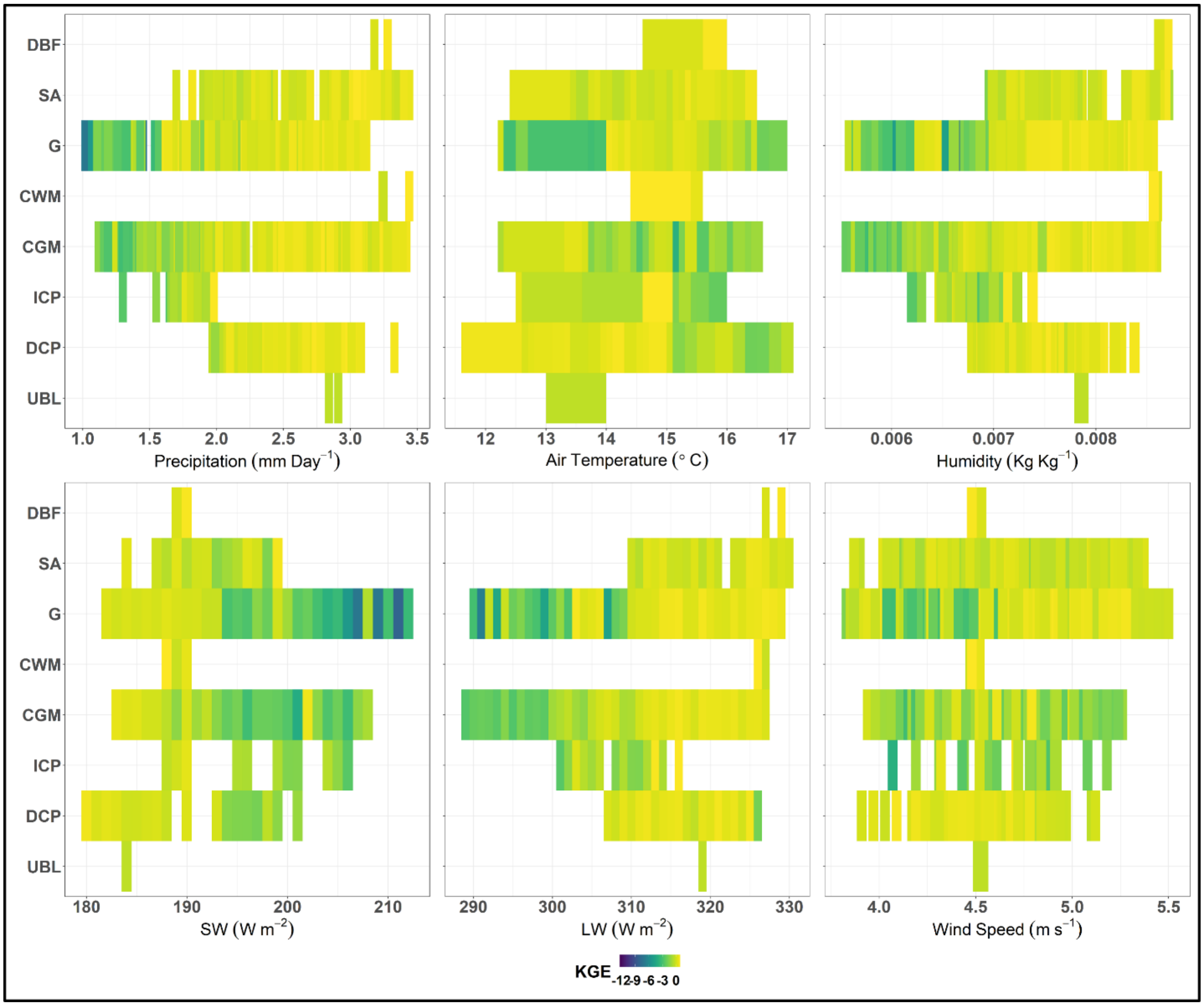

Figure 2-18:
The variation of the KGE between the model and MODIS LE flux with respect to the dominant land cover and the 11-year mean annual NLDAS-2. The forcing components include precipitation, air temperature, specific humidity, downward shortwave (SW) and longwave (LW) radiation, and wind speed.

2.5 Discussion

The dynamic vegetation scheme in the land surface model significantly influences the water and carbon budgets of terrestrial hydrological modeling. In this study, we investigated the impact of including and excluding Noah-MP dynamic vegetation function on key water and carbon budget terms by comparing 6 different model configurations against field measurements. The difference in each version is related to the calculation of LAI and FVEG. The simulation results reveal the difference between dynamic leaf model calculation of LAI estimates (V3-LD-FD and V4-LD-FX) and LAI from MODIS real-time data (V4-LM-FC, V4-LM-FD, V4-LM-FX) at the point-scale for two selected study locations, were able to reasonably capture the temporal variability of the LE component (i.e. transpiration, E_{soil}, and E_{canopy}) and sensible heat flux. The Noah-MP model requires the conservation of the partitioning of total net radiation (Rn) energy that reaches the land into sensible and latent heat and soil heat fluxes (Best et al., 2015; Niu et al., 2011; Pitman, 2003). As a result, portioning of Rn could impact the ability of the model to predict both sensible and latent heat fluxes. With enough soil moisture, Noah-MP uses the remaining energy to evaporate water from the soil into the atmosphere resulting in the unchanged magnitude of the total LE. The result from performance matrixes in Figure 2-18 also indicates that a lower KGE score for simulated LE is connected to limited incoming shortwave radiation over dominant domain landcover types. At the site level, V3-LD-FD and V4-LD-FX simulations captured the observed seasonal trend of GPP, but they underestimated GPP during peak growing seasons. The underestimation of LAI during the growing season is attributed to less carbon allocation to leaves and lower GPP during the growing season (Figure 2-3). This reflects the greater photosynthetic capacity of dominant C4 grassland with a more rapid accumulation of green leaf area than C3 plants in the model (Figure 2-3).

In addition to LAI and FVEG, in all model versions stomata are controlled mainly by average soil water availability (or β factor), leaf maximum carboxylation rate (Vcmax,) and maximum rate of carboxylation by the enzyme Rubisco (Vcmax25) which are treated as vegetation type-dependent constants. The only recognition of the hydrodynamic properties of plants in Noah-MP is the rooting depth. However, the depth of rooting solely serves as an indicator of the specific soil layers that should be integrated into a singular average soil moisture value, ultimately governing the regulation of stomata. Nevertheless, the authors of the reference (Wang et al., 2018) revealed that by substituting the static root profile with dynamic root optimization within the default Noah-MP model, they achieved a heightened level of accuracy in depicting root responses to evapotranspiration fluctuations between wet and dry seasons. Plant Water Use Efficiency (WUE) remains a major challenge for simulations of diurnal dynamics of transpiration (Matheny et al., 2014). Root zone soil moisture also has a direct impact on baseflow and streamflow simulations.

A rapid shift in vegetation emergence than actual plant coverage implies that current Noah-MP versions are generally missing important processes, such as the negative lagged effect associated with warmer springs which consequently leads to the buildup of water stress (Buermann et al., 2018; O'Sullivan et al., 2020; Wolf et al., 2016). Again, mainly due to the spatial scale difference between satellite observations and model grids, there is a discrepancy between MODIS observation at the flux tower and simulated LAI in all the MODIS-LAI-based model versions.

Implementation of prescribed LAI/FEVG with the same vegetation values every year can generate abnormally high ET during dry conditions and exacerbate soil moisture deficits. To address this issue enormous efforts have been made to introduce dynamic growth simulations into Noah-MP over the last decade. Authors in reference (Liu et al., 2016) introduced dynamic growth simulations and field management for two summer crops (corn and soybean) into Noah-MP (Noah-MP-Crop). Additionally, Authors in reference (Ingwersen et al., 2018) extended Noah-MP by a dynamic crop growth component (Xinyou & Van Laar, 2005) for winter wheat and maize. Plants subjected to long-term or severe drought stress cannot reach the same level of transpiration after the cessation of a drought which can cause disagreement between the model and measured LE (Su et al., 2021).

At the domain scale, the inconsistency in evaporation between the models and MODIS in the central and western parts of Kansas shows that all models failed to simulate LE correctly over this region (Figure 2-7). This could be largely due to the discrepancies between prescribed and real land cover classes. Additionally, this could be attributed to shortcomings in the irrigation routine in Noah-MP, since irrigated croplands in the western part of Kansas enhance evapotranspiration. One must bear in mind that incorporating an improved land-cover dataset in the model is crucial to properly representing surface processes on both meteorological and climatological scales. In addition, previous studies (Heinsch et al., 2006; Miranda et al., 2017; Pu et al., 2020) have addressed the tendency of MODIS to overestimate LAI which may lead to miscalculation of vegetation cover fraction and overestimates of evaporation.

Compared to the field measurements, simulated SM from all model versions in 2018 shows larger disagreement in the middle of the growing season when leaves are fully developed, and the plant is able to transpire water approximately at rates equivalent to the atmospheric demand. This is accompanied by overall higher precipitation forcing in the model compared to 2012. Therefore, precipitation differences in early summer in 2018 represent a significant source of forcing condition uncertainty and cause a noticeable divergence between modeled and measured SM which remain throughout the year. A rapid shift in vegetation emergence than actual plant coverage implies that current Noah-MP versions are generally missing important processes, such as the negative lagged effect associated with warmer springs which consequently leads to the buildup of water stress (Buermann et al., 2018; O’Sullivan et al., 2020; Wolf et al., 2016). Again, mainly due to the spatial scale difference between satellite observations and model grids, there is a discrepancy between MODIS observation at the flux tower and simulated LAI in all the MODIS-LAI-based model versions.

The overall results show there is a major impact of rainfall forcing on all model versions. From simulations, it is evident that NLDAS-2 precipitation forcing significantly impacts the simulated latent heat fluxes of all model versions. The discrepancies in precipitation between NLDAS-2 forcing and gauge measurements exert a great impact on the general performance of the simulated compared to the observed LE and SM. At both sites, there is a clear response trend between the magnitude and timing of daily gauge-based precipitation and measured LE. Investigating the cumulative gauge-measured and NLDAS-2 precipitation of selected drought years indicates that not only is there a difference in terms of timing and magnitude of each event but also the total depth of annual rainfall. Furthermore, the gradual decline of water content in the topsoil layer results in a dramatic decrease in LE, especially during the drought years. However, the drought had little impact on LE simulation whenever there was sufficient water input from large precipitation events at the beginning of the growing season. The relative insensitivity of the model LAI to the overall LE suggests that the evolution of land surface models (LSMs) has focused more on obtaining correct surface fluxes instead of the accurate reproduction of SM products (Entekhabi et al., 2010). We should note that while NLDAS-2 may provide the most realistic retrospective forcing data, aggregating reanalysis, radar data, and rain gauge measurements into a grid, tends to crucially smooth precipitation in space and time (Luo et al., 2003). In North American mesic grasslands, precipitation is a strong driver of C4 grass productivity during the growing season (Brunsell et al., 2013; Wagle et al., 2015), which is reflected in a higher degree of carbon uptake, especially at the KON site.

In particular, this study shows that the difference in land-cover type has the potential to affect couplings between carbon and water fluxes at the land surface and alter land model simulations. It is also important to note that Noah-MP features four vegetation carbon pools (leaf, stem, root, wood), and two soil carbon pools (fast and slow) (Niu et al., 2011; Yang et al., 2011). Hence, updating the surface exchange coefficients and parameters specifically related to the dynamic vegetation components also plays a significant role in the determination of vegetation impact.

2.6 Conclusion

Multiple vegetation physics options available in Noah-MP LSM were evaluated on the overall skill of their model predictions over various land cover types. This study demonstrates the response of carbon and water fluxes to vegetation components (i.e., LAI and FVEG) based on 11 years of Ameriflux observations, particularly during two major drought events over the midwestern United States. Decomposing LE flux components reveals that the apparent insensitivity of simulated LE to LAI and dynamic vegetation process can be attributed to the tradeoff between soil evaporation and transpiration. Noah-MP employs a closed energy budget. In the presence of adequate soil moisture, incoming net radiation limits ET, and both sites are generally operating in an energy-limited regime. With high surface and root zone soil moisture, water can be extracted from the soil for evaporation and the total amount of evapotranspiration from each model remains similar which reflects constraints associated with Noah-MP that could be linked to the forcing. Overestimation of LE resulted in underestimation of runoff, especially over heavily cultivated basins that cover much of the western and central part of the state.

Although the Noah-MP LE and GPP differ from the observation datasets at the selected sites, it is still considered a satisfactory proxy of water and carbon fluxes in the absence of better estimates like flux tower measurements. Recent work by Kumar et al. (2019) and Mocko et al., (2021) have found that data assimilation of LAI into Noah-MP’s dynamic vegetation scheme improves the simulation of ET and GPP, particularly in the agricultural areas of the United States. LSMs include a myriad of surface processes and vegetation parameters that ideally would be regionally tuned, leading to difficulties in vegetation specification and uncertainties in their outputs, especially under extreme climate conditions like drought. Promising future model enhancements will potentially improve the model's ability to capture vegetation dynamic behavior, especially under extreme climatic conditions.

Chapter 3: Lake Stability Underpins Cyanobacteria Dominance in a Hypereutrophic Discontinuous Polymictic Reservoir

Hosseini, A., Roundy, J.K., Ladwig, R., and Harris, T.D., 2023. Lake stability underpins cyanobacteria dominance in a hypereutrophic discontinuous polymictic reservoir. Lake and Reservoir Management (under review).

3.1 Abstract

Cyanobacterial harmful algal blooms (CyanoHABs) pose a direct threat to water quality in lakes and reservoirs. CyanoHABs taxa have specialized traits like buoyancy control and nitrogen fixation that allow them to outcompete eukaryotic phytoplankton during periods of thermal stratification (i.e., water column stability) and nitrogen-limitation, respectively. This study investigates the relationship between water column stability and CyanoHABs in the hypereutrophic discontinuous polymictic Marion Reservoir, Kansas, from 2021 to 2022. High-frequency monitoring data for water temperature and dissolved oxygen (DO) combined with discrete measurements of water physicochemical properties (e.g., nutrients (N, P), redox-sensitive metals, light, pH, etc.) were collected throughout the water column. Relatively warm, calm wind days seemed to spur the development of near-surface (<1 m below the air-water interface) thermally uniform layers, which in turn directly helped favor buoyant cyanobacteria over eukaryotic algal competitors. Furthermore, our results demonstrate that atmospheric stilling in polymictic reservoirs affects the thermal mixing regime and water column DO concentrations. This can lead to internal phosphorus loading and decreased N:P ratios, which promote the dominance of CyanoHAB taxa in the phytoplankton community. Quantifying the role of atmospheric stilling in polymictic reservoirs led to better predictions of the phytoplankton community composition and could help integrate limnological processes into future climate models.

Keywords: Cyanobacterial harmful algal blooms (CyanoHABs), hypereutrophic, lake stability, polymictic, wind mixing

3.2 Introduction

The occurrence of algal blooms stresses freshwater ecosystems because of their ability to form dense biomass and produce toxins. It is estimated that harmful algal blooms impose approximately 1 billion dollars annually on the U.S. economy (Page et al., 2020). This is likely an underestimation given the estimate does not include the cost of removing cyanobacterial harmful algal blooms (CyanoHABs) and their metabolites from drinking water treatment plants (Wurtsbaugh et al., 2019).

Kansas contains 24 federal reservoirs that provide about 70% of the drinking water for the state (Rahmani et al., 2018). Reservoirs contribute substantial economic value to the state through flood control, irrigation, recreation, wildlife support, and power generation (Hargrove et al., 2010). CyanoHABs in Kansas have been shown to be dominated by Microcystis and several Anabaena genera, and there is evidence that these CyanoHABs comprised of these genera have recently increased across the state (Dzialowski et al., 2011). Kansas Department of Health and Environment (KDHE) has established three levels of threat advisory (i.e., Watch, Warning, and Hazard) based on cyanobacterial cell concentrations and microcystins concentrations in shore-based samples during CyanoHAB events. By 2021, the KDHE response program has investigated over 150 different water bodies and identified more than 50 lakes with at least one confirmed case that had exceeded HAB thresholds for cells and toxins (Figure 3-1; KDHE, 2002).

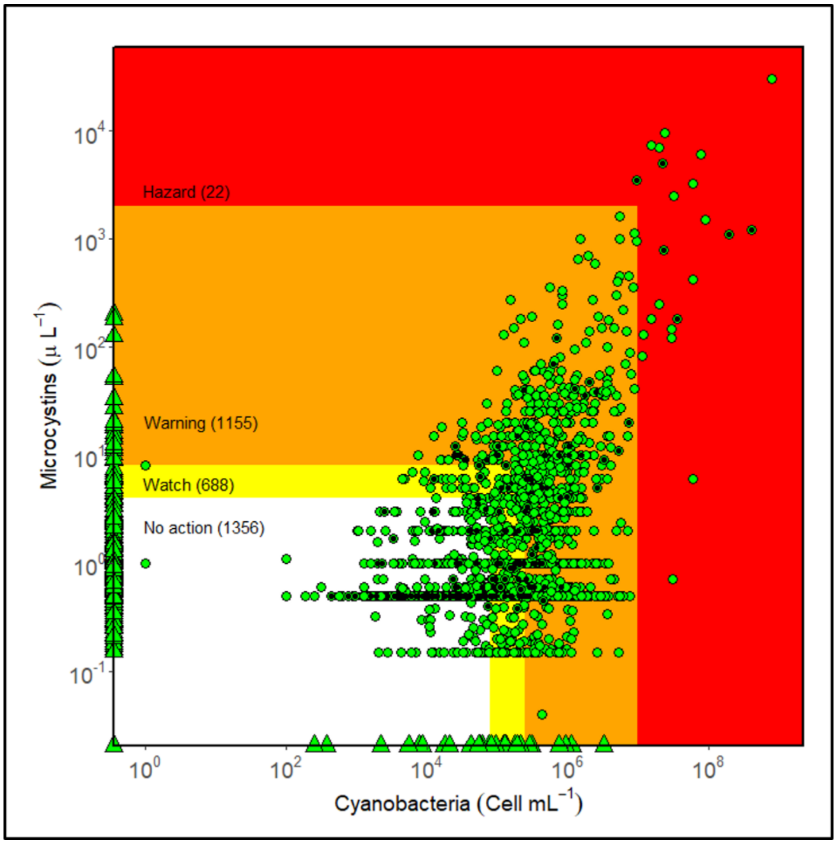

Figure 3-1:

The number of recreational sampling events on Marion (black dots) in context to all KDHE CyanoHAB sampling events by cyanobacterial cell count and total microcystins from 2010-2022. Colored graphic sections represent KDHE guidance value categories for CyanoHAB events; no action (white), watch (yellow, cell counts ≤80,000 (cells/mL) and microcystin toxin level ≤4 (µg/L)), warning (orange, cell counts ≤250,000 (cells/mL) and microcystin toxin level ≤ 8 (µg/L)), and hazard (red, cell counts ≥10,000,000 (cells/mL) and microcystin toxin level ≥ 2,000 (µg/L)). Triangles represent non-detect values.

CyanoHABs are the result of complex interactions among phytoplankton, nutrients, and biotic and abiotic factors. Cyanobacteria have unique traits compared to their eukaryotic algae competitors including the ability to control their buoyancy and fixation of atmospheric nitrogen (Oliver et al., 2012; Reynolds et al., 1987). These traits allow cyanobacteria to thrive under a wide range of light conditions and in phosphorus-rich conditions where nitrogen may become limiting to the phytoplankton community, which in turn gives cyanobacteria competitive advantages over other phytoplankton taxa. In turbid, light-limited eutrophic systems, cyanobacterial use their specialized buoyancy trait to gain a competitive advantage over eukaryotic competitors during periods of relatively strong thermal stratification, allowing cyanobacteria to rapidly proliferate (Ibelings et al., 2021).

Mechanical mixing (i.e., wind-driven) forces are considered a fundamental driver for biogeochemical processes in shallow aquatic ecosystems. In the absence of turbulent mixing, thermal stratification can promote hypoxic to anoxic conditions at the sediment-water interface (SWI; (Boehrer et al., 2008; Mellios et al., 2015; Singh et al., 2019). The establishment of anaerobic conditions decreases redox potential at the SWI, which in turn causes the dissolution of P-bound iron oxyhydroxides (FeOOH) and can lead to the ″internal loading″ of nitrogen (N) and phosphorus (P) from benthic sediments into the water column (Dodds & Whiles, 2010; Mortimer, 1941). Internal loading can also occur under aerobic conditions at the SWI under high pH conditions (>8 pH units; (Boström et al., 1988; Smolders et al., 2006; Søndergaard et al., 2003; Welch & Cooke, 2005). Internal P loading often results in the partial and delayed rehabilitation of water bodies in response to external anthropogenic nutrient loading reduction. Research conducted in Midwestern USA reservoirs has shown that external phosphorus (P) load is directly proportional to internal P load, suggesting that past external P loading into Kansas reservoirs can lead to increased internal P loading (Dzialowski et al., 2007). To accurately determine the initiation and persistence of cyanobacterial blooms, it is crucial to disentangle the effects of meteorological, physical, and bio-geochemical drivers in shallow aquatic systems. Nevertheless, gaining a deeper understanding of the dynamics of cyanobacterial blooms requires a comprehensive differentiation of the effects of these drivers in shallow aquatic systems. In this study, we analyzed the response of lake thermal and dissolved oxygen (DO) cycles to key meteorological factors and the effect of water column mixing on nutrient, metal dynamics, and consequently emergence and propagation of CyanoHABs using high-frequency data from a hypereutrophic discontinuous polymictic reservoir. We further explored a range of indices and statistical approaches to recommend a diagnostic approach to predict relative cyanobacteria abundance that can be applied to other shallow lakes and reservoirs.

3.3 Material and Methods

3.3.1 Study Site

Marion Reservoir is a 25.13 (km^2) impoundment constructed by the Tulsa District, U.S. Army Corps of Engineers (USACE) on the Cottonwood River in Marion County, Kansas in 1968 (Figure 3-1). The reservoir is polymictic and has a mean depth of 3.4 m (maximum depth= 9.0 m; KDHE, 2002). The North Cottonwood River and its tributaries drain 82% of the watershed while the French Creek watershed comprises 18% of the remaining drainage area (Barnes & Devlin, 2008). The reservoir is a multi-purpose impoundment for flood control, water supply, and recreation, and is a primary source of drinking water for people in Marion County and surrounding communities (Mosher, 2000).

The combination of long-term external nutrient loading from the agriculturally dominated ~ 530 km2 watershed (predominantly cultivated row crops (43%) and grassland (40%)), subsequent internal loading, and relatively high surface area to volume ratios (i.e., shallow) has resulted in optimal conditions for CyanoHAB development (KDHE, 2002). The first record of a CyanoHAB event occurred in 2003. The 2003 bloom exceeded the World Health Organization's recommended guidelines value for cells per milliliter by 337-fold. Since the 2003 bloom, CyanoHABs have been frequently reported in Marion (Harris et al., 2020). In the summers of 2012, 2013, 2017, and 2022, CyanoHABs exceeded the KDHE recreational guidelines for the watch, warning, and hazard advisory levels in Marion Reservoir multiple times (Figure 3-1).

3.3.2 *Data Collection*

We used hourly weather data from the USACE station located near the reservoir dam. Meteorological data include air temperature (°C), wind speed (m/s), and precipitation (m/day). All meteorological data were provided hourly. Bathymetric data were collected in 2008 by the Kansas Biological Survey (KBS, 2010).

In-situ Continuous Sampling. A high-frequency monitoring buoy that collected measurements hourly was installed near the dam (Figure 3-1) in two separate sampling campaigns from 2021 to 2022. During the spring of 2021, a monitoring buoy was installed at Marion Lake near the deepest point in the lake (dam buoy, ~8 m). Dissolved Oxygen (DO) and water temperature were measured from May 26 - November 15, 2021, and May 18 - October 5, 2022, using both miniDOTs and HOBO loggers (Precision Measurement Engineering, Inc. (PME), Vista, CA, USA; Onset, Bourne, MA, USA).

MiniDOT loggers measured DO and water temperature from 0.2-0.3 m below the surface up to approximately 0.5 m above the sediment-water interface at 1-1.5 m depth increments. Note that the depth of the sensors had to be slightly adjusted over time depending on the number of available working data loggers and reservoir depth. The temperature values were measured using HOBO tidbit v2 temperature loggers with a nominal accuracy of ±0.21 $^{\circ}$C. The buoy was equipped with sensors placed along a line that anchors to a modified metal wagon wheel, which was designed to lay flat on the lake bottom and prevent the two bottommost sensors from being buried by sediment (Figure 3-2). MiniDOTs were deployed with wipers to avoid biofouling.

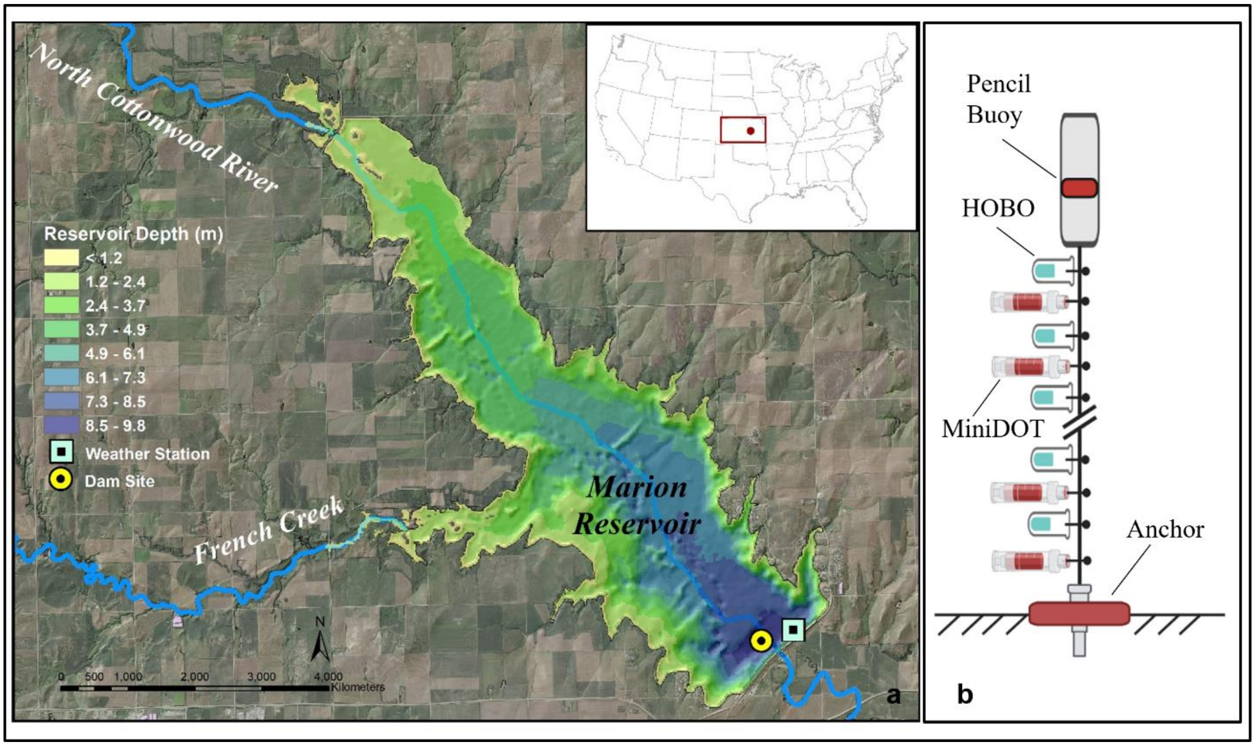

Figure 3-2:
a) Location of Marion reservoir in Kansas showing two major inlet streams including a bathymetric map, location of the monitoring buoy (yellow dot), and weather station operated by U.S. Army Corps of Engineers (blue square). b) Mooring scheme with the positions of the scientific instruments labeled along the instrument string.

In-situ Discrete Sampling. Vertical distribution of phytoplankton communities was measured using FluoroProbe III (FP; bbe Moldaenke GmbH, Kiel, Germany). This device segregates spectral emission of chlorophyll a (chl-a) concentrations of four phytoplankton groups based on their fluorescence excitation spectra: green algae (Chlorophyta and Euglenophyta), diatoms (Chrysophyta), cyanobacteria (Cyanophyta), and Cryptophyta (for a review of spectral fluorescence phytoplankton quantification methods, see Harrison et al., 2016; Lofton et al., 2020; MacIntyre et al., 2010). While the use of a portable instrument such as the FluoroProbe comes with some caveats, in the absence of labor-intensive and time-consuming microscopic analysis it provides rapid fluorescence-based biomass of phytoplankton communities and their abundance within the water column. FluoroProbe readings were expressed as relative fluorescence units

(RFU), which are directly proportional to concentrations of the respective pigments (Pace et al., 2017). Bloom initiation phase was defined when cyanobacteria accounted for more than 50 percent of total chlorophyll a (chl-a) concentration measured by the FluoroProbe.

A suite of parameters including temperature, conductivity, pH, salinity, turbidity, oxidation-reduction potential (ORP), and total dissolved solids of the water column was measured at each site visit with Horiba U-53 multiprobe (2021 until November) and later (after November 2021) with the YSI ProDSS multi-parameter sonde. Each probe was first lowered to about 0.5 m below the surface water; taking measurements at a 1m interval up to a depth of 10 m (the probe was allowed to stabilize before recording each measurement). Data from the entire profile were divided into two layers based on depth (i.e., less than 3 m (top), and more than 6 m (bottom) layers). Both sondes were calibrated independently according to manufacturer instructions each day before the start of field measurements (YSI ProODO 2015 & YSI ProDSS 2015; Gardner, 2017).

Discrete water quality samples were collected with a nonmetallic Van Dorn vertical water sampler from two different depths (surface at approx. 1m and bottom at approx. 7.5 m) and stored using 125-mL high-density polyethylene (HDPE) bottles. Each vial was triple rinsed with reservoir water, filled with samples, and placed on the ice during travel back to the laboratory, then frozen and sent to the Kansas State University (KSU) Soil Testing lab. Samples were analyzed for total nitrogen (TN) concentrations, total phosphorus (TP) concentrations, total Iron (Fe), and total Manganese (Mn) based on the Standard Methods for the Examination of Water and Wastewater (APHA/AWWA/WEF 2005).

The light extinction was determined by lowering a handheld light meter (LI-1500, LI-COR, Lincoln, NE, USA) on the sunny side of the boat, at 0.5 m increments from just below the water surface (0 m depth) until the readings were 1 percent of the light at the water surface.

3.3.3 Data Preprocessing and Stability Metrics

To ensure the quality of the measured temperature and DO, we neglected all data for two hours before and after the time when the buoy was pulled out of the water for cleaning and downloading data. Additionally, no gap-filling of the data was used to avoid creating data artifacts. Anomalous data were identified based on the field sheet notes, visual inspection, and recorded observations that imply dislocation or failure of the buoy (i.e., physical interruptions such as destruction or movements of sensor devices caused by humans or animals). It should be noted that any data-cleaning approach that relies on human interpretation is inherently subjective. Quantitatively, any observation more than 3 standard deviations away from the mean was considered an outlier and excluded from the dataset (Pearson, 2002).

Both temperature and DO profiles were vertically interpolated to a regular vertical grid with 0.5 m increments with a uniform hourly resolution for each year measurement period from the surface to the bottom of the lake using the linear interpolation method to approximate missing data at specific depths due to sensor failure.

The Li-COR photosynthetically active radiation (PAR) data with depth were fitted to a linear regression based on the Lambert-Beer equation (Eq. 1: Kirk 1983) to calculate the light extinction coefficient:

$$K_d = ln\,(\frac{I_z}{I_o})\,\frac{1}{z} \qquad (1)$$

where I_o and I_z are light intensities at the surface (0 m depth) and z is depth in meters, respectively. The coefficient (K_d) is then used to determine the depth of the euphotic zone (Z_l, the depth where 1% of the incident surface photosynthetic active radiation arrives). In the absence of PAR measurements, K_d is approximated from the empirical relationship based on Secchi depth measurements (Cole & Kilham, 1975) as:

$$K_d \sim 1.7/Secchi_{Depth} \qquad (2)$$

Data from 2021 illustrate that the relationship between K_d calculated by the Lambert-Beer equation and K_d estimated from the empirical model is acceptable ($R^2 = 0.57$).

Using the interpolated temperature profiles together with the bathymetric data, we calculated the stability metrics Schmidt Stability (St), LakeNumber (L_N), buoyancy frequency (N^2), and a heat budget ratio (HBR).

St (J/m^2) is a measure of the work required to fully mix a thermally-stratified water column to an isothermal state. The higher the Schmidt stability index, the more severe stratification:

$$S_t = \frac{g}{A_s}\int_0^{z_m}(z_v - z)A_z\rho_z dz \qquad (3)$$

where g is the gravitational acceleration (9.81 m/s), A_s is the surface area (m^2), z_m is the maximum depth (m), A_z is the respective area at depth z, ρ_z is the respective density at depth z (kg/m^3), z_v is the depth of the center of volume ($z_v = \frac{1}{V}\int_0^{z_m}(A_z z dz)$), and V is the volume ($m^3$).

L_N is a dimensionless number representing the ratio of stratification strength to overturning wind forcing and takes into account lake volume and the density profile. With a critical value of one, $L_N < 1$ indicates weak and $L_N \geq 1$ reveals stronger stratification with respect to wind stress (Coman & Wells, 2012).

$$L_N = \frac{S_t(zm_1 + zm_2)}{2\rho_h u_2^* A_s^{\frac{1}{2}} z_v} \qquad (4)$$

Where ρ_h is the average water density at hypolimnion (kg/m^3), u_2^* is wind friction velocity (m/s), zm_1 and zm_2 (m) are the depths to the top and bottom of the metalimnion, respectively.

N^2 ($1/s^2$) is the squared buoyancy which represents the local stability of the water column through the oscillation frequency of a parcel of fluid when displaced based on the vertical density gradient. A high squared frequency indicates strong stratification (Read et al., 2011; Waldo et al., 2021).

$$N^2 = \frac{g}{\rho} . \frac{d\rho}{dz} \qquad (5)$$

Where ρ is water density (kg/m^3) and z is depth (m) and $\frac{d}{dz}$ presents density gradient.

We defined a heat budget ratio (HBR) to compare the amount of needed energy to maintain isothermal conditions to the amount of available external energy by wind (Kjensmo, 1994; Ladwig et al., 2021). The HBR is presented as the sum of the required energy to mix a density profile to a fully mixed state without affecting the amount of internal energy (i.e., Schmidt Stability, St) and the energy needed to produce a given thermal stratification from fully mixed conditions (i.e., Birgean work, B, J/m^2), to only B. This ratio compares the amount of energy required to maintain isothermal conditions to the amount of available mechanical external energy, mainly exerted by wind (Kjensmo, 1994). Increased water column stagnancy results in a reduced exchange of fluxes between the surface mixed and bottom layer. Birgean work and Schmidt's stability are complementary quantities demonstrating work done through the lake surface: first, to form a vertical density gradient from a hypothetical initial condition, and then to form or break up that stratification without further exchange of heat or solute (Ferris & Burton, 1988). Therefore, HBR values >1 indicate the bottom water layers are isolated from the surface fluxes in a lake.

$$HBR = \frac{S_t + B}{B} = \frac{\frac{g}{A_S}\int_0^{zm} A_z(1-\rho_z)(z_v - z)dz + \frac{g}{A_S}\int_0^{zm} A_z(1-\rho_z)\, z\, dz}{\frac{g}{A_S}\int_0^{zm} A_z(1-\rho_z)\, z\, dz} \qquad (6)$$

Thermocline depth, St, L_N, and N^2 were estimated using the R package ″rLakeAnalyzer″ (Read et al., 2011; L. Winslow et al., 2018). All statistical analyses and figures were prepared using R 4.2.2 (R Development Core Team, 2008).

3.4 Statistical Analysis

After initial quality control screening, 26 sampling events were observed over the 2-year study period. Although we sampled 22 parameters over the course of the study, we used a subset of the dataset to include only parameters that indicate and influence cyanobacterial blooms (Table *3-1*). All other parameters are listed in Table *3-2*.

Table 3-1:
Measured parameters, units, methods, or analysis equipment used in this study during the 2021-2022 campaigns at Marion Reservoir.

Parameter	Abbreviation	Unit	Method/Equipment
Oxidation Reduction Potential	ORP	mV	Horiba U-53/YSI ProDSS
Total Phosphorous Concentration (1, 7.5 m)	Top.P Bottom.P	mg/L	Standard Method 4500-P
Total Nitrate Concentration (1, 7.5 m)	Top.N Bottom.N	mg/L	Standard Method 4500-N
Total Iron Concentration (1, 7.5 m)	Top.Fe Bottom.Fe	mg/L	Standard Method 3500-Fe
Total Manganese Concentration (1, 7.5 m)	Top.Mn Bottom.Mn	mg/L	Standard Method 3500-Mn
Dissolved Oxygen	DO	mg/L	MniDOTs Loggers
Water Temperature	WaterTemp	°C	HOBO/MniDOTs Loggers
Euphotic Zone	Z_l	m	LI-1500
Air Temperature	AirTemp	°C	USACE
RH	RelHum	%	USACE
Wind Speed	WS	m/s	USACE

Table 3-2:

All of the measured parameters, units, methods, or analysis equipment during the 2021-2022 campaigns at Marion Reservoir.

Parameter	**Abbreviation**	**Unit**	**Method/Equipment**
Conductivity	*Cond.*	*mS/cm*	*Horiba U-53/YSI ProDSS*
Turbidity	*Turb.*	*NTU*	*Horiba U-53/YSI ProDSS*
Salinity	*Sal.*		*Horiba U-53/YSI ProDSS*
Oxidation Reduction Potential	*ORP**	*mV*	*Horiba U-53/YSI ProDSS*
pH	*pH*		*Horiba U-53/YSI ProDSS*
Total Phosphorous Concentration (1, 3, 7.5 m)	*Top.P** *Middle.P* *Bottom.P**	*mg/L*	*Standard Method 4500-P*
Total Nitrate Concentration (1, 3, 7.5 m)	*Top.N** *Middle.N* *Bottom.N**	*mg/L*	*Standard Method 4500-N*
Total Iron Concentration (1, 3, 7.5 m)	*Top.Fe** *Middle.Fe* *Bottom.Fe**	*mg/L*	*Standard Method 3500-Fe*
Total Manganese Concentration (1, 3, 7.5 m)	*Top.Mn** *Middle.Mn* *Bottom.Mn**	*mg/L*	*Standard Method 3500-Mn*
Dissolved Oxygen	*DO**	*mg/L*	*MniDOTs Loggers*
Water Temperature	*WaterTemp**	*°C*	*HOBO/MniDOTs Loggers*
Lake Depth	*Lake_depth*	*m*	*Handheld Depth Finder*
Euphotic Zone	*Zl **	*m*	*LI-1500*
Secchi Depth	*Secchi_depth*	*m*	*Secchi Disk*
Air Temperature	*AirTemp**	*°C*	*USACE*
Relative Humidity	*RelHum**	*%*	*USACE*
Wind Speed	*WindSpeed**	*m/s*	*USACE*
Wind Direction	*WindDir*	*deg*	*USACE*
Precipitation	*Rain*	*mm*	*USACE*
Total Suspended Solids	*TSS*	*mg/L*	*Standard Method (APHA) 2540D&E*
Volatile Suspended Solids	*VSS*	*mg/L*	*Standard Method (APHA) 2540D&E*
Non-Volatile Suspended Solids	*NVSS*	*mg/L*	*Standard Method (APHA) 2540D&E*

Note. The asterisk (*) is used to indicate focus parameters in this study.

3.4.1 Correlation Coefficient Analysis

To explore the relationships between the relative abundance of cyanobacteria with daily average biotic and abiotic parameters and overall lake stability indices, a correlation matrix was calculated. Spearman correlation matrix of the main important attributes was calculated using *rstatix* (Alboukadel, 2021) and plotted using *corrplot* (Wei et al., 2017). Attributes with a coefficient p-value of less than 0.05 are considered to be significantly correlated.

3.4.2 Decision Tree

To investigate the predictive power of each biotic and abiotic parameter and stability metrics to determine the relative abundance of cyanobacteria, decision tree analysis was performed using the R-package *rpart* (Therneau et al., 2019). Relative abundance of cyanobacteria (PerCyano) as the percentage of total chl-a concentration measured by the FluoroProbe was classified into three groups, low (≤ 40 %), medium (41-65 %), and high (≥ 65 %). In rpart the three parameters were modified to obtain a desirable tree size: *minbucket* = 3, *maxdept = 3,* and complexity parameter (*cp*) = 0.01. *minbucket* indicates the minimum number of observations in any terminal node and *maxdepth* sets the *maximum depth of any node of the final tree,* with the root *node* counted as *depth* 0 (Zhou & McArdle, 2015). *cp* controls the complexity of the model which imposes a penalty on the *tree* for having too many *splits*. This means that if a split does not decrease the overall model fit with the threshold of *cp*, this split will not be carried out. Thus, large *cp* values increasingly limit the number of splits and complexity of the tree (Bartz et al., 2021). Three decimal numbers in the middle of the nodes display the proportion of observations in each class that fall into the designated Cyanobacteria percentage group. Therefore, the color gradient is a visual representation of these numbers, with more intense colors with more correct classifications. At the bottom of each note, the percentage of total observations that ended up being in that node is given (rounded to an integer). The confidence in model performance accuracy is summarized in a 3×3 contingency table. In this table, the forecasts are represented by columns, and the rows represent the observations. The entries in the table represent the number of times the model has *correctly* predicted the risk category (i.e., hits) out of the total number of forecasts. The darker colors indicate subtle differences between observation and model, whereas lighter colors mark larger differences. Due to the limited number of measurements, all of the data was used to build a *tree* structure, and the dataset was not divided into the train and test sets. This results in a decision tree model that is useful for analyzing the relationship between CyanoHABs and potential predictors but is limited in its ability to be a true prediction model.

3.5 Results

The goal of our study is to identify the drivers of water column stability that impact CyanoHAB initiation and persistence in the shallow reservoir. In the following sections, we first analyze field data and define the initiation and duration of CyanoHABs (where PerCyano >50%) based on the observed patterns in thermal, DO, stability indices, and metal and nutrient dynamics. Subsequently, we present statistical approaches to highlight proximal CyanoHAB drivers.

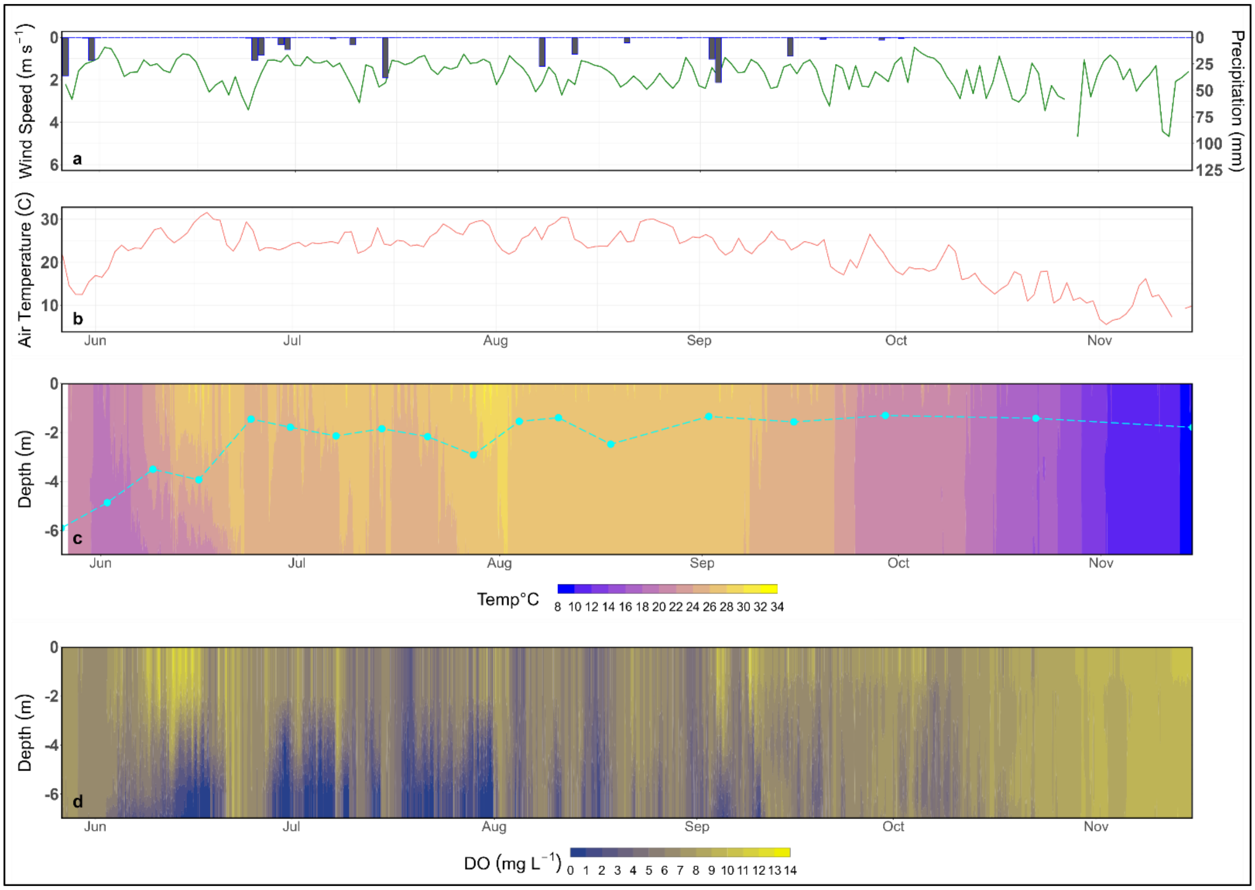

Figure 3-3:

Daily averaged meteorological data where: (a) cumulative precipitation (blue bars) and wind speed (green line), (b) air temperature, (c) thermal structure, and (d) dissolved oxygen (DO) depth profiles of the lake using the high-frequency data with a 1-h between 27 May and 15 November 2021. The cyan dashed line in time–depth profile of water temperature indicates the depth of the euphotic zone (zl).

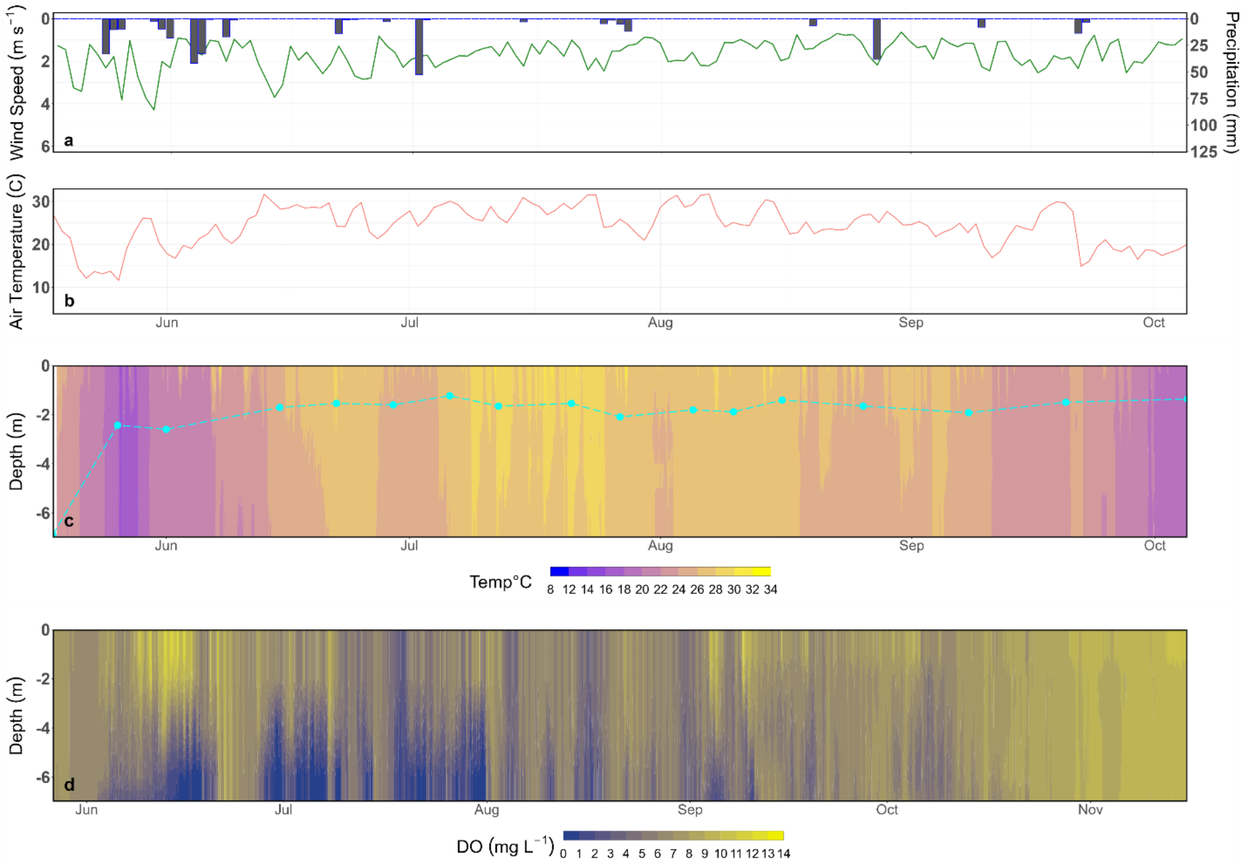

Figure 3-4:
Daily averaged meteorological data where: (a) cumulative precipitation (blue bars) and wind speed (green line), (b) air temperature, (c) thermal structure, and (d) dissolved oxygen (DO) depth profiles of the lake using the high-frequency data with a 1-h interval between 15 May and 5 October 2022. The cyan dashed line in time–depth profile of water temperature indicates the depth of the euphotic zone (zl).

3.5.1 Water Temperature and DO Response to Meteorological Drivers and Lake Stability

We examined relationships among main meteorological factors (e.g., air temperature, precipitation, and wind speed), thermal characteristics, and DO distribution throughout the water column in Marion reservoir during 2021 and 2022 monitoring campaigns (Figure 3-3 and Figure 3-4). The water column remained isothermal before June and after mid-October in both monitoring years. During the first two weeks of June 2021, there was a rapid rise in air temperature (about 10 °C) followed by calm wind conditions (wind speeds less than 2 m/s) and no precipitation, which triggered distinct thermal stratification. The rapid increase of air temperature and consequently water temperature in conjunction with low wind-induced turbulence resulted in the maximum St and L_N during this time (Figure 3-5).

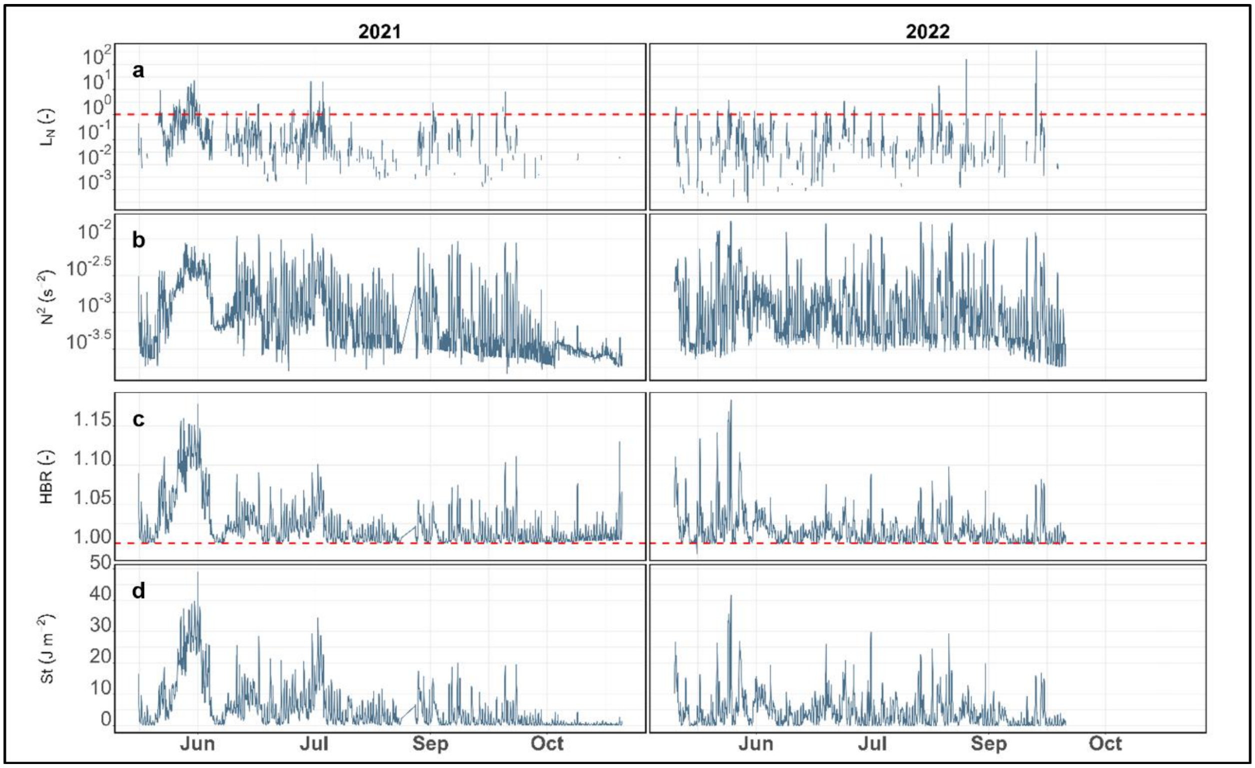

Figure 3-5:
Time series of (a) log lake number (L_N), (b) log buoyancy frequency squared (N2), (c) heat budget ratio (HBR), and (d) Schmidt's stability (St) during 2021 and 2022 campaigns. A Horizontal dashed red line indicates L_N and HBR of 1, whereas L_N and HBR <1 generally indicate a system is prone to wind-driven mixing.

Concurrently, DO concentration reached almost 12 mg 1/L in the upper 2 m layer during the daytime, then decreased rapidly from 3 m water depth and reached hypoxic conditions (DO < 2 mg/L) near the bottom. This relatively short stable period was disrupted by an increase in wind speed (WS > 3 m/s) and rainfall (about 30 mm/day). The stability metrics (i.e., St, L_N, and N^2) and HBR increased over the stratification period during the early weeks in June in both years (Figure

3-5). However, early summer stratification was noticeably stronger (multiple days with $L_N > 1$) in 2021 compared to 2022. In addition, more days with wind speeds greater than 2–3 m/s and intense precipitation events during the summer of 2022 caused frequent turbulent mixing and less intense stratified periods. Whenever L_N is small ($L_N < 1$), the buoyancy frequency (N^2) decreases rapidly, and the water column remains well-oxygenated.

In 2022, for approximately two weeks from the end of July until the first week of August, the DO level dropped below 2 mg/L at the bottom of the epilimnion (Figure 3-4). During this time sufficient duration of calm days (average wind velocity <2 m/s) hampered mixing of the entire water column and promoted a deepening of the thermocline. A distinct temperature difference was also observed between the upper mixed layer, the middle, and the near-bottom layer (from 27 to nearly 23 °C) from July 28 through August 2.

In both years, during autumn (from September until the end of the measurement season), water temperatures dropped by more than 4 °C compared to August and allowed the system to mix more rapidly. However, whenever warming was re-established and episodic wind speed was mild (WS < 2 m/s), a weak shallow (thermocline depth < 2 m) stratification formed (Figure 3-3 and Figure 3-4).

Higher HBR values (HBR > 1) indicate the isolation of the bottom water layers from surface fluxes in the lake. However, it should be noted that HBR covers a very narrow range (0.98 - 1.18) for Marion Reservoir. Schmidt stability values close to zero portray weak thermal stability and periods indicating overturn. The peak of HBR, as well as the hypolimnetic anoxic area, occurred during the first strong stratification in early summer. However, this pattern is more evident in 2021 than in 2022 (Figure 3-5).

In both years, light penetration prior to the bloom was relatively deep ($Z_l > 6$ m). In 2021, the depth of the photic zone first decreased moderately to about 4 m at the beginning of the summer and then to 2 m towards the end of June. In 2022, the euphotic zone was slightly deeper ($Z_l \approx 6.8$ m) in the middle of May but was substantially reduced to 2 m a week later and remained the same until mid-October (Figure 3-3 and Figure 3-4).

3.5.2 Phytoplankton Community Composition

Phytoplankton abundance and community composition changed over the study period, with links between thermal stratification and CyanoHAB formation. Before the early summer stratification, green algae exhibited community dominance (>50%) in both years (Figure 3-5). A rapid increase in PerCyano ($\geq$25 % to $\backsimeq$ 70%) occurred in the second week of June 2021, but in 2022 PerCyano increased gradually over four weeks and reached a maximum (~ 90%) in the middle of June (Figure 3-5). A high concentration of DO in the epilimnion at this time also reflects increased phytoplankton photosynthetic activities. From early September, the community dominance shifted from cyanobacteria to diatom and green algae; however, unlike late spring and early summer, cyanobacteria never regained phytoplankton community dominance after a complete mixture of the water column.

3.5.3 Metal, Nutrient, and Water Quality

We evaluated the variation of redox-sensitive metals such as manganese (Mn) and iron (Fe), ORP, water column TN, and TP concentrations, and their ratio (i.e., TN:TP), during 2021 and 2022 campaigns in Marion reservoir (Figure 3-6). The maximum concentration of TP and total Fe were slightly higher in 2022 compared to 2021 but the average maximum concentration of TN did not change between two years.

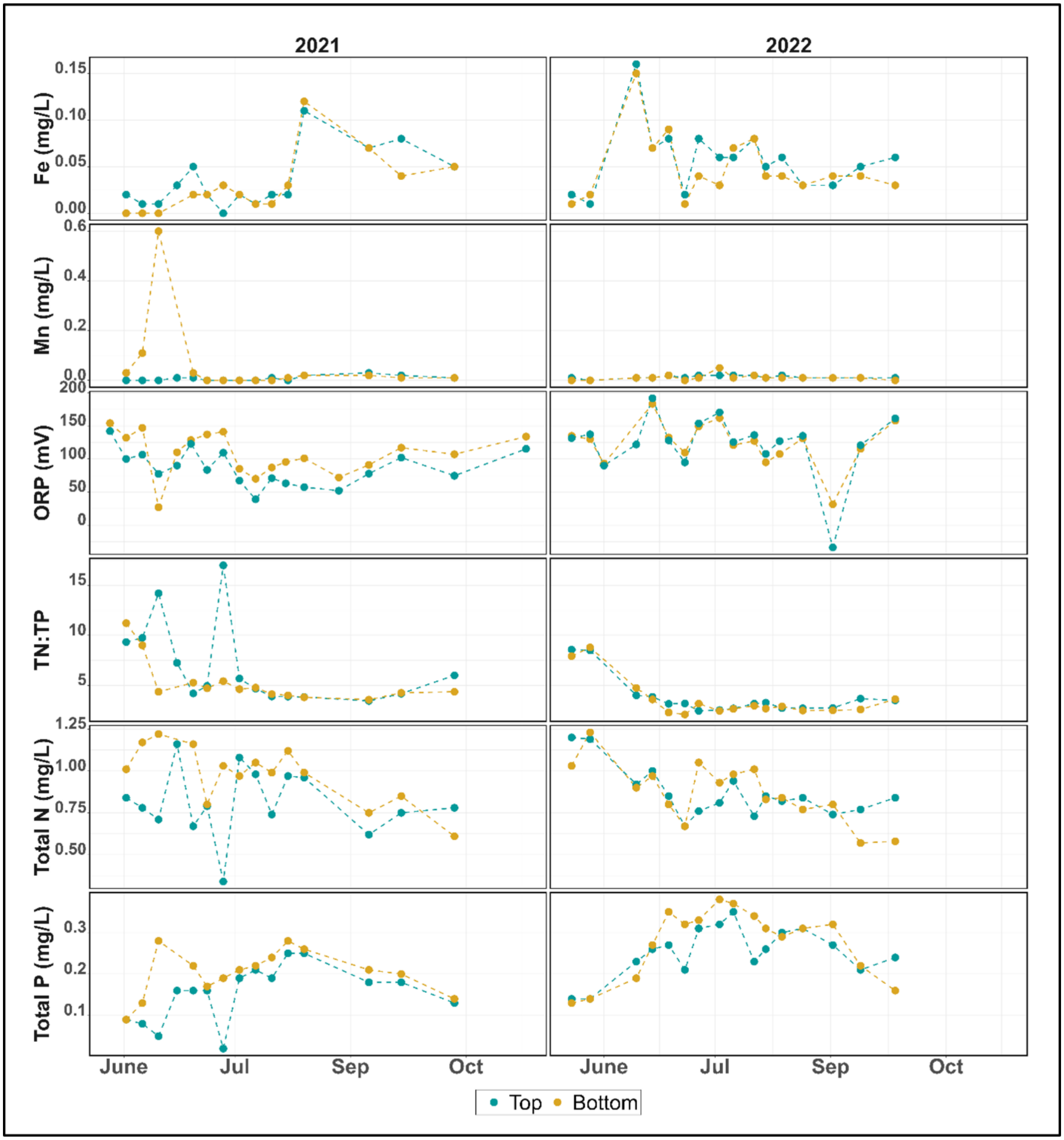

Figure 3-6:

Temporal dynamic of total Iron (Fe), total Manganese (Mn), oxidation-reduction potential (ORP), nutrient ratio (TN:TP), total Nitrogen (TN), and total phosphate (TP) concentration during 2021 and 2022 campaigns. Blue and yellow colors represent the top and bottom layers, respectively.

Dissolved Mn concentrations remained below detection (<0.001 mg/L) in the entire water column before summer (June 1) in both years. The highest Mn concentration (~0.6 mg/L, 30-60 times higher than the rest of the measurements) was recorded on June 16, 2021, in the hypolimnion (bottom layer), which coincided with L_N values >1, near-bottom ORP decreasing from 150 to 30 mV, and a dramatic increase in PerCyano (Figure 3-7). This sharp increase in L_N and the concurrent decline in ORP was well correlated with the relatively high concentration of P (~0.3 mg/L) and Mn in bottom waters, which seemed to indicate an internal loading of nutrient and metals from the sediment-water interface (SWI) during this phase (Figure 3-6). Similar patterns in L_N and ORP were not observed among the water column in 2022.

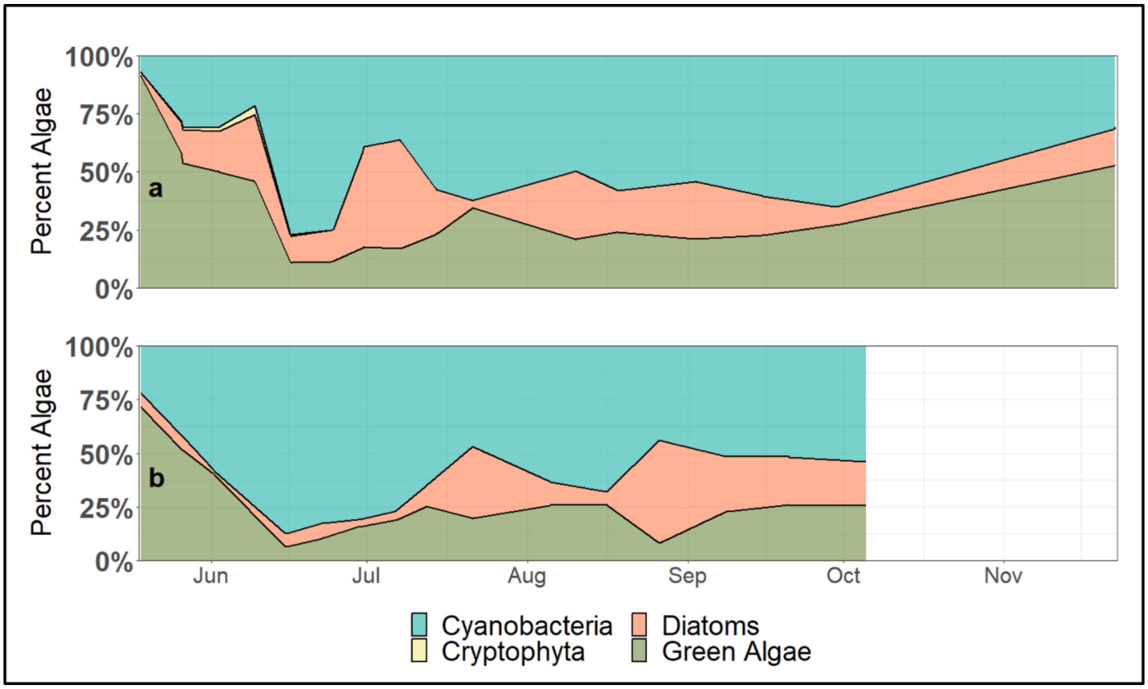

Figure 3-7:
Stacked area charts reflect the composite algal community by percent relative abundance over time. (a) May–November 2021 and (b) May–October 2022. Blank spaces indicate the difference between the duration of data collection campaigns.

Noticeable differences between TP concentration and TN:TP ratio in the upper and bottom layers were observed during stratified periods which follow the pattern of bloom onset and persistence, especially in summer months (Figure 3-6). The lower value of TN:TP (~ 5) in the hypolimnion during bloom onset in 2021 indicates the higher amount of released P from the sediment relative to N due to longer stratification in early summer (Figure 3-6). The separation between TN and TP from the upper and lower layers is more evident during bloom initiation in early summer. For instance, on July 16, 2021, TN and TP concentrations in the bottom layer (~ 7 m depth) were nearly 1.5 and 3 times higher, respectively, than the close values from the top layer. From the last week of July until the end of the 2021 sampling campaign, and during the entire summer and autumn of 2022, TN:TP ratios were less than 5 which likely indicates nitrogen-limited conditions in Marion Reservoir (*sensu* Dzialowski et al., 2005). In contrast, the TN:TP ratio remained similar between the top and bottom in 2022.

3.5.4 Contributions of Influencing Factors to CyanoHABs

Cyanobacteria percentage exhibited a significantly positive correlation with top and bottom Fe, bottom P, and a negative correlation with HBR index, Z_l, and bottom TN:TP ratio (Figure 3-8). The highest positive correlation was found between Cyanobacteria percentage and bottom Fe (r = 0.58). Although from observations wind velocity was considered to induce water column mixing and impact cyanobacteria distribution, its p-value was slightly above the chosen significance threshold (0.058 > 0.05) and was not statistically significant.

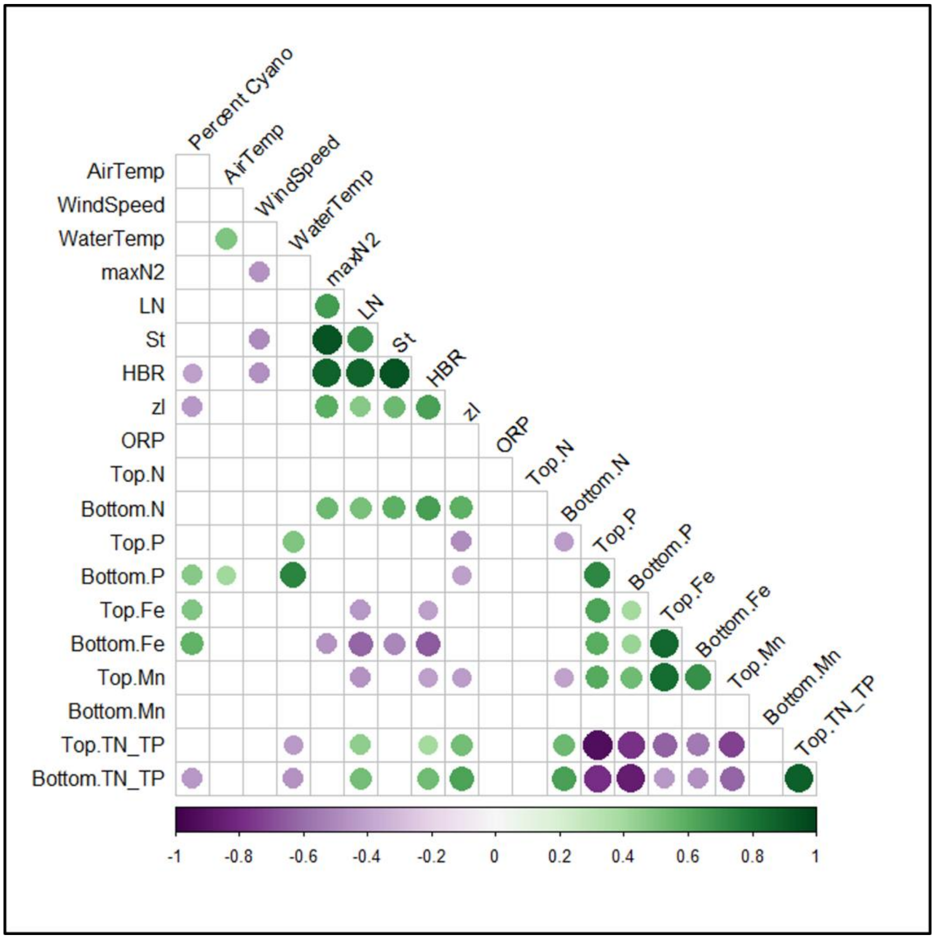

Figure 3-8:
Correlation matrix for measured variables and indices used to analyze drivers of cyanobacteria bloom in Marion reservoir. Both the size and color of the circles indicate the strength of Spearman's correlation coefficient between any two given variables. Blank boxes indicate non-significant correlations (P-value > 0.05). All cases with missing data were omitted from the analysis.

According to the decision tree, hypolimnetic total phosphorus (TP) concentration (hence internal nutrient loading) was the most important parameter to predict PerCyano. When near-bottom TP (~ 7 m) was <0.14 mg/L, PerCyano probability is characterized as low (<40%). When TP in the bottom layer was ≥0.14 mg/L, and the air temperature was <23 °C, PerCyano probability was medium (41-64 %). If the air temperature was greater than 23 °C and Z_l <1.8 m, PerCyano probability was high (>65%). With the highest value of successful model forecast (i.e., number of hits =10), the contingency table shows that the model is able to classify the medium CyanoHAB group better than the other classes (Figure 3-9).

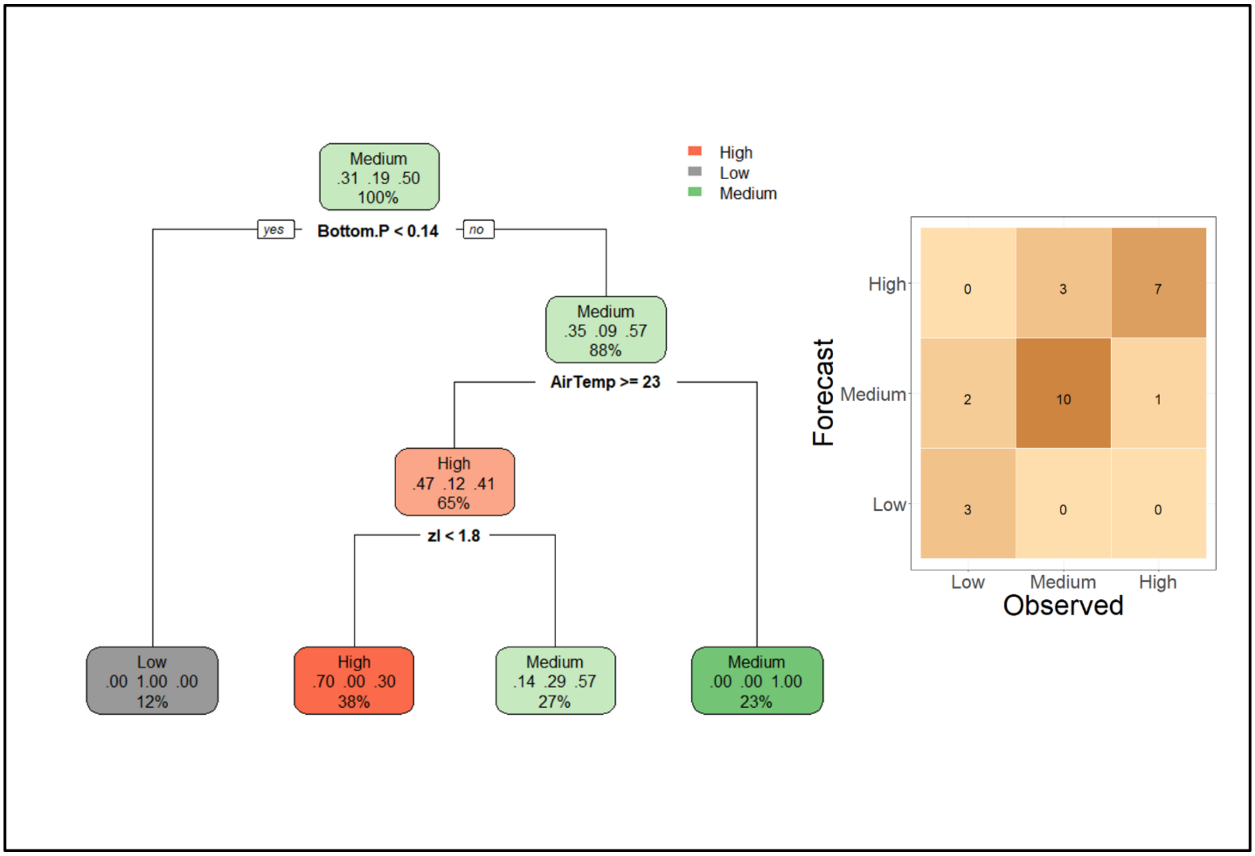

Figure 3-9:
Decision tree analysis showing key drivers (i.e., Bottom (~7 m) Phosphorus, air temperature, and euphotic zone (Zl) influencing changes in relative cyanobacteria abundance trends. (Left) Each terminal node presents the predicted class (High (>60%), Medium (41-59%), and Low (<40%)) in the top row, the predicted probability of each class in the middle row, and the percentage of observations in the node in the bottom row. (Right) Contingency table describing the comparison between the forecasts and observations for each CyanoHAB risk category, with darker colors representing greater prediction forecasts.

3.6 Discussion

Our results from a 2-year high-frequency time-series monitoring campaign highlight that relatively calm weather (WS < 2 m/s) and relatively strong thermal stratification ($L_N > 1$) increased the probability of CyanoHABs. However, no significant statistical correlation was found between wind speed and CyanoHABs, perhaps due to the time and the limited number of field samples. Nonetheless, the combination of warmer temperatures (average daily air temperature >23 °C) and atmospheric stilling (the decrease in near-surface wind speed) amplified stratification in lakes as it reduces mechanical energy fluxes at the water surface-atmosphere interface and consequently the degree of vertical mixing. This condition favored the formation of CyanoHABs on the surface of the water column, subsequently restricting light penetration, and increasing near-bottom dissolved oxygen consumption in turn causing internal P loading in the polymictic Marion Reservoir.

Dynamic changes throughout the monitoring period in thermal density gradients, or the lack thereof, substantially changed due to meteorological factors (Air temp > 23 °C and WS < 2 m/s) within the polymictic Marion Reservoir. Although the reservoir was isothermal for the majority of the study period, relatively weak stratification (L_N close to 0) occurred on most days with relatively high temperatures and low wind speeds; however, relatively light wind action (WS > 2 m/s) was able to disrupt thermal stratification. These results are in agreement with Stefan et al. (1996) and Woolway et al., (2017) who identified that a decrease in wind speeds has resulted in substantial changes in stratification dynamics. In general, Birgean work is higher than Schmidt stability in shallow lakes (Ambrosetti & Barbanti, 2002; Kjensmo, 1994; Nõges et al., 2011). In Marion Reservoir, Birgean work was on average 50 times higher than St, with St at or close to zero the majority of the time, in turn causing HBR to have a relatively small range of variation (Figure 3-5). However, the moments of maximum stability and wind work coincide and generally occur in early summer (first weeks of June), depending on the respective meteorological conditions. Variations of the lake stability indices (e.g., St, L_N. N^2, and HBR) reveal changes in water column de-stratifying forces that weaken vertical density gradients (decrease in buoyancy frequency), availability of metal/nutrients, vertical light distribution, microbial substrates, and consequently biological processes. The correlation between N^2 (i.e., larger positive values mean stronger thermal stratification) and top layer DO (~ 0.5 m below surface, $r = 0.42$), highlights the importance of vertical density gradients in determining the success of CyanoHAB taxa in polymictic lakes.

The CyanoHAB caused an increase in phytoplankton turbidity that substantially decreased the euphotic zone (Figure 3-3 and Figure 3-4). This is likely why a relatively shallow light penetration depth was selected as a strong predictor of high PerCyano (<65%) with our decision tree (Figure 3-9). However, the relatively deep euphotic zone prior to the cyanobacterial dominance likely helped spur the CyanoHAB in both years. In 2021, we observed the start of the CyanoHAB occurring during the period of the relatively deep euphotic zone, visually linking relatively deep light penetration with the onset of the CyanoHAB. This succession pattern of relatively clear water (i.e., clear water phase) followed by inedible phytoplankton (i.e., cyanobacteria) is consistent with that postulated for dimictic eutrophic lakes by the Plankton Ecology Group (PEG) model (Sommer et al., 2012). In contrast to the PEG model, cyanobacteria briefly lost dominance (PerCyano < 50%) of the phytoplankton community in late June 2021 due to a strong wind-driven mixing event that caused thermal destratification, showing that polymictic lakes may not always fit the PEG model for phytoplankton succession in eutrophic systems. Thus, the selection of a relatively shallow euphotic zone by the decision tree model is likely a result of the CyanoHAB instead of a driving factor.

Thermal stratification, even at the sub-daily to daily timescale, triggered a cascade of physicochemical changes to the water column. For example, thermal stratification inhibited the mechanical aeration of the bottom layer through mixing that subsequently caused near-bottom hypoxic/anoxic conditions, causing internal nutrient loading and in turn increased PerCyano (Figure 3-6 and Figure 3-7). Combined effects of slack wind turbulence and either solar radiation or air temperatures on hypolimnetic DO depletion were also reported by Shinohara et al. (2023). Multiple studies have shown near-bottom hypoxic and anoxic conditions (DO < 2 mg/L) cause metal reduction (e.g., Fe^{3+} into Fe^{2+} and Mn^{4+} to Mn^{2+}) through microbial anaerobic respiration (Beutel et al., 2008; Gobler et al., 2016; Norgbey et al., 2021) and soluble forms of P to be released from the sediment-water interface (SWI). This process could explain a visually distinct peak of Mn accompanied by the sharp increase of TP within bottom waters on June 16, 2021 (Figure 3-6). Based on the decision tree algorithm, bottom TP concentrations were one of the most important factors explaining PerCyano (Figure 3-9), indicating that internal P loading may be a dominant driver of CyanoHABs in Marion.

Increases in water-soluble and exchangeable Fe are favored by a decrease in ORP (Gotoh & Patrick, 1974; Miao et al., 2006); however, we did not observe a concurrent increase in Fe with Mn and TP during early June 2021 (Figure 3-6). Sulfide in sediment pore waters under anoxic conditions can affect iron precipitation because sulfide reacts rapidly with Fe^{2+}, forming insoluble iron and, thus, effectively removing the iron from the system (Molot et al., 2014). In contrast, Mn^{2+} is stable in the presence of sulfide and is often observed diffusing out of sulfide-rich zones (Nealson & Saffarini, 1994), which may be why we observed a response of Mn but not Fe during relatively low ORP conditions in 2021. Sediment metals and phosphorus release could be affected by a number of other mechanisms like organic matter decomposition, relatively high water temperatures, and changes in pH (Delfino & Lee, 1971; Miao et al., 2006), even under oxic/relatively high ORP conditions (Hupfer & Lewandowski, 2008).

Future studies on Marion Reservoir could determine if sulfur or other factors like relatively high bottom temperatures or pH are affecting metal and nutrient release from the sediments. Despite the relatively low variation in nutrient concentrations over the study period, wind-induced mixing, and resuspension of released phosphorus from sediment in the overlying water seemed to result in favorable conditions for CyanoHAB taxa in Marion Reservoir.

The higher rate of oxygen consumption at the bottom of the epilimnion was first observed in the summer of 2022 (between the last week of July and the first week of August; Figure 3-4). This phenomenon occurred when biological oxygen demand exceeded the flux of atmospheric oxygen to the epilimnion from wind-driven mixing (Kreling et al., 2017). Accumulation of phytoplankton near the thermocline due to high-density gradients can slow down their sinking, increasing the retention time and establishing a productive layer. This condition favors the heterotrophic decomposition of cyanobacterial biomass, leading to an increased decay of organic matter. As a consequence, the rates of oxygen consumption increase, which can ultimately result in hypoxic conditions (Mi et al., 2020; Nwosu et al., 2021). This may be why we observed hypoxic conditions near the bottom of the epilimnion 2 months after cyanobacteria became the dominant phytoplankton.

Historically, P has been considered a primary limiting nutrient controlling phytoplankton biomass in freshwater reservoirs (Hoyer & Jones, 1983; Jones & Knowlton, 1993). The TN:TP ratio has been shown to serve as an indicator of N- or P-nutrient limitation for phytoplankton (Downing et al., 2001; Liang et al., 2021), with cyanobacteria being favored over other taxa during periods of low TN:TP ratios (<30 by mass; Harris et al., 2014; Orihel & Rooney, 2012; Smith, 1983). In Marion, TN:TP ratios were substantially less than 30 (TN:TP <5 by mass) throughout June-September in both years. These relatively low TN:TP ratios were driven by increases in P

(Orihel & Rooney, 2012), as exemplified in bottom samples collected during June 2021 (Figure 3-6), and a negative correlation between bottom TN:TP ratios and PerCyano (Figure 3-8). Dzialowski et al. (2005 and 2011) reported that in the Kansas reservoirs with TN:TP ratios between 9-29, co-limitation of phosphorus and nitrogen impacted phytoplankton production. Given that TN:TP ratios were generally <9 in Marion Reservoir indicates that N-limitation of the phytoplankton community may be present; however, we did not sample for heterocystous nor dissolved nutrients and thus cannot clearly identify if N limits phytoplankton biomass in Marion. Additionally, the TN:TP should be interpreted with caution since ratios only reflect the potential for nutrient availability, and actual limitation can be assessed by the concentrations of available dissolved inorganic nitrogen and phosphorus (Dzialowski et al., 2011).

To further investigate the impact of biotic and abiotic factors that shape cyanobacterial blooms, a broader range of variables such as basin hydrology, biological components (e.g., zooplankton community structure), and reservoir morphology could be evaluated for their relative importance in determining CyanoHABs in turbid, polymictic reservoirs. Considering the widespread occurrence of CyanoHABs in discontinuous polymictic lakes and reservoirs worldwide (Gray et al., 2019; Loftin et al., 2016), the research presented here extends beyond Marion Reservoir and the results will be helpful to scientists and water managers' working strategies for other water bodies to deal with CyanoHABs. Additionally, our work shows a clear link between meteorological factors, thermal stratification, and CyanoHABs in polymictic, hypereutrophic reservoirs. Given that temperatures are expected to increase between 2-5 °C by the end of this century and strong wind events (WS > 7 m/s) may be declining in the central Great Plains (Kunkel et al., 2022; Tavakol et al., 2020), our results may be helpful to improve the representation of dynamic processes of understudied polymictic reservoirs and pave the way for prospective process-based modeling studies that aim to capture the complexity of processes that affect future CyanoHABs emergence in response to climate extreme events.

Chapter 4: : Assessing the Impact of Input Data on Vertical 1D Model for Predicting Lake Thermodynamic Patterns: A Case Study of Marion Reservoir (Kansas, U.S.)

Hosseini, A., Roundy, J.K., Ladwig, R., Mesman, J., and Harris, T.D., 2023. Assessing the impact of input data on a vertical 1D model for predicting lake thermodynamic patterns: A case study of Marion reservoir (Kansas, U.S.). Lake and Reservoir Management (under preparation).

4.1 Abstract

The rapid expansion of anthropogenic activities has profoundly and pervasively impacted diverse biosphere processes across a broad spectrum of scales. Notably, inland freshwater systems have experienced extensive alterations, positioning them among the ecosystems most profoundly affected by human-induced changes. Despite the growing number of reservoirs worldwide to meet escalating water demands and the inherent variations in reservoir processes, there remains a notable underrepresentation of reservoir-centric studies. Additionally, the lack of required hydro-climatological factors in the data-scarce area has created a gap in quantifying lacustrine dynamics, especially lake thermal structure and mixing regimes over time. A combination of the community Noah-MP land surface model (LSM) stream flow predictions and mechanistic General Lake Model (GLM) can therefore provide an important method for simulating future thermal conditions in ungauged or data-limited catchments. Utilizing a combination of land surface model and lake model requires calibration and validation of the inputs and the lake model involved as well as a comprehensive sensitivity analysis to ensure the accuracy of the observed and simulated water temperature. To test this modeling framework, it is employed in the case of Marion Reservoir, a multi-purpose impoundment situated in central Kansas. Marion Reservoir serves a variety of functions including flood control, water supply, and recreation. Notably, Marion Reservoir is renowned as a hypereutrophic discontinuous polymictic waterbody, characterized by recurring algal blooms that have persisted for over a decade. The lake model was able to reproduce the water temperature dynamics when forced with either measured field data or modeled inputs (NLDAS-2 and Noah-MP) at Marion Reservoir. While the Noah-MP runoff simulations successfully captured the general trend of inflow, the magnitude of runoff during the late spring and early summer period was found to be considerably lower when compared to the measurements obtained from gauges. This study provides a first step to coupling the GLM lake model into Noah-MP to improve the representation of inland freshwater ecosystems in land surface models.

Keywords: Lake thermal regime, Reanalysis climate data, GLM, Noah-MP, Streamflow

4.2 Introduction

Inland freshwater bodies including lakes and reservoirs are recognized as important sentinels of climate change, integrating surrounding catchment areas and atmospheric climate change drivers (Adrian et al., 2009). Climate change and the persistent rise in global air temperatures have profound impacts on aquatic ecosystems, resulting in earlier, extended, and more pronounced thermal stratification (N. M. Hayes et al., 2017; Woolway & Merchant, 2019).

Due to its ecological importance, changes in stratification phenology (i.e., the timing of stratification onset and break-up) play a fundamental role in numerous physical, chemical, biological, and ecological lake processes including key processes like nutrient cycling and light availability, sedimentation, and depletion of hypolimnetic dissolved oxygen (Jankowski et al., 2006; Piccioni et al., 2021; K. Song et al., 2013; Wilhelm & Adrian, 2007; Winder & Sommer, 2012). Associated increases in air temperature will not only result in more profound lake stability gradients but also in generally higher surface water temperatures (Hondzo & Stefan, 1993; Pilla et al., 2018). At elevated temperatures, cyanobacteria can often outcompete eukaryotic algae, creating a significant hurdle in maintaining the crucial ecological balance and sustainable use of water resources (Paerl, 2014; Wagner & Erickson, 2017).

Reservoirs and lakes are often perceived as interchangeable entities due to their shared characteristics and functions. While most natural lakes, such as those formed by glaciers, have existed for thousands of years, reservoirs, in contrast, are predominantly young, with an average lifespan of less than 50 years (Havel et al., 2005). Historically, reservoirs have been grouped together with natural lakes in conceptual models of climate change impacts, failing to recognize their unique characteristics and processes (Hutchinson, 1967; Williamson et al., 2009). For instance, reservoirs often exhibit substantial watershed-to-lake area ratios in comparison to natural lakes, rendering them more prone to experiencing elevated nutrient and sediment loads. In addition, the extended hydraulic residence time in reservoirs contributes to a prolonged nutrient retention period and creates favorable conditions for the proliferation of cyanobacteria blooms.

With the escalating global construction of reservoirs and dams in response to growing water demands (Zarfl et al., 2015), it is crucial to enhance our understanding of both lakes and reservoirs, particularly in relation to climate change and eutrophication. However, there is a notable scarcity of studies that have quantified these impacts specifically on reservoirs when compared to natural lakes.

Midwestern reservoirs, which represent the primary lentic habitat in the central US according to Thornton (1990), possess the potential to act as valuable climate analogs for studying and predicting the effects of climate change on upcoming aquatic ecosystems. Due to fertile plains soils and extensive agriculture, most reservoirs in the Corn Belt and Northern Great Plains, are classified as mesotrophic to eutrophic.

Numerical process-based lake models serve as powerful tools for obtaining a comprehensive understanding of aquatic processes, unraveling causal factors, and estimating future trajectories of the system in response to climate change (Ladwig et al., 2018; Mesman et al., 2020). For lakes and reservoirs in particular, one-dimensional (1-D) models that resolve vertical profiles of temperature and density have become indispensable tools for studying and managing these water bodies. These models are widely utilized due to their computational efficiency and minimal calibration requirements, providing valuable insights into aquatic systems. Moreover, lake managers and reservoir operators often favor the simplicity and straightforward application of 1-D models over higher dimensional (Kerimoglu & Rinke, 2013; Weber et al., 2017).

While the need for accurate meteorological forcing in simulating watershed hydrological cycles is well established, many lakes and reservoirs in the U.S. and other parts of the world may not have the resources to continuously monitor the weather data. In addition, the limited availability of direct streamflow measurements in areas with spare monitoring systems remains a significant challenge. Even when streamflow records exist for estimating reservoir inflow rates, they tend to focus primarily on main streams, while data on discharge from tributaries are rare (Song et al., 2022). Currently, the primary challenge in the process of parameterizing lakes and reservoirs within climate models is to ensure that the models' behavior remains consistent and precise, taking into account the broad spectrum of morphological attributes and the significant fluctuations in meteorological forcing (Almeida et al., 2022). While the incorporation of inflows and outflows may crucially improve the quality of model predictions, the uncertainties and inadequate forcing data can restrain the broader application of process-based models.

In the absence of reliable gauge measurements, model-based runoff estimations offer a viable solution, leveraging advanced Land Surface Model (LSM) models like Noah’s Multiparameterization (Noah-MP) (Niu et al., 2011). The inclusion of vegetation dynamics within the Noah-MP model improves its accuracy when estimating surface fluxes, temperature, and key hydrological variables, such as soil moisture, snow water equivalent, and runoff (Hosseini et al., 2022).

The NASA North American Land Data Assimilation System Phase Two (NLDAS-2) presents a potential weather data source for 1-D modeling applications. This dataset is particularly valuable due to its assimilation of climate observations from various sources, resulting in high-resolution, spatially continuous, and comprehensive climate-forcing data. NLDAS-2 has gained recognition as a reliable and robust dataset, making it a valuable resource for conducting hydrological modeling at the watershed scale. The NLDAS-2 dataset is utilized as a source of atmospheric forcing data to drive the Noah-MP model.

During the last decades, one-dimensional hydrodynamic models (e.g., General Lake Model, GLM, Hipsey et al., 2019) have been applied to the vast diversity of lakes and reservoirs around the globe to simulate water body conditions under climate change. The integration of the GLM model into widely used land surface models like Noah-MP holds growing significance for developing a holistic forecasting model. Such a model holds the potential to provide solutions for future challenges to simulate water body conditions (e.g., water level, thermal structure) under environmental alterations (e.g., climatic, land use, and agricultural policies; Bruce et al., 2018). The primary objective of this study is to lay the foundation for achieving this goal by proposing an initial step forward. We conducted a comparative analysis to assess GLM's performance in simulating the hydrodynamic and thermal behavior of a hypereutrophic, intermittently mixed reservoir. Our study included two separate model runs. The first run involved implementing the GLM model utilizing in situ meteorological forcing data and inflow measurements sourced from the U.S. Army Corps of Engineers (In-si. The second run employed readily accessible and comprehensive NLDAS-2 datasets for forcing data, in conjunction with Noah-MP's runoff predictions. At this stage, only a one-way coupling of the models was carried out so that the runoff predictions obtained by the Noah-MP model served as input data for the GLM simulations.

This linkage provides a valuable opportunity to capture a more realistic depiction of reservoir responses to climate, even in the face of challenges such as limited observations and spatial heterogeneity, and empowers the adaptation of appropriate future management practices.

4.3 Materials and Methods

4.3.1 Study Site

Marion Reservoir, situated in Marion County, Kansas, was constructed in 1968 by the Tulsa District, U.S. Army Corps of Engineers (USACE). With a water area of 25.13 km^2, it is a polymictic reservoir with an average depth of 3.4 meters (reaching a maximum depth of 9.0 m, as reported by KDHE in 2002, Figure 4-1). The North Cottonwood River and its tributaries account for 82% of the watershed drainage, while the French Creek watershed contributes to the remaining 18% (Barnes & Devlin, 2008). Serving multiple purposes such as flood control, water supply, and recreation, the reservoir plays a crucial role as a primary source of drinking water for the local communities in Marion County and its surroundings (Mosher, 2000).

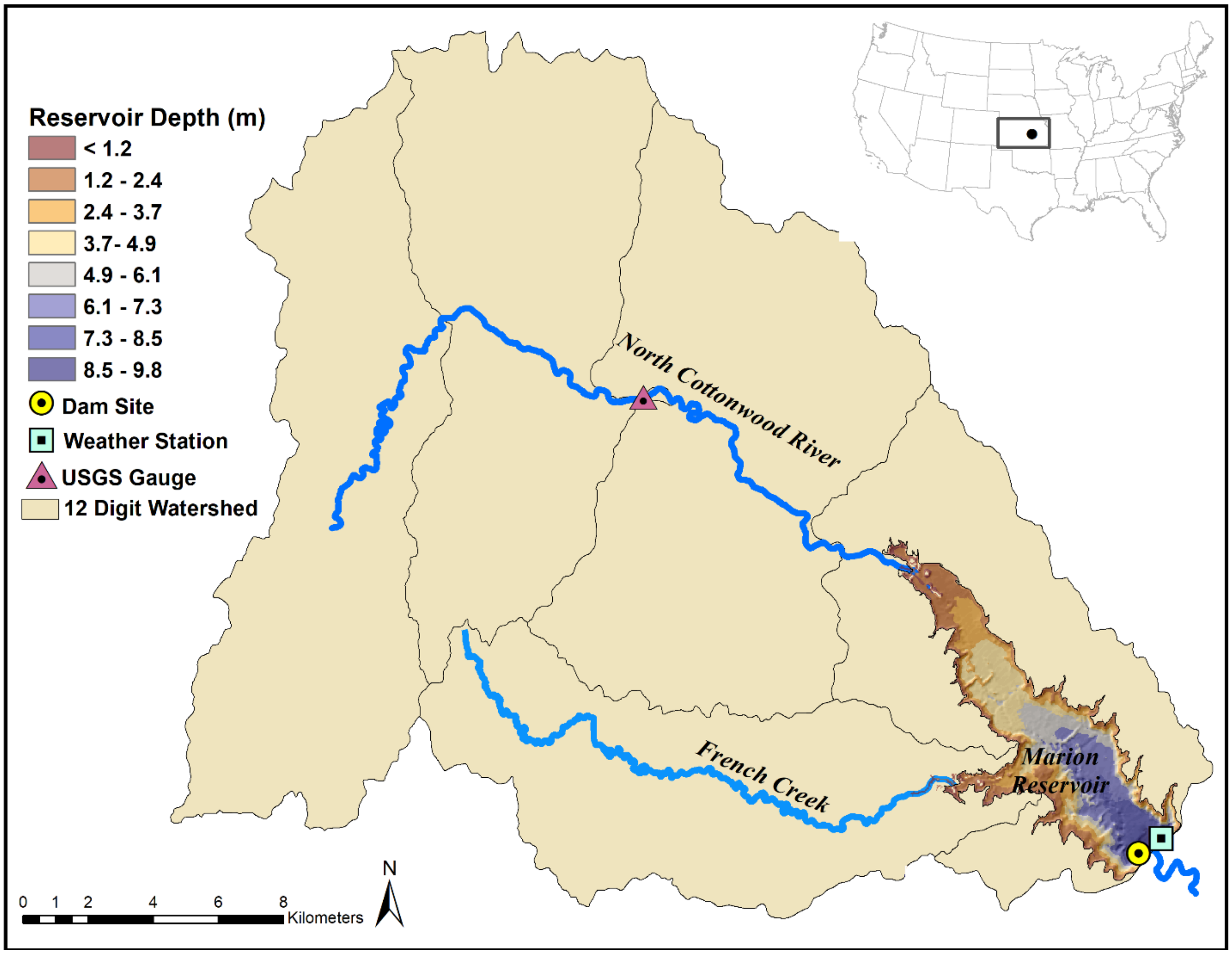

Figure 4-1: *Location of Marion reservoir in Kansas showing: two major inlet streams along with 2-digit hydrologic unit code Location of Marion reservoir in Kansas showing: two major inlet streams (i.e., North Cottonwood River and French Creek along with 2-digit hydrologic unit code (HUC) basins comprising the Marion Reservoir watershed, a bathymetric map, location of the monitoring buoy (yellow dot), and weather station operated by U.S. Army Corps of Engineers (blue square).*

4.3.2 Atmospheric Forcing and Input Data

Meteorological measurements, including air temperature (°C), wind speed (m/s), and precipitation (m/hr), were obtained from the U.S. Army Corps of Engineers (USACE) station situated near the dam of the reservoir (Figure 4-1). Additionally, inflow from the Cottonwood River inlet and outflow and water level records of the dam were collected from USACE. The meteorological and all input data were available at an hourly resolution. Bathymetric data for the reservoir was collected in 2008 by the Kansas Biological Survey (KBS 2010, Figure 4-1).

The NLDAS-2 data set includes precipitation (mm/hr), downward shortwave and longwave radiation (W/m^2), near-surface air temperature (°K), wind (m/s), humidity (kg/kg), and surface pressure (hPa). The NLDAS-2 data set utilizes a combination of ground-based rain gauges, radar, satellite observations, and model-generated precipitation, based on the NCEP North American Regional Reanalysis (NARR; Mesinger et al., 2006) over the U.S. to produce a high-resolution (1-hourly 12.5-km) gridded precipitation and surface meteorological data set. The NLDAS-2 data were extracted for the grid that contains the reservoir for the period 1 January 2021 to 31 December 2022 (Figure 4-2).

Observed streamflow from the United States Geological Survey (USGS) gauge at *Cottonwood River near Durham, KS* (07179785, https://waterdata.usgs.gov) was used for bias correction of simulated streamflow.

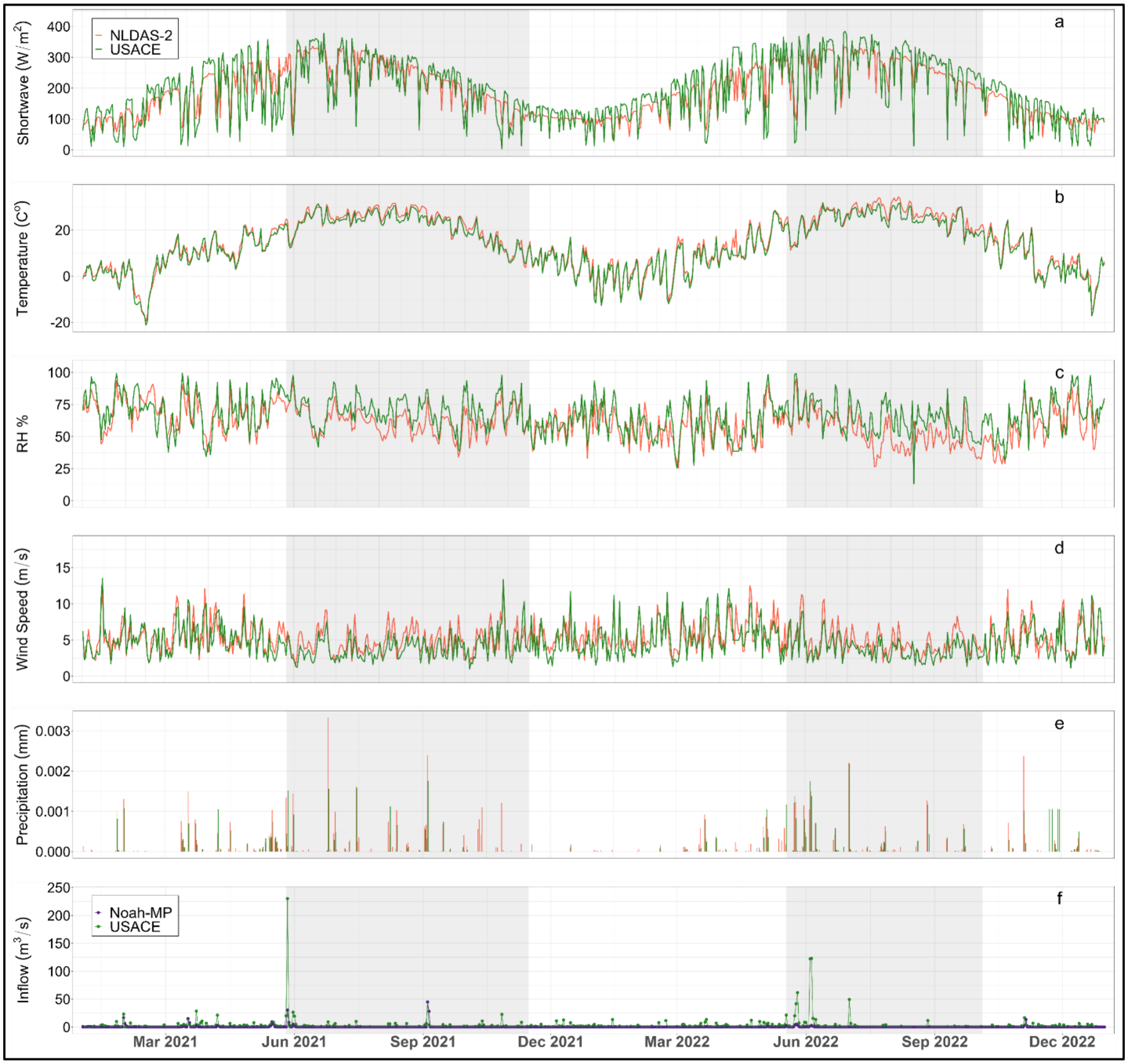

Figure 4-2:

Temporal disaggregation of meteorological forcing and inflow data for Marion Reservoir (2021-2022). USACE measurements vs NLDAS-2 (a) shortwave solar radiation, (b) air temperature, (c) relative humidity, (d) wind speed, (e) precipitation, and (f) inflow hydrograph presenting USACE measurements at Cottonwood inlet vs biased corrected Noah-MP simulation from both Cottonwood and French Creek inputs. Gray-shaded areas denote two sampling campaigns (i.e., 27 May -15 November 2021 and 15 May - 5 October 2022).

4.3.3 In situ Lake Temperature Data

In the spring of 2021, a monitoring buoy was deployed at Marion Reservoir near the deepest point in the lake (dam buoy, ~8 m, Figure 4-1). This monitoring buoy was designed to collect water temperature measurements throughout two distinct sampling campaigns, May 26 - November 15, 2021, and May 18 - October 5, 2022, using HOBO loggers (PME, Vista, CA, USA; Onset, Bourne, MA, USA). More detailed descriptions of the monitoring site and sampling methodology can be found in Hosseini et al. 2023 (under review).

4.3.4 General Lake Model (GLM)

GLM is a one-dimensional open-source hydrodynamic model designed to simulate a wide range of enclosed aquatic ecosystems, including lakes, reservoirs, and wetlands. The model employs a flexible Lagrangian structure which adjusts the thickness and volume of layers with consistent properties during each step of the simulation (Bueche et al., 2017; Read et al., 2014; L. A. Winslow et al., 2017). For mixing, GLM applies an integral energy approach in which the mixing depth is determined by the amount of available external kinetic energy. Transport below the mixed layer depth is parameterized through an eddy diffusion coefficient approach. The mathematical equations and hydrodynamics closures that govern GLM are detailed in the work of Hipsey et al. (2014, 2019). The model, along with its comprehensive documentation that encompasses detailed version update descriptions, can be found at http://aed.see.uwa.edu.au/research/models/GLM/Pages/documentation.html.

Required meteorological forcing data to run GLM (v3.3.0) include wind speed, air temperature, relative humidity, precipitation, snow, shortwave, and longwave radiation. Incoming longwave solar radiation data from NLDAS-2 and wind direction measurements obtained from

USACE were utilized in both scenarios. Due to the unavailability of snowfall records for the study site, it was assumed that there was no snow present during the analysis period.

4.3.5 Noah-MP

The community Noah land surface model with multi-parameterization options (Noah-MP; Niu et al., 2011; Yang et al., 2011) is a powerful tool for the simulation of energy, water, and carbon fluxes exchanging between the land surface and the atmosphere. Improved representation of terrestrial hydrometeorological and eco-hydrological processes in Noah-MP resulted in the enhanced simulation of surface runoff across various special and temporal scales (Ma et al., 2017; Niu et al., 2011). We apply version v4.0.1 of Noah-MP with dynamic vegetation to compute the leaf area index (LAI) and annual maximum FVEG from the monthly climatological gridded data. The soil layer configuration in the models comprises four layers with varying thicknesses from the surface to the bottom, resulting in a total soil depth of 2.0 meters. The thicknesses of these layers are as follows: 0.1 meters, 0.3 meters, 0.6 meters, and 1 meter, respectively. In the soil moisture simulation, the upper boundary condition is determined by the infiltration rate, which is calculated as the difference between precipitation and surface runoff. The parameterization of surface runoff follows a straightforward TOPMODEL-based runoff scheme (Niu et al., 2005), where the residual runoff is used to estimate the infiltration rate. The model run spans the entire state of Kansas (37°–40°N, 102°– 95°W) at a spatial resolution of 1/8° grid (~12.5 km) at an hourly temporal resolution for the period 1 January 2016 to 31 December 2022. Detailed model descriptions and other parameters can be found in Hosseini et al., 2022.

4.3.6 ***Simulated Runoff Routing and Bias Correction***

To generate streamflow input for the Marion Reservoir, the gridded runoff and baseflow obtained from the Noah-MP model were combined with a hydrologic routing model. The routing model simulates the movement of water through the natural stream channels, taking into account factors such as topography and stream channel characteristics. The routing model employs the HydroSHEDS topography dataset, which has a resolution of 30 arcseconds (approximately 1km), as well as a velocity parameterization that accounts for slope adjustments based on Gong et al. (2009). While this routing algorithm only solves continuity, it offers a computationally efficient approach that has been successfully applied in various hydrologic monitoring and forecasting applications, as demonstrated by Sheffield et al. (2013) and Yuan et al. (2015).

Even though the simulated daily discharge from Noah-MP provides good estimates of streamflow, it is expected that the model will still have systematic biases due to the underestimation of runoff as mentioned that can be corrected statistically. To do this, we utilize the USGS stream gage (07179785) on the Cottonwood River, to create a normalized correction factor based on the percentile and season of the flow. This correction factor is created by calculating the difference between the USGS stream gauge and the model for percentile flows and months of the year. To capture the variability of streamflow, streamflow percentiles were computed for each month, ranging from the p_0 (minimum daily streamflow) to the p_{100} (maximum daily streamflow), with a step size of 5%. The monthly percentiles are calculated by pooling all daily flows from within the month from 2016 to 2022, which aligns with the availability of the USGS data. The normalized correction factor is then calculated as the difference between the percentile flow from the USGS gauge and the model at all percentiles and months. This correction factor is then normalized by dividing by the drainage area at the gage location. This creates a two-dimensional space (month and percentile) that can be used to calculate a correction factor for model streamflow for a different location by knowing the date, percentile flow from the model, and basin area. This correction factor was then applied to modeled streamflow at the two inputs of

Marion reservoir, Cottonwood and French Creek. After the daily model, streamflow has been corrected, it is then temporally downscaled to hourly streamflow by randomly selecting observed hourly time series based on season and percentile flow. The bias correction approach implemented in this study demonstrated a close resemblance to the observed values. This improvement is evident in Spearman's coefficient range, which ranges from 0.26 to 0.71 (Figure 4-3).

The observed hourly time series used to create the hourly downscaling was based on the hourly reported inputs from the US Army Corps of Engineers weather station. While this method of temporarily downscaling the streamflow produces reasonable realizations of hourly flow data that match the daily estimates, it is not expected that these hourly estimates will match observations due to the random selection of partitioning of hourly flow. This corrected streamflow at an hourly time step provides the best estimate of hourly streamflow from the model and was used as one of the inflows in the GLM model.

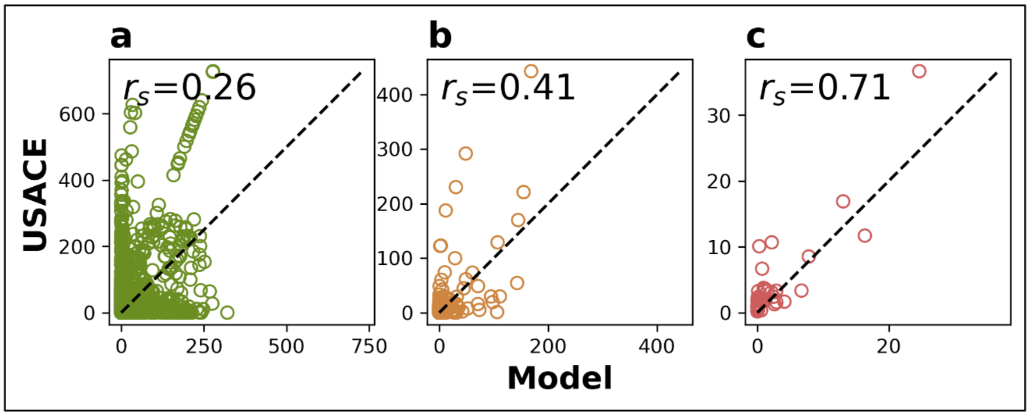

Figure 4-3:
Comparison between biased corrected simulated routed streamflow and USACE measurements at (a) hourly, (b) daily, and (c) monthly time scales for the period of 2019–2022 including Spearman's rank correlation coefficient (r_s) scores.

4.3.7 Calibration and Validation

Both GLM runs with different forcing inputs were calibrated separately with high-frequency water temperature data collected throughout 2021–2022 using manual adjustments and auto-calibrating scripts. Data from a longer measurement period in 2021 were employed for calibration, while data from 2022 were reserved for validation.

In the first step, we manually calibrated the parameters "*rain_factor*", "*inflow_factor*", and "*outflow_factor*" to improve the water balance fit and to enhance the agreement between the simulated and measured water levels. To identify the key parameters that govern the lake mixing process and shape model predictions of water temperature, a set of parameters was selected based on our understanding of the uncertainties associated with each parameter for Marion Reservoir (Hosseini et al. under review), as well as the relevant boundaries delineated by previous studies (Winslow et al. 2017). A set of four calibration parameters was chosen to refine the model's accuracy. These parameters include the light extinction coefficient, which describes the depth of light penetration, along with scaling factors for wind speed, shortwave radiation, and longwave radiation.

To minimize the root-mean-square error (RMSE) of water temperature, we employed the Covariance Matrix Adaption Evolution Strategy (CMA-ES) algorithm, a derivative-free and evolutionary optimization technique (Hansen, 2006; Ladwig et al., 2018, 2021). Within the calibration process, 1000 iterations were conducted. A summary of the GLM parameters considered in the calibration process, with descriptions, default values, and final values used for the simulation in this study, is given in Table *4-1*.

Table 4-1:
Description, symbols, initial values, value ranges, and model value (the calibrated values that are used to run each model configuration) of General Lake Model (GLM) parameters used in the thermal calibration process.

Parameter	**Symbol**	**Description**	**Value Range**	**Model Value [In-situ, LSM]**
rain_factor*	$\boldsymbol{f_R}$	Scaling factor to adjust the rainfall	[0.1,1]	0.8
inflow_factor*	$\boldsymbol{f_{infI}}$	Scaling factor that can be applied to adjust the provided input data	[0.5,10]	3.39
outflow_factor *	$\boldsymbol{f_{outf}}$	Scaling factor that can be applied to adjust the provided input data	[0.5,2]	1.0
sw_factor	$\boldsymbol{f_{SW}}$	Scaling factor to adjust the shortwave radiation data	[1,0.25,2]	0.46, 0.25
lw_factor	$\boldsymbol{f_{LW}}$	Scaling factor to adjust the longwave (or cloud)	[0.5,0.25,2]	1.35, 1.34
wind_factor	$\boldsymbol{f_u}$	Scaling factor to adjust the windspeed	[1,0.7,1.3]	1.30, 0.94
Kw	$\boldsymbol{K_w}$	Light extinction coefficient (1/m)	[0.7,0.1,4]	0.88, 1.13

Note. The value ranges include initial value, upper and lower limits. Moreover, the parameters marked with (*) undergo manual calibration.

The performance of the water temperature simulation was evaluated using the widely recognized root mean square error (RMSE) metric, which is commonly employed as a benchmark for evaluating model fit in lake modeling studies (Bueche et al., 2017, 2020; Frassl et al., 2018; Luo et al., 2018; Willmott & Matsuura, 2005).

$$RMSE = \sqrt{\sum_{i=1}^{N} \frac{(S_i - O_i)^2}{N}}$$

where N is the number of samples, S_i and O_i represent simulated and observed values respectively. All analyses were done with the software R (R Core Team, 2018).

4.4 Results

This study adopts a two-step evaluation approach, examining the impact of various forcing data on both lake water level and thermal simulations, comparing them to the field measurements.

4.4.1 Reservoir Water Level

Throughout the entire simulation period, the results of the In-situ model consistently demonstrated an overestimation of the water level, displaying a significant deviation in comparison to the observed values (overall RMSE=1.42 m). The disparity was particularly prominent for low water levels, where the deviation reached as high as 2 meters (Figure 4-4a).

In contrast, the results of the LSM simulation revealed a relatively strong agreement with the observed water level (overall RMSE=0.80), specifically during the summer of 2021. Although, starting from September 2021, the model consistently began to overestimate the water level by approximately 0.5 m, and this discrepancy persisted throughout the remainder of the year. In 2022, the water level was initially overestimated by approximately 0.5 m until June 2022. However, from June onward, there was a shift, and the model started underestimating the water level by around 1 m. This underestimation persisted until the end of the year (Figure 4-4b). Even though the range was not correct, the model captures the seasonal variability through the seasons, depicting the gradual decline in water levels during summer and autumn, as well as the occurrence of low flows in winter.

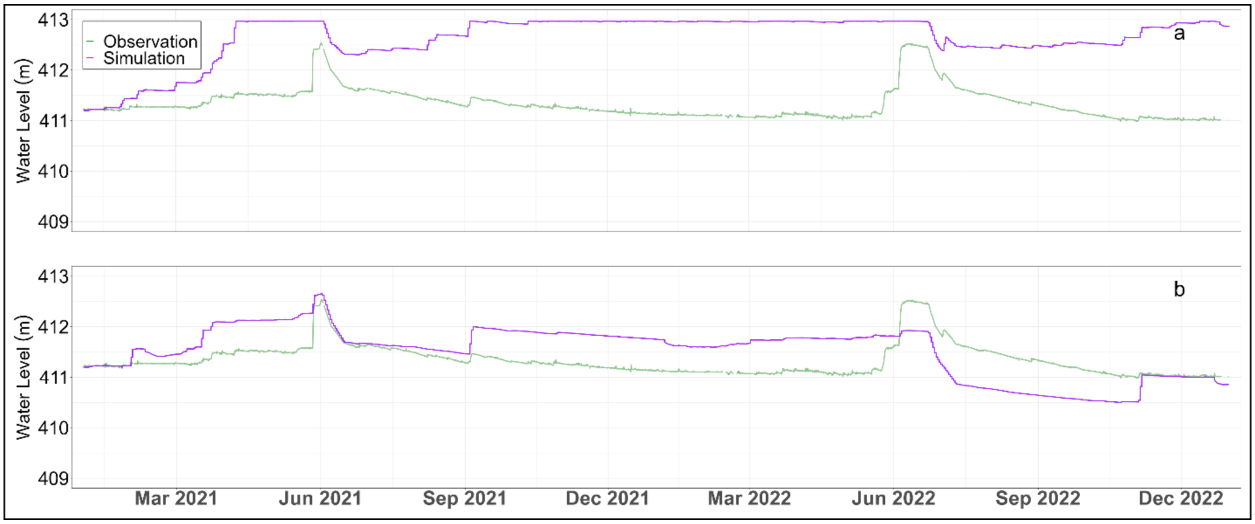

Figure 4-4: *Comparison of water level data between observed and GLM simulation Comparison of water level data between observed (green) and GLM simulated (purple) over the period of 2021-2022 at Marion Reservoir. The simulations were based on two different sets of forcing datasets: (a) In-situ, and (b) LSM models.*

The In-situ model consistently tends to overestimate lake water levels, particularly evident during the winter and early spring months (up until April), accompanied by heightened uncertainty. After this period, the disparities diminish slightly. In contrast, the LSM model consistently offers closely aligned predictions for lake water levels throughout both years, up until May. As summer commences, the dissonance between observed and simulated water levels begins to escalate, ultimately reaching disparities of up to 1 m during the fall (Figure 4-5).

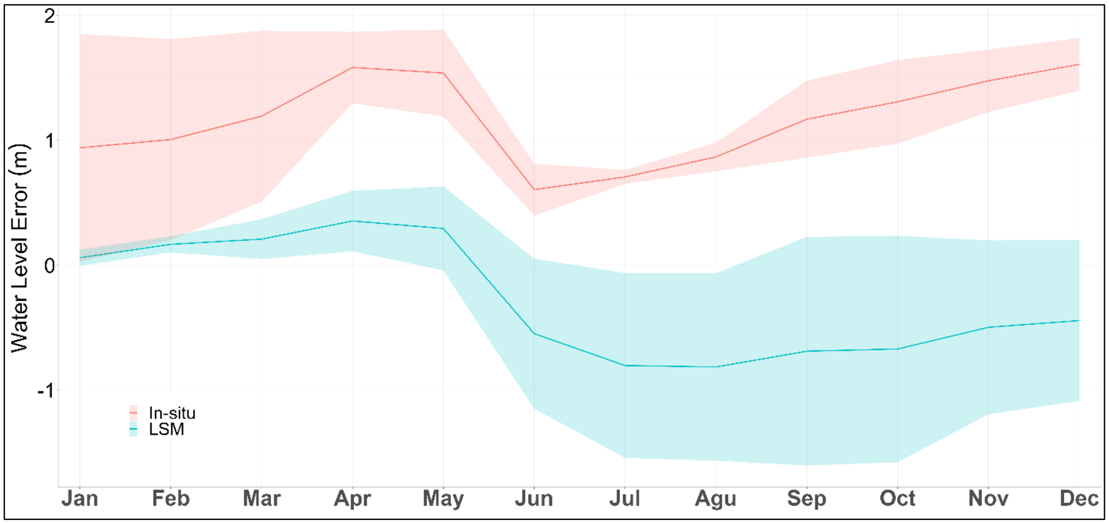

Figure 4-5:
Monthly average values of the hourly difference between observed and simulated lake water levels using In-situ and LSM models in Marion Reservoir during 2021-2022. The shaded area around lines indicates standard error.

4.4.2 Water Temperature Dynamics

Both combinations of meteorological forcing and inflow data could reproduce the lake's thermal dynamics (e.g., short-stratified, and isothermal conditions) well throughout the two-year study period from 2021 to 2022 (Figure 4-6). Remarkably the deviations between the simulated and measured values during the validation period were smaller for the second scenario, with an RMSE of 0.88 °C, compared to the RMSE of 1.1 °C observed in the first scenario (Table *4-2*).

Although the same initial and boundary conditions are applied to both runs, there are still some variations between the two scenarios' results, and they are also different from the field data to a certain extent. Positive and negative deviations of differences between simulated and observed temperature are almost equal during the calibration period for both scenarios, resulting in RMSE values of 1.15 and 1.21 °C respectively (Table *4-2*).

Table 4-2

Model results or goodness-of-fit, measured by Root Mean Square Error (RMSE)

Model	**Calibration**	**Validation**	**Total RMSE before Calibration**	**Total RMSE after Calibration**
In-situ	1.21	1.1	7.09	1.16
LSM	1.15	1.0	2.82	1.08

Note. The RMSE is calculated for calibration, validation, uncalibrated, and calibrated entire model runs for water temperature (°C) in Marion Reservoir using two different hourly forcing datasets.

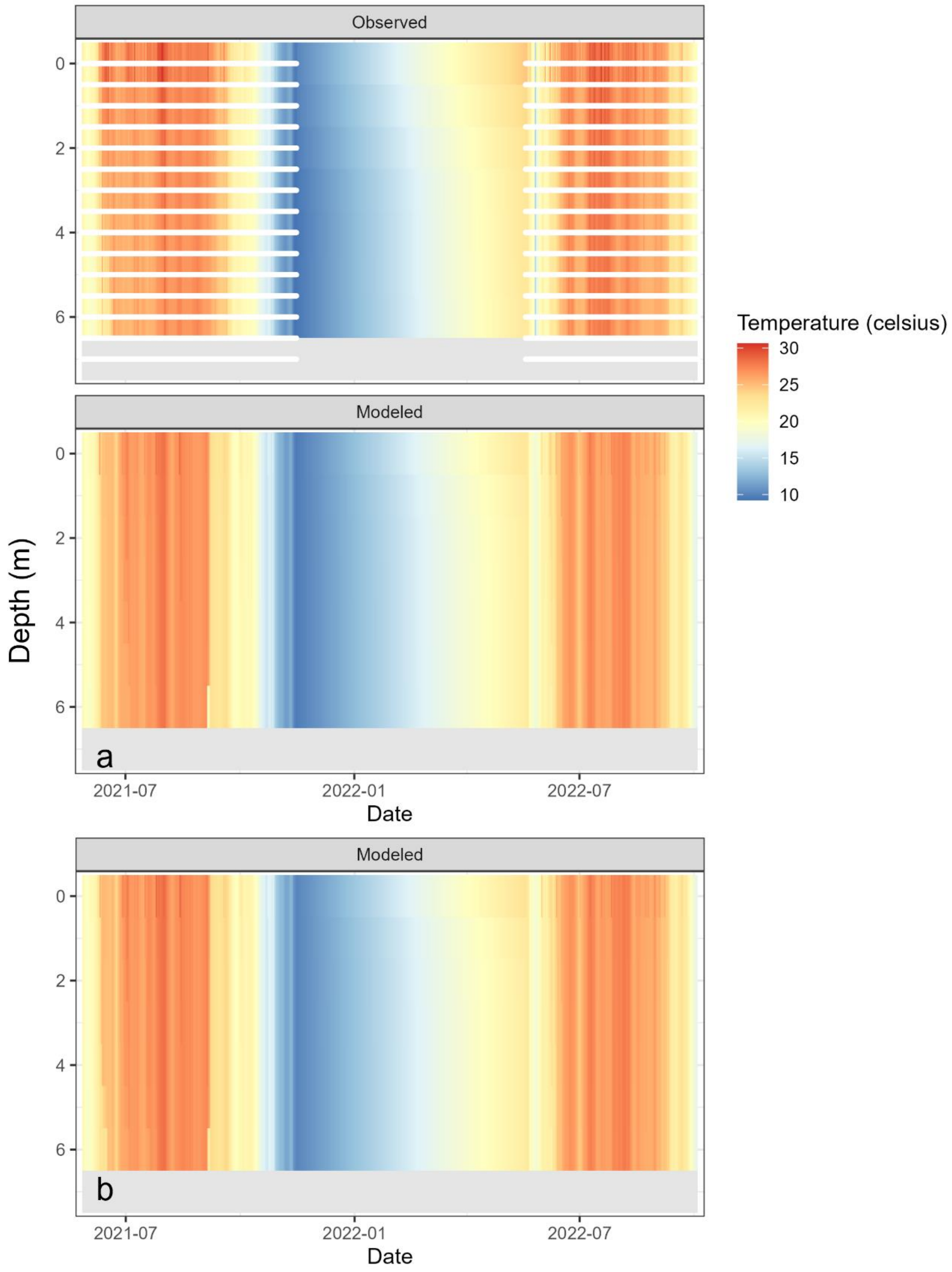

Figure 4-6:
The temperature profiles of Marion Reservoir between 2021-2022, with the top panel displaying the contour plot of measured data, (a) In-situ, and (b) LSM models. White dots on the observed

plot indicate the precise locations (time, date, and depth) where continuous field-recorded water temperatures were available.

Overall, a comparative analysis of the simulated thermal dynamics using the two model configurations indicates that the LSM model provides a relatively more accurate depiction of the extent of short-term stratification across the water column compared to the In-situ model (Figure 4-6). The quantitative evaluation, measured through total RMSE, demonstrates that the LSM model achieves a lower RMSE value of 1.08 °C, in contrast to the slightly higher RMSE of 1.16 °C observed in the In-situ model.

The distinction between simulated and measured water temperatures throughout the water column becomes further apparent when analyzing the average seasonal evolution of hourly errors from both models. As illustrated in Figure 4-7, significant disparities are evident in water temperatures between simulations and measurements across the epilimnion (0.5 m), metalimnion (3 m), and hypolimnion (7 m) during the months of late May and June. Importantly, this time frame aligns with the occurrence of Cyanobacterial Harmful Algal Blooms (CyanoHabs) within the lake.

.

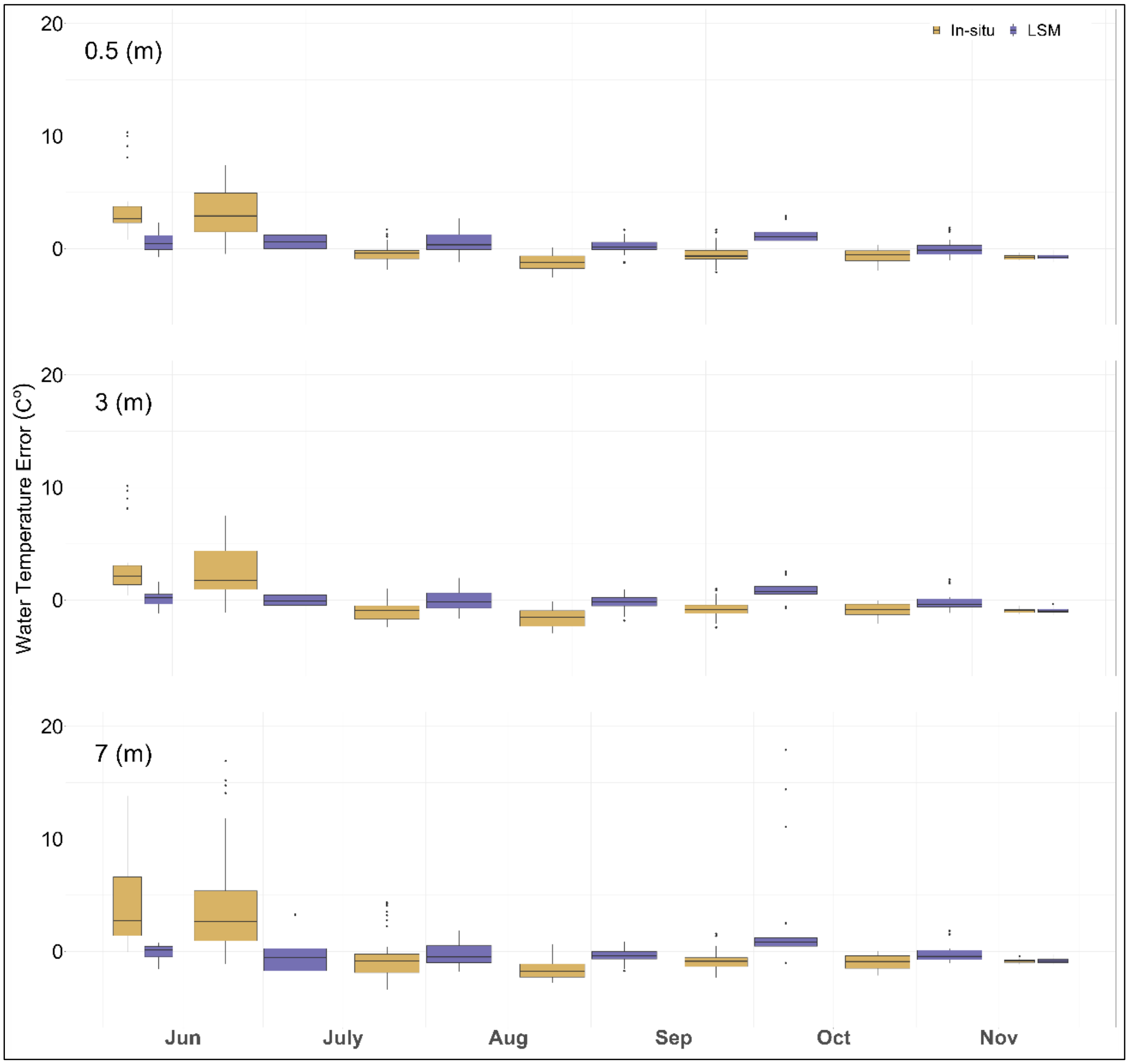

Figure 4-7:
The average seasonal variation of the hourly difference between observed and simulated lake water temperature using In-situ and LSM models at 0.5, 3, and 7 m depth) in Marion Reservoir during 2021-2022.

4.5 Discussion

We base our analysis on high-frequency temperature profile observations and simulations. Changes in the thermal dynamics of shallow reservoirs can have significant consequences for various aspects of the aquatic environment. They can affect water transparency, as well as the dispersion and movement of oxygen and nutrients, ultimately influencing essential biological processes. The analysis of temperature dynamics, considering NLDAS-2 data alongside simulated Noah-MP inflow as input data, in comparison to measured forcing revealed that GLM was able to replicate the complex patterns and fluctuations in water temperatures, even in the absence of essential meteorological and stream flow field measurements. The comparison between the calibrated and validated years revealed only minor discrepancies, indicating a high level of model confidence and the feasibility of the LSM model for shallow reservoirs like Marion. While the RMSE criteria indicated a generally strong agreement between the simulated and observed water temperatures throughout the calibration and validation periods, the model displayed slight inconsistencies in simulating water levels and tended to underestimate surface layer water temperatures. Especially during the onset of CyanoHABs, an in-depth examination of the GLM model's performance highlights its challenges in accurately capturing lake water temperature dynamics. These limitations may be attributed to deficiencies in the energy budget representation within The General Lake Model (GLM) for polymictic shallow reservoirs, which consequently impacts the model's capability to effectively simulate variables, including temperature gradients, mixing patterns, and light penetration.

Alterations in the water level of a lake have the potential to cause significant effects on hydrodynamic processes, which encompass various aspects such as the depth of the thermocline, the stability and duration of stratification, and even the overall quality of the lake water itself (Robertson et al., 2018). The deviations between observations and simulations for both models indicated that at several times during the simulation, important inflows and/or outflows were missed. In the absence of inflow and outflow records, reservoir water level records can serve as a valuable alternative for estimating both inflow and outflow dynamics through careful analysis based on expert knowledge (Song et al., 2022). Therefore, enhancing the estimation of water level through the utilization of the GLM model, with NLDAS-2 forcing data and simulated Noah-MP inflow, holds immense potential for accurately quantifying reservoir water balance.

The inclusion of a runoff scheme in the Noah-MP model, which considers the interaction between the unconfined water layer and upper soil significantly improves the accuracy of stream flow calculations (Cai et al., 2014; He et al., 2023). Furthermore, the integration of the dynamic Leaf Area Index (LAI) and Vegetation fraction (FVEG) within the Noah-MP (v.4.0.1) model significantly enhances its ability to provide more skillful estimates of stream flow (Hosseini et al., 2022; Kumar et al., 2019).

Significant hourly bias was noted in the routed streamflow results derived from the Noah-MP simulation when compared to USACE gauge measurements, with a pronounced emphasis during the early to mid-June timeframe for both years. However, through the application of the statistical bias correction method described here, it becomes possible to effectively mitigate systematic bias and substantially improve the agreement between simulated runoff from Noah-MP and gauge measurements over an hourly to monthly time scale.

The obtained result validates the effectiveness of utilizing NLDAS-2 forcing data in conjunction with the Noah-MP surface flow simulation for generating a satisfactory thermal lake regime. The capability of GLM to be linked to the biogeochemical and ecological modeling libraries, such as the aquatic eco-dynamic model (AED-2), holds promise for the future implementation of GLM-AED2. The findings of the current study shed light on the potential of this integrated approach, enabling interactive simulations encompassing a diverse range of water-quality variables, including dissolved oxygen (DO) and sediment flux. In case sufficient biogeochemical data can be gathered to train such models in the Marion Reservoir, this integrated framework can empower researchers to gain valuable insights into the ecological functioning of the reservoir.

Furthermore, the integration of Noah-MP with GLM represents a significant advancement in land surface modeling, specifically addressing the limitation of neglecting the impacts of impoundments and reservoir operations in the current Noah-MP (Kumar et al., 2019; Ma et al., 2017). By merging these two models, a more comprehensive and accurate evaluation of land surface hydrologic fluxes becomes possible, leading to enhanced land-water management practices.

Chapter 5: Conclusion and Future Work

This dissertation found new insights that hold potential for enhancing the prediction of the lake water column thermal regime, a fundamental physical characteristic of lakes and reservoir systems in ungauged catchments using physics-based models. Accurate real-time prediction of water temperature at different depths, on an hourly time scale, plays a crucial role in assessing the profound impact of climate change on shallow polymictic aquatic systems. By providing valuable insights into temperature dynamics, this research enables a comprehensive evaluation of the impact that a wide range of environmental variables exert on these ecosystems. Moreover, this information empowers decision-makers to prioritize and implement effective actions for the management and conservation of aquatic resources.

In Chapter 2, the study focused on examining the role of the dynamic vegetation function in Noah-MP in relation to important water and carbon budget terms. This analysis involved comparing six distinct model configurations with field measurements. The variations observed among each version primarily stemmed from the different calculation approaches employed for the Leaf Area Index (LAI) and Fraction of Vegetation (FVEG). Results indicate that despite the variability in latent heat flux (LE) components, including transpiration, canopy evaporation, and soil evaporation, across different model configurations, the total LE remains relatively unchanged. This insensitivity can be attributed to the prevailing influence of net radiation (Rn), which dominates the overall LE dynamics, particularly when there is sufficient soil moisture available. The underestimation of simulated streamflow, in comparison to USGS gauge measurements, can be attributed to an overestimation of evaporation. This discrepancy is characterized by the underestimation of peak-flow magnitudes, suggesting that a larger portion of water should be retained within the soil layers rather than being evaporated into the atmosphere. At the domain level, the divergence in evaporation patterns between the models and MODIS in irrigated croplands can be primarily attributed to disparities in prescribed and actual land cover classes, as well as limitations in the irrigation routine within Noah-MP. The comparison between gridded soil moisture (SM) percentile and USDM drought categories for two specific drought events in 2012 and 2018 revealed that the newer version of Noah-MP (v4.0.1) outperformed the older version 3.6 in reproducing spatial patterns of drought that closely aligned with the USDM.

Chapter 3 investigates the relationship between key meteorological factors and the thermal and dissolved oxygen (DO) cycles in a hypereutrophic discontinuous polymictic reservoir using a range of indices and statistical approaches. Additionally, it explores the influence of water column mixing on nutrient and metal dynamics, and how these factors contribute to the emergence and propagation of CyanoHABs. The study utilizes high-frequency data to provide insights into the complex interactions and processes occurring within the reservoir, shedding light on the mechanisms driving the dynamics of both physical and biological variables. The findings from a comprehensive 2-year high-frequency time-series monitoring campaign reveal important insights into the factors influencing the occurrence of CyanoHABs. The results demonstrate that specific meteorological conditions, such as calm and warm weather (wind speed < 2 m/s and temperature > 23 °C), along with a strong thermal stratification (indicated by a LakeNumber (L_N) greater than 1), significantly increase the likelihood of CyanoHABs. However, it should be noted that no significant statistical correlation was observed between wind speed and CyanoHABs, which could potentially be attributed to the limited number of field samples and the duration of the study.

Building upon the insights gained in Chapter 3, Chapter 4 establishes a procedure for integrating the general lake model (GLM) into widely adopted land surface models such as Noah-

MP. The primary focus of this integration is to simulate the hydrodynamic and thermal characteristics of a hypereutrophic polymictic reservoir. To achieve this objective, the study follows a two-fold approach. Firstly, the GLM model is executed using in situ meteorological data and inflow measurements obtained from the U.S. Army Corps of Engineers (USACE). Secondly, the study employs freely available and comprehensive NLDAS-2 datasets to provide the necessary forcing data for the GLM model, in conjunction with Noah-MP's runoff predictions. The results indicated that GLM could successfully reproduce the complex patterns and variations in reservoir water temperatures using both NLDAS-2 data coupled with simulated Noah-MP inflow and measurements from the USACE as forcing drivers. Although there was generally good agreement between the simulated and observed water temperatures throughout the calibration and validation periods, it is important to acknowledge that the GLM model exhibited minor inconsistencies in simulating water levels and tended to underestimate surface layer water temperatures.

Taken together this study demonstrates the potential for enhancing predictions of inland freshwater physical dynamics by utilizing process-based models rooted in fundamental physical principles. Additionally, these findings can contribute to improving forecasts of various biological, physical, and chemical processes, including the distribution of dissolved oxygen, underwater light penetration, nutrient exchange between the epilimnion and hypolimnion, and phytoplankton dynamics.

5.1 Limitations and Recommendations for Future Work

Despite the robustness of our study, it is crucial to acknowledge the limitations associated with Noah-MP and GLM simulations. These simulations tend to exhibit a remarkably uniform water column temperature, deviating from the actual conditions observed in reality. Additionally, they frequently fail to capture the occurrence of short-term stratification events that commonly take place during the summer season. Also, it is important to acknowledge the limitations associated with the USACE field measurements. These measurements primarily focus on streamflow from one major river thereby lacking information on inflow measurements from other tributaries. This introduces uncertainties in our analysis, as it is possible that these measurements may have missed certain flow paths and their associated dynamics. We also recognize the importance of long-term monitoring data in refining numerical models through calibration, as it presents a valuable opportunity to enhance their accuracy. In addition, the availability of multi-year datasets serves as valuable training data for machine learning algorithms, such as random forest decision trees, which were effectively utilized in our study. This approach ensures the identification of relevant factors that have a significant impact on the dynamics of Cyanobacterial Harmful Algal Blooms (CyanoHABs) in shallow reservoirs, thereby providing more reliable results. To further enhance the accuracy and reliability of cyanobacterial biomass estimation, additional measurements of cyanobacterial community composition could be incorporated. In particular, including measurements such as phytoplankton biovolume, phytoplankton community composition at genera taxonomic level, and laboratory spectrophotometry determination of chlorophyll *a* (chl-a) would complement the portable FluoroProbe measurements and provide a more comprehensive understanding of cyanobacteria biomass.

Considering that a significant proportion of lakes and water bodies in Kansas are artificially created, it becomes imperative to prioritize measures that guarantee the preservation of high-quality drinking water within these reservoirs. Moreover, Kansas reservoirs exhibit a common trait of being shallow and hypereutrophic, with many of them already experiencing recurring harmful algal blooms (CyanoHABs) or being susceptible to such occurrences. As future work, the integration of GLM with biogeochemical and ecological modeling libraries, such as the aquatic eco-dynamic model (AED-2), holds promise for the implementation of GLM-AED2. Building upon the findings of this study, further exploration of this combined approach can provide valuable insights into interactive simulations that encompass a wide range of water-quality factors, including dissolved oxygen (DO) levels, sediment flux, and phytoplankton community dynamics. To effectively calibrate the AED-2 component, a promising approach is to leverage high-frequency in situ phycocyanin measurements. In prospective investigations, the incorporation of high-frequency in situ phycocyanin measurements, specifically obtained through the Cyclops-7 phycocyanin sensor, presents a valuable avenue for calibrating the GLM-AED-2 model. Such integration has the potential to advance our understanding of the complex dynamics of aquatic ecosystems and contribute to more comprehensive assessments of water quality.

References

Adrian, R., O'Reilly, C. M., Zagarese, H., Baines, S. B., Hessen, D. O., Keller, W., Livingstone, D. M., Sommaruga, R., Straile, D., Van Donk, E., Weyhenmeyer, G. A., & Winder, M. (2009). Lakes as sentinels of climate change. *Limnology and Oceanography*, *54*(6part2), 2283–2297. https://doi.org/10.4319/lo.2009.54.6_part_2.2283

Alboukadel, K. (2021). *Rstatix: Pipe-Friendly Framework for Basic Statistical Tests. R package version 0.7.0* (0.7.0) [Computer software].

Almeida, M. C., Shevchuk, Y., Kirillin, G., Soares, P. M. M., Cardoso, R. M., Matos, J. P., Rebelo, R. M., Rodrigues, A. C., & Coelho, P. S. (2022). Modeling reservoir surface temperatures for regional and global climate models: A multi-model study on the inflow and level variation effects. *Geoscientific Model Development*, *15*(1), 173–197. https://doi.org/10.5194/gmd-15-173-2022

Ambrosetti, W., & Barbanti, L. (2002). Physical limnology of Italian lakes. 2. Relationships between morphometric parameters, stability and Birgean work. *Journal of Limnology*, *61*(2), 159–167. https://doi.org/10.4081/jlimnol.2002.159

Anandhi, A., & Knapp, M. (2016). How does the drought of 2012 compare to earlier droughts in Kansas, USA? *Journal of Service Climatology*, *9*(1). https://doi.org/10.46275/JoASC.2016.05.001

Arsenault, K. R., Nearing, G. S., Wang, S., Yatheendradas, S., & Peters-Lidard, C. D. (2018). Parameter Sensitivity of the Noah-MP Land Surface Model with Dynamic Vegetation. *Journal of Hydrometeorology*, *19*(5), 815–830. https://doi.org/10.1175/jhm-d-17-0205.1

Baldocchi, D., Falge, E., Gu, L., Olson, R., Hollinger, D., Running, S., Anthoni, P., Bernhofer, C., Davis, K., Evans, R., Fuentes, J., Goldstein, A., Katul, G., Law, B., Lee, X., Malhi, Y., Meyers, T., Munger, W., Oechel, W., … Wofsy, S. (2001). FLUXNET: A New Tool to Study the Temporal and Spatial Variability of Ecosystem–Scale Carbon Dioxide, Water Vapor, and Energy Flux Densities. *Bulletin of the American Meteorological Society*, *82*(11), 2415–2434. https://doi.org/10.1175/1520-0477(2001)082<2415:FANTTS>2.3.CO;2

Ball, J. T., Woodrow, I. E., & Berry, J. A. (1987). A Model Predicting Stomatal Conductance and its Contribution to the Control of Photosynthesis under Different Environmental Conditions. In J. Biggins (Ed.), *Progress in Photosynthesis Research* (pp. 221–224). Springer Netherlands. https://doi.org/10.1007/978-94-017-0519-6_48

Barnes, P. L., & Devlin, D. L. (2008). Marion Reservoir Kansas Watershed Restoration. *2008 Providence, Rhode Island, June 29 - July 2, 2008*. 2008 Providence, Rhode Island, June 29 - July 2, 2008. https://doi.org/10.13031/2013.24719

Bartz, E., Zaefferer, M., Mersmann, O., & Bartz-Beielstein, T. (2021). *Experimental Investigation and Evaluation of Model-based Hyperparameter Optimization* (arXiv:2107.08761). arXiv. http://arxiv.org/abs/2107.08761

Best, M. J., Abramowitz, G., Johnson, H. R., Pitman, A. J., Balsamo, G., Boone, A., Cuntz, M., Decharme, B., Dirmeyer, P. A., Dong, J., Ek, M., Guo, Z., Haverd, V., Van Den Hurk, B. J. J., Nearing, G. S., Pak, B., Peters-Lidard, C., Santanello, J. A., Stevens, L., & Vuichard, N. (2015). The Plumbing of Land Surface Models: Benchmarking Model Performance. *Journal of Hydrometeorology*, *16*(3), 1425–1442. https://doi.org/10.1175/JHM-D-14-0158.1

Beutel, M. W., Leonard, T. M., Dent, S. R., & Moore, B. C. (2008). Effects of aerobic and anaerobic conditions on P, N, Fe, Mn, and Hg accumulation in waters overlaying profundal sediments of an oligo-mesotrophic lake. *Water Research*, *42*(8–9), 1953–1962. https://doi.org/10.1016/j.watres.2007.11.027

Boehrer, B., Fukuyama, R., & Chikita, K. (2008). Stratification of very deep, thermally stratified lakes. *Geophysical Research Letters*, *35*(16), L16405. https://doi.org/10.1029/2008GL034519

Boström, B., Andersen, J. M., Fleischer, S., & Jansson, M. (1988). Exchange of phosphorus across the sediment-water interface. *Hydrobiologia*, *170*(1), 229–244. https://doi.org/10.1007/BF00024907

Bruce, L. C., Frassl, M. A., Arhonditsis, G. B., Gal, G., Hamilton, D. P., Hanson, P. C., Hetherington, A. L., Melack, J. M., Read, J. S., Rinke, K., Rigosi, A., Trolle, D., Winslow, L., Adrian, R., Ayala, A. I., Bocaniov, S. A., Boehrer, B., Boon, C., Brookes, J. D., … Hipsey, M. R. (2018). A multi-lake comparative analysis of the General Lake Model (GLM): Stress-testing across a global observatory network. *Environmental Modelling & Software*, *102*, 274–291. https://doi.org/10.1016/j.envsoft.2017.11.016

Brunsell, N. A., De Oliveira, G., Barlage, M., Shimabukuro, Y., Moraes, E., & Aragão, L. (2021). Examination of seasonal water and carbon dynamics in eastern Amazonia: A comparison of Noah-MP and MODIS. *Theoretical and Applied Climatology*, *143*(1–2), 571–586. https://doi.org/10.1007/s00704-020-03435-6

Brunsell, N. A., Ham, J. M., & Owensby, C. E. (2008). Assessing the multi-resolution information content of remotely sensed variables and elevation for evapotranspiration in a tall-grass prairie environment. *Remote Sensing of Environment*, *112*(6), 2977–2987. https://doi.org/10.1016/j.rse.2008.02.002

Brunsell, N. A., Nippert, J. B., & Buck, T. L. (2013). Impacts of seasonality and surface heterogeneity on water-use efficiency in mesic grasslands: WATER-USE EFFICIENCY IN MESIC GRASSLANDS. *Ecohydrology*, 1223–1233. https://doi.org/10.1002/eco.1455

Brunsell, N. A., Schymanski, S. J., & Kleidon, A. (2011). Quantifying the thermodynamic entropy budget of the land surface: Is this useful? *Earth System Dynamics*, *2*(1), 87–103. https://doi.org/10.5194/esd-2-87-2011

Brunsell, N. A., Van Vleck, E. S., Nosshi, M., Ratajczak, Z., & Nippert, J. B. (2017). Assessing the Roles of Fire Frequency and Precipitation in Determining Woody Plant Expansion in Central U.S. Grasslands. *Journal of Geophysical Research: Biogeosciences*, *122*(10), 2683–2698. https://doi.org/10.1002/2017JG004046

Bueche, T., Hamilton, D. P., & Vetter, M. (2017). Using the General Lake Model (GLM) to simulate water temperatures and ice cover of a medium-sized lake: A case study of Lake Ammersee, Germany. *Environmental Earth Sciences*, *76*(13), 461. https://doi.org/10.1007/s12665-017-6790-7

Bueche, T., Wenk, M., Poschlod, B., Giadrossich, F., Pirastru, M., & Vetter, M. (2020). glmGUI v1.0: An R-based graphical user interface and toolbox for GLM (General Lake Model) simulations. *Geoscientific Model Development*, *13*(2), 565–580. https://doi.org/10.5194/gmd-13-565-2020

Buermann, W., Forkel, M., O'Sullivan, M., Sitch, S., Friedlingstein, P., Haverd, V., Jain, A. K., Kato, E., Kautz, M., Lienert, S., Lombardozzi, D., Nabel, J. E. M. S., Tian, H., Wiltshire, A. J., Zhu, D., Smith, W. K., & Richardson, A. D. (2018). Widespread seasonal compensation effects of spring warming on northern plant productivity. *Nature*, *562*(7725), 110–114. https://doi.org/10.1038/s41586-018-0555-7

Cai, X., Yang, Z.-L., David, C. H., Niu, G.-Y., & Rodell, M. (2014). Hydrological evaluation of the Noah-MP land surface model for the Mississippi River Basin: HYDROLOGICAL EVALUATION OF NOAH-MP. *Journal of Geophysical Research: Atmospheres, 119*(1), 23–38. https://doi.org/10.1002/2013JD020792

Chang, M., Liao, W., Wang, X., Zhang, Q., Chen, W., Wu, Z., & Hu, Z. (2020). An optimal ensemble of the Noah-MP land surface model for simulating surface heat fluxes over a typical subtropical forest in South China. *Agricultural and Forest Meteorology, 281*, 107815. https://doi.org/10.1016/j.agrformet.2019.107815

Chen, L. G., Hartman, A., Pugh, B., Gottschalck, J., & Miskus, D. (2020). Real-Time Prediction of Areas Susceptible to Flash Drought Development. *Atmosphere*, *11*(10), 1114. https://doi.org/10.3390/atmos11101114

Claussen, M., Bathiany, S., Brovkin, V., & Kleinen, T. (2013). Simulated climate–vegetation interaction in semi-arid regions affected by plant diversity. *Nature Geoscience, 6*(11), 954–958. https://doi.org/10.1038/ngeo1962

Cole, G. A., & Kilham, P. (1975). Textbook of limnology. Mosby, Saint Louis. *Limnology and Oceanography*, *21*(1), 186–187. https://doi.org/10.4319/lo.1976.21.1.0186b

Collatz, G. J., Ball, J. T., Grivet, C., & Berry, J. A. (1991). Physiological and environmental regulation of stomatal conductance, photosynthesis and transpiration: A model that includes a laminar boundary layer. *Agricultural and Forest Meteorology*, *54*(2–4), 107–136. https://doi.org/10.1016/0168-1923(91)90002-8

Collatz, G., Ribas-Carbo, M., & Berry, J. (1992). Coupled Photosynthesis-Stomatal Conductance Model for Leaves of C4 Plants. *Functional Plant Biology, 19*(5), 519–538. https://doi.org/10.1071/PP9920519

Coman, M. A., & Wells, M. G. (2012). Temperature variability in the nearshore benthic boundary layer of Lake Opeongo is due to wind-driven upwelling events. *Canadian Journal of Fisheries and Aquatic Sciences*, *69*(2), 282–296. https://doi.org/10.1139/f2011-167

Cuntz, M., Mai, J., Samaniego, L., Clark, M., Wulfmeyer, V., Branch, O., Attinger, S., & Thober, S. (2016). The impact of standard and hard-coded parameters on the hydrologic fluxes in the Noah-MP land surface model: HARD-CODED PARAMETERS IN NOAH-MP. *Journal of Geophysical Research: Atmospheres*, *121*(18), 10,676-10,700. https://doi.org/10.1002/2016JD025097

De Kauwe, M. G., Medlyn, B. E., Walker, A. P., Zaehle, S., Asao, S., Guenet, B., Harper, A. B., Hickler, T., Jain, A. K., Luo, Y., Lu, X., Luus, K., Parton, W. J., Shu, S., Wang, Y., Werner, C., Xia, J., Pendall, E., Morgan, J. A., … Norby, R. J. (2017). Challenging terrestrial biosphere models with data from the long-term multifactor Prairie Heating and CO $_2$ Enrichment experiment. *Global Change Biology*, *23*(9), 3623–3645. https://doi.org/10.1111/gcb.13643

De Oliveira, G., Brunsell, N. A., Sutherlin, C. E., Crews, T. E., & DeHaan, L. R. (2018). Energy, water and carbon exchange over a perennial Kernza wheatgrass crop. *Agricultural and Forest Meteorology*, *249*, 120–137. https://doi.org/10.1016/j.agrformet.2017.11.022

Delfino, J. J., & Fred Lee, G. (1971). Variation of manganese, dissolved oxygen and related chemical parameters in the bottom waters of Lake Mendota, Wisconsin. *Water Research*, *5*(12), 1207–1217. https://doi.org/10.1016/0043-1354(71)90085-6

Dickinson, R. E., Shaikh, M., Bryant, R., & Graumlich, L. (1998). Interactive Canopies for a Climate Model. *Journal of Climate*, *11*(11), 2823–2836. https://doi.org/10.1175/1520-0442(1998)011<2823:ICFACM>2.0.CO;2

Dodds, W. K., & Whiles, M. R. (2010). *Freshwater ecology: Concepts and environmental applications of limnology* (Third edition). Elsevier, Academic Press.

Downing, J. A., Watson, S. B., & McCauley, E. (2001). Predicting Cyanobacteria dominance in lakes. *Canadian Journal of Fisheries and Aquatic Sciences, 58*(10), 1905–1908. https://doi.org/10.1139/f01-143

Dzialowski, A. R., Lim, N. C., Liechti, P. M., & Beury, J. H. (2007). *Internal Nutrient Recycling in Marion Reservoir*. Kansas Biological Survey.

Dzialowski, A. R., Smith, V. H., Wang, S.-H., Martin, M. C., & Jr., F. deNoyelles. (2011). Effects of non-algal turbidity on cyanobacterial biomass in seven turbid Kansas reservoirs. *Lake and Reservoir Management*, *27*(1), 6–14. https://doi.org/10.1080/07438141.2011.551027

Dzialowski, A. R., Wang, S.-H., Lim, N.-C., Spotts, W. W., & Huggins, D. G. (2005). Nutrient limitation of phytoplankton growth in central plains reservoirs, USA. *Journal of Plankton Research*, *27*(6), 587–595. https://doi.org/10.1093/plankt/fbi034

Ek, M. B., Mitchell, K. E., Lin, Y., Rogers, E., Grunmann, P., Koren, V., Gayno, G., & Tarpley, J. D. (2003). Implementation of Noah land surface model advances in the National Centers for Environmental Prediction operational mesoscale Eta model. *Journal of Geophysical Research: Atmospheres*, *108*(D22), 2002JD003296. https://doi.org/10.1029/2002JD003296

Entekhabi, D., Njoku, E. G., O'Neill, P. E., Kellogg, K. H., Crow, W. T., Edelstein, W. N., Entin, J. K., Goodman, S. D., Jackson, T. J., Johnson, J., Kimball, J., Piepmeier, J. R., Koster, R. D., Martin, N., McDonald, K. C., Moghaddam, M., Moran, S., Reichle, R., Shi, J. C., … Van Zyl, J. (2010). The Soil Moisture Active Passive (SMAP) Mission. *Proceedings of the IEEE*, *98*(5), 704–716. https://doi.org/10.1109/JPROC.2010.2043918

Ferris, J. M., & Burton, H. R. (1988). The annual cycle of heat content and mechanical stability of hypersaline Deep Lake, Vestfold Hills, Antarctica. *Hydrobiologia*, *165*(1), 115–128. https://doi.org/10.1007/BF00025579

Fowler, K., Peel, M., Western, A., & Zhang, L. (2018). Improved Rainfall-Runoff Calibration for Drying Climate: Choice of Objective Function. *Water Resources Research*, *54*(5), 3392–3408. https://doi.org/10.1029/2017WR022466

Frassl, M., Boehrer, B., Holtermann, P., Hu, W., Klingbeil, K., Peng, Z., Zhu, J., & Rinke, K. (2018). Opportunities and Limits of Using Meteorological Reanalysis Data for Simulating Seasonal to Sub-Daily Water Temperature Dynamics in a Large Shallow Lake. *Water*, *10*(5), 594. https://doi.org/10.3390/w10050594

Gao, Y., Li, K., Chen, F., Jiang, Y., & Lu, C. (2015). Assessing and improving Noah-MP land model simulations for the central Tibetan Plateau. *Journal of Geophysical Research: Atmospheres*, *120*(18), 9258–9278. https://doi.org/10.1002/2015JD023404

Gardner, K. (2017). *Gallatin River Task Force Community Water Quality Monitoring Program Sampling and Analysis Plan*. Montana Department of Environmental Quality.

Gayler, S., Wöhling, T., Grzeschik, M., Ingwersen, J., Wizemann, H.-D., Warrach-Sagi, K., Högy, P., Attinger, S., Streck, T., & Wulfmeyer, V. (2014). Incorporating dynamic root growth enhances the performance of Noah-MP at two contrasting winter wheat field sites. *Water Resources Research*, *50*(2), 1337–1356. https://doi.org/10.1002/2013WR014634

Ghimire, G. R., Sharma, S., Panthi, J., Talchabhadel, R., Parajuli, B., Dahal, P., & Baniya, R. (2020). Benchmarking Real-Time Streamflow Forecast Skill in the Himalayan Region. *Forecasting*, *2*(3), 230–247. https://doi.org/10.3390/forecast2030013

Gim, H.-J., Park, S. K., Kang, M., Thakuri, B. M., Kim, J., & Ho, C.-H. (2017). An improved parameterization of the allocation of assimilated carbon to plant parts in vegetation dynamics for Noah-MP: PARAMETERIZATION OF CARBON ALLOCATION. *Journal of Advances in Modeling Earth Systems*, *9*(4), 1776–1794. https://doi.org/10.1002/2016MS000890

Gobler, C. J., Burkholder, J. M., Davis, T. W., Harke, M. J., Johengen, T., Stow, C. A., & Van De Waal, D. B. (2016). The dual role of nitrogen supply in controlling the growth and toxicity of cyanobacterial blooms. *Harmful Algae*, *54*, 87–97. https://doi.org/10.1016/j.hal.2016.01.010

Gong, L., Widén-Nilsson, E., Halldin, S., & Xu, C.-Y. (2009). Large-scale runoff routing with an aggregated network-response function. *Journal of Hydrology*, *368*(1–4), 237–250. https://doi.org/10.1016/j.jhydrol.2009.02.007

Gotoh, S., & Patrick, W. H. (1974). Transformation of Iron in a Waterlogged Soil as Influenced by Redox Potential and pH. *Soil Science Society of America Journal*, *38*(1), 66–71. https://doi.org/10.2136/sssaj1974.03615995003800010024x

Gray, E., Elliott, J. A., Mackay, E. B., Folkard, A. M., Keenan, P. O., & Jones, I. D. (2019). Modelling lake cyanobacterial blooms: Disentangling the climate-driven impacts of changing mixed depth and water temperature. *Freshwater Biology*, *64*(12), 2141–2155. https://doi.org/10.1111/fwb.13402

Gupta, H. V., Kling, H., Yilmaz, K. K., & Martinez, G. F. (2009). Decomposition of the mean squared error and NSE performance criteria: Implications for improving hydrological modelling. *Journal of Hydrology*, *377*(1–2), 80–91. https://doi.org/10.1016/j.jhydrol.2009.08.003

Hansen, N. (2006). The CMA Evolution Strategy: A Comparing Review. In *Towards a New Evolutionary Computation: Advances in the estimation of distribution algorithms* (pp. 75–102).

Hargrove, W. L., Johnson, D., Snethen, D., & Middendorf, J. (2010). From Dust Bowl to Mud Bowl: Sedimentation, conservation measures, and the future of reservoirs. *Journal of Soil and Water Conservation*, *65*(1), 14A-17A. https://doi.org/10.2489/jswc.65.1.14A

Harris, T. D., Wilhelm, F. M., Graham, J. L., & Loftin, K. A. (2014). Experimental manipulation of TN:TP ratios suppress cyanobacterial biovolume and microcystin concentration in large-scale *in situ* mesocosms. *Lake and Reservoir Management*, *30*(1), 72–83. https://doi.org/10.1080/10402381.2013.876131

Harris, T. D., Yun, J., Baker, D., Kastens, J., Sturm, B., Leavitt, P., Ketterer, M., & Amand, A. St. (2020). *Phytoplankton and water quality in Marion and Keith Sebelius reservoirs: Results of paleolimnological sediment core and historical data analyses*. Kansas Biological Survey.

Harrison, J. W., Howell, E. T., Watson, S. B., & Smith, R. E. H. (2016). Improved estimates of phytoplankton community composition based on in situ spectral fluorescence: Use of ordination and field-derived norm spectra for the bbe FluoroProbe. *Canadian Journal of*

Fisheries and Aquatic Sciences, *73*(10), 1472–1482. https://doi.org/10.1139/cjfas-2015-0360

Havel, J. E., Lee, C. E., & Vander Zanden, M. J. (2005). Do Reservoirs Facilitate Invasions into Landscapes? *BioScience*, *55*(6), 518–525. https://doi.org/10.1641/0006-3568(2005)055[0518:DRFIIL]2.0.CO;2

Hayes, M. J., Svoboda, M. D., Wardlow, B. D., Anderson, M. C., & Kogan, F. (2012). *Drought monitoring: Historical and current perspectives*. Drought Mitigation Center Faculty Publications. https://digitalcommons.unl.edu/droughtfacpub/94/

Hayes, N. M., Deemer, B. R., Corman, J. R., Razavi, N. R., & Strock, K. E. (2017). Key differences between lakes and reservoirs modify climate signals: A case for a new conceptual model. *Limnology and Oceanography Letters*, *2*(2), 47–62. https://doi.org/10.1002/lol2.10036

He, C., Valayamkunnath, P., Barlage, M., Chen, F., Gochis, D., Cabell, R., Schneider, T., Rasmussen, R., Niu, G.-Y., Yang, Z.-L., Niyogi, D., & Ek, M. (2023). *Modernizing the open-source community Noah-MP land surface model (version 5.0) with enhanced modularity, interoperability, and applicability* [Preprint]. Climate and Earth system modeling. https://doi.org/10.5194/egusphere-2023-675

Heinsch, F. A., Maosheng Zhao, Running, S. W., Kimball, J. S., Nemani, R. R., Davis, K. J., Bolstad, P. V., Cook, B. D., Desai, A. R., Ricciuto, D. M., Law, B. E., Oechel, W. C., Hyojung Kwon, Hongyan Luo, Wofsy, S. C., Dunn, A. L., Munger, J. W., Baldocchi, D. D., Liukang Xu, … Flanagan, L. B. (2006). Evaluation of remote sensing based terrestrial productivity from MODIS using regional tower eddy flux network observations. *IEEE*

Transactions on Geoscience and Remote Sensing, *44*(7), 1908–1925. https://doi.org/10.1109/TGRS.2005.853936

Hipsey, M. R., Bruce, L. C., Boon, C., Busch, B., Carey, C. C., Hamilton, D. P., Hanson, P. C., Read, J. S., De Sousa, E., Weber, M., & Winslow, L. A. (2019). A General Lake Model (GLM 3.0) for linking with high-frequency sensor data from the Global Lake Ecological Observatory Network (GLEON). *Geoscientific Model Development*, *12*(1), 473–523. https://doi.org/10.5194/gmd-12-473-2019

Hipsey, M. R., Salmon, S. U., & Mosley, L. M. (2014). A three-dimensional hydro-geochemical model to assess lake acidification risk. *Environmental Modelling & Software*, *61*, 433–457. https://doi.org/10.1016/j.envsoft.2014.02.007

Hondzo, M., & Stefan, H. G. (1993). Regional water temperature characteristics of lakes subjected to climate change. *Climatic Change*, *24*(3), 187–211. https://doi.org/10.1007/BF01091829

Hosseini, A., Mocko, D. M., Brunsell, N. A., Kumar, S. V., Mahanama, S., Arsenault, K., & Roundy, J. K. (2022). Understanding the impact of vegetation dynamics on the water cycle in the Noah-MP model. *Frontiers in Water*, *4*, 925852. https://doi.org/10.3389/frwa.2022.925852

Hoyer, M. V., & Jones, J. R. (1983). Factors Affecting the Relation Between Phosphorus and Chlorophyll *a* in Midwestern Reservoirs. *Canadian Journal of Fisheries and Aquatic Sciences*, *40*(2), 192–199. https://doi.org/10.1139/f83-029

Hupfer, M., & Lewandowski, J. (2008). Oxygen Controls the Phosphorus Release from Lake Sediments—A Long-Lasting Paradigm in Limnology. *International Review of Hydrobiology*, *93*(4–5), 415–432. https://doi.org/10.1002/iroh.200711054

Hutchinson, G. E. (1967). *A treatise on limnology, introduction to lake biology and the limnoplankton* (Vol. 2). Wiley.

Ibelings, B. W., Kurmayer, R., Azevedo, S. M. F. O., & Wood, S. A. (2021). Understanding the occurrence of cyanobacteria and cyanotoxins. In I. Chorus & M. Welker (Eds.), *Toxic cyanobacteria in water: A guide to their public health consequences, monitoring and management* (2nd ed., pp. 213–294).

Ingwersen, J., Högy, P., Wizemann, H. D., Warrach-Sagi, K., & Streck, T. (2018). Coupling the land surface model Noah-MP with the generic crop growth model Gecros: Model description, calibration and validation. *Agricultural and Forest Meteorology*, *262*, 322–339. https://doi.org/10.1016/j.agrformet.2018.06.023

Ise, T., Litton, C. M., Giardina, C. P., & Ito, A. (2010). Comparison of modeling approaches for carbon partitioning: Impact on estimates of global net primary production and equilibrium biomass of woody vegetation from MODIS GPP. *Journal of Geophysical Research*, *115*(G4), G04025. https://doi.org/10.1029/2010JG001326

Jankowski, T., Livingstone, D. M., Bührer, H., Forster, R., & Niederhauser, P. (2006). Consequences of the 2003 European heat wave for lake temperature profiles, thermal stability, and hypolimnetic oxygen depletion: Implications for a warmer world. *Limnology and Oceanography*, *51*(2), 815–819. https://doi.org/10.4319/lo.2006.51.2.0815

Jasechko, S., Sharp, Z. D., Gibson, J. J., Birks, S. J., Yi, Y., & Fawcett, P. J. (2013). Terrestrial water fluxes dominated by transpiration. *Nature*, *496*(7445), 347–350. https://doi.org/10.1038/nature11983

Jones, J. R., & Knowlton, M. F. (1993). Limnology Of Missouri Reservoirs: An Analysis of Regional Patterns. *Lake and Reservoir Management*, *8*(1), 17–30. https://doi.org/10.1080/07438149309354455

Kaste, J. M., Heimsath, A. M., & Hohmann, M. (2006). Quantifying sediment transport across an undisturbed prairie landscape using cesium-137 and high resolution topography. *Geomorphology*, *76*(3–4), 430–440. https://doi.org/10.1016/j.geomorph.2005.12.007

KBS. (2010). *Bathymetric and Sediment Survey of Marion Reservoir, Marion County, Kansas* [Applied Science and Technology for Reservoir Assessment (ASTRA) Program report 2008-03]. Kansas Biological Survey, Kansas Water Office. https://www.yumpu.com/en/document/read/51082852/marion-reservoir-marion-county-ks-kansas-water-office

KDHE. (2002). *Neosho River Basin Total Maximum Daily Load*. Kansas Department of Health and Environment. https://www.kdhe.ks.gov/DocumentCenter/View/14836/Marion-Lake-PDF

Kerimoglu, O., & Rinke, K. (2013). Stratification dynamics in a shallow reservoir under different hydro-meteorological scenarios and operational strategies: NONWINTER STRATIFICATION DYNAMICS. *Water Resources Research*, *49*(11), 7518–7527. https://doi.org/10.1002/2013WR013520

Kjensmo, J. (1994). Internal energy, the work of the wind, and the thermal stability in Lake Tyrifjord, southeastern Norway. *Hydrobiologia*, *286*(1), 53–59. https://doi.org/10.1007/BF00007280

Knoben, W. J. M., Freer, J. E., & Woods, R. A. (2019). Technical note: Inherent benchmark or not? Comparing Nash–Sutcliffe and Kling–Gupta efficiency scores. *Hydrology and Earth System Sciences*, *23*(10), 4323–4331. https://doi.org/10.5194/hess-23-4323-2019

Kreling, J., Bravidor, J., Engelhardt, C., Hupfer, M., Koschorreck, M., & Lorke, A. (2017). The importance of physical transport and oxygen consumption for the development of a metalimnetic oxygen minimum in a lake: Metalimnetic oxygen minimum. *Limnology and Oceanography*, *62*(1), 348–363. https://doi.org/10.1002/lno.10430

Kumar, S., Peterslidard, C., Tian, Y., Houser, P., Geiger, J., Olden, S., Lighty, L., Eastman, J., Doty, B., & Dirmeyer, P. (2006). Land information system: An interoperable framework for high resolution land surface modeling. *Environmental Modelling & Software*, *21*(10), 1402–1415. https://doi.org/10.1016/j.envsoft.2005.07.004

Kumar, S. V., M. Mocko, D., Wang, S., Peters-Lidard, C. D., & Borak, J. (2019). Assimilation of Remotely Sensed Leaf Area Index into the Noah-MP Land Surface Model: Impacts on Water and Carbon Fluxes and States over the Continental United States. *Journal of Hydrometeorology*, *20*(7), 1359–1377. https://doi.org/10.1175/JHM-D-18-0237.1

Kunkel, K. E., Frankson, R., Runkle, J., Champion, S. M., Stevens, L. E., Easterling, D. R., Stewart, B. C., McCarrick, A., & Lemery (Eds.), C. R. (2022). *2022: State Climate Summaries for the United States 2022* [NOAA Technical Report NESDIS 150]. NOAA/NESDIS.

Ladwig, R., Furusato, E., Kirillin, G., Hinkelmann, R., & Hupfer, M. (2018). Climate Change Demands Adaptive Management of Urban Lakes: Model-Based Assessment of Management Scenarios for Lake Tegel (Berlin, Germany). *Water*, *10*(2), 186. https://doi.org/10.3390/w10020186

Ladwig, R., Hanson, P. C., Dugan, H. A., Carey, C. C., Zhang, Y., Shu, L., Duffy, C. J., & Cobourn, K. M. (2021). Lake thermal structure drives interannual variability in summer anoxia dynamics in a eutrophic lake over 37 years. *Hydrology and Earth System Sciences*, *25*(2), 1009–1032. https://doi.org/10.5194/hess-25-1009-2021

Lehner, B., Verdin, K., & Jarvis, A. (2008). New Global Hydrography Derived From Spaceborne Elevation Data. *Eos, Transactions American Geophysical Union*, *89*(10), 93. https://doi.org/10.1029/2008EO100001

Liang, H., Huang, X., Wang, H., Xu, W., & Shi, B. (2021). The role of extracellular organic matter on the cyanobacteria ultrafiltration process. *Journal of Environmental Sciences*, *110*, 12–20. https://doi.org/10.1016/j.jes.2021.03.010

Lin, P., Rajib, M. A., Yang, Z.-L., Somos-Valenzuela, M., Merwade, V., Maidment, D. R., Wang, Y., & Chen, L. (2018). Spatiotemporal Evaluation of Simulated Evapotranspiration and Streamflow over Texas Using the WRF-Hydro-RAPID Modeling Framework. *JAWRA Journal of the American Water Resources Association*, *54*(1), 40–54. https://doi.org/10.1111/1752-1688.12585

Liu, X., Chen, F., Barlage, M., Zhou, G., & Niyogi, D. (2016). Noah-MP-Crop: Introducing dynamic crop growth in the Noah-MP land surface model: Noah-MP-Crop. *Journal of Geophysical Research: Atmospheres*, *121*(23), 13,953-13,972. https://doi.org/10.1002/2016JD025597

Loftin, K. A., Graham, J. L., Hilborn, E. D., Lehmann, S. C., Meyer, M. T., Dietze, J. E., & Griffith, C. B. (2016). Cyanotoxins in inland lakes of the United States: Occurrence and potential recreational health risks in the EPA National Lakes Assessment 2007. *Harmful Algae*, *56*, 77–90. https://doi.org/10.1016/j.hal.2016.04.001

Lofton, M. E., Leach, T. H., Beisner, B. E., & Carey, C. C. (2020). Relative importance of top-down vs. Bottom-up control of lake phytoplankton vertical distributions varies among fluorescence-based spectral groups. *Limnology and Oceanography, 65*(10), 2485–2501. https://doi.org/10.1002/lno.11465

Logan, K. E., & Brunsell, N. A. (2015). Influence of drought on growing season carbon and water cycling with changing land cover. *Agricultural and Forest Meteorology*, *213*, 217–225. https://doi.org/10.1016/j.agrformet.2015.07.002

Luo, L., Hamilton, D., Lan, J., McBride, C., & Trolle, D. (2018). Autocalibration of a one-dimensional hydrodynamic-ecological model (DYRESM 4.0-CAEDYM 3.1) using a Monte Carlo approach: Simulations of hypoxic events in a polymictic lake. *Geoscientific Model Development*, *11*(3), 903–913. https://doi.org/10.5194/gmd-11-903-2018

Luo, L., Robock, A., Mitchell, K. E., Houser, P. R., Wood, E. F., Schaake, J. C., Lohmann, D., Cosgrove, B., Wen, F., Sheffield, J., Duan, Q., Higgins, R. W., Pinker, R. T., & Tarpley, J. D. (2003). Validation of the North American Land Data Assimilation System (NLDAS) retrospective forcing over the southern Great Plains. *Journal of Geophysical Research: Atmospheres*, *108*(D22), 2002JD003246. https://doi.org/10.1029/2002JD003246

Ma, N., Niu, G.-Y., Xia, Y., Cai, X., Zhang, Y., Ma, Y., & Fang, Y. (2017). A Systematic Evaluation of Noah-MP in Simulating Land-Atmosphere Energy, Water, and Carbon Exchanges Over the Continental United States: Noah-MP Evaluation in CONUS. *Journal of Geophysical Research: Atmospheres, 122*(22), 12,245-12,268. https://doi.org/10.1002/2017JD027597

MacIntyre, S., Jonsson, A., Jansson, M., Aberg, J., Turney, D. E., & Miller, S. D. (2010). Buoyancy flux, turbulence, and the gas transfer coefficient in a stratified lake: TURBULENCE AND GAS EVASION IN LAKES. *Geophysical Research Letters*, *37*(24). https://doi.org/10.1029/2010GL044164

Matheny, A. M., Bohrer, G., Vogel, C. S., Morin, T. H., He, L., Frasson, R. P. D. M., Mirfenderesgi, G., Schäfer, K. V. R., Gough, C. M., Ivanov, V. Y., & Curtis, P. S. (2014). Species-specific transpiration responses to intermediate disturbance in a northern hardwood forest. *Journal of Geophysical Research: Biogeosciences*, *119*(12), 2292–2311. https://doi.org/10.1002/2014JG002804

Mellios, N., Kofinas, D., Laspidou, C., & Papadimitriou, T. (2015). Mathematical Modeling of Trophic State and Nutrient Flows of Lake Karla using the PCLake Model. *Environmental Processes*, *2*(S1), 85–100. https://doi.org/10.1007/s40710-015-0098-y

Mesinger, F., DiMego, G., Kalnay, E., Mitchell, K., Shafran, P. C., Ebisuzaki, W., Jović, D., Woollen, J., Rogers, E., Berbery, E. H., Ek, M. B., Fan, Y., Grumbine, R., Higgins, W., Li, H., Lin, Y., Manikin, G., Parrish, D., & Shi, W. (2006). North American Regional Reanalysis. *Bulletin of the American Meteorological Society*, *87*(3), 343–360. https://doi.org/10.1175/BAMS-87-3-343

Mesman, J. P., Ayala, A. I., Adrian, R., De Eyto, E., Frassl, M. A., Goyette, S., Kasparian, J., Perroud, M., Stelzer, J. A. A., Pierson, D. C., & Ibelings, B. W. (2020). Performance of one-dimensional hydrodynamic lake models during short-term extreme weather events. *Environmental Modelling & Software*, *133*, 104852. https://doi.org/10.1016/j.envsoft.2020.104852

Mi, C., Shatwell, T., Ma, J., Wentzky, V. C., Boehrer, B., Xu, Y., & Rinke, K. (2020). The formation of a metalimnetic oxygen minimum exemplifies how ecosystem dynamics shape biogeochemical processes: A modelling study. *Water Research*, *175*, 115701. https://doi.org/10.1016/j.watres.2020.115701

Miao, S., DeLaune, R. D., & Jugsujinda, A. (2006). Influence of sediment redox conditions on release/solubility of metals and nutrients in a Louisiana Mississippi River deltaic plain freshwater lake. *Science of The Total Environment*, *371*(1–3), 334–343. https://doi.org/10.1016/j.scitotenv.2006.07.027

Miranda, R. D. Q., Galvíncio, J. D., Moura, M. S. B. D., Jones, C. A., & Srinivasan, R. (2017). Reliability of MODIS Evapotranspiration Products for Heterogeneous Dry Forest: A Study Case of Caatinga. *Advances in Meteorology*, *2017*, 1–14. https://doi.org/10.1155/2017/9314801

Mocko, D. M., Kumar, S. V., Peters-Lidard, C. D., & Wang, S. (2021). Assimilation of Vegetation Conditions Improves the Representation of Drought over Agricultural Areas. *Journal of Hydrometeorology*, *22*(5), 1085–1098. https://doi.org/10.1175/JHM-D-20-0065.1

Molot, L. A., Watson, S. B., Creed, I. F., Trick, C. G., McCabe, S. K., Verschoor, M. J., Sorichetti, R. J., Powe, C., Venkiteswaran, J. J., & Schiff, S. L. (2014). A novel model for cyanobacteria bloom formation: The critical role of anoxia and ferrous iron. *Freshwater Biology*, *59*(6), 1323–1340. https://doi.org/10.1111/fwb.12334

Mortimer, C. H. (1941). The Exchange of Dissolved Substances Between Mud and Water in Lakes. *The Journal of Ecology*, *29*(2), 147–201. https://doi.org/10.2307/2256395

Mosher, T. D. (2000). *Assessment of a 254-mm minimum length limit for crappie in three northeastern Kansas reservoirs*. Kansas Department of Wildlife and Parks, Federal Aid in Sport Fish and Wildlife Restoration.

Myneni, R., Knyazikhin, Y., & Park, T. (2015). *MOD15A2H MODIS Leaf Area Index/FPAR 8-Day L4 Global 500m SIN Grid V006* (NASA EOSDIS Land Processes DAAC).

Nash, J. E., & Sutcliffe, J. V. (1970). River flow forecasting through conceptual models part I — A discussion of principles. *Journal of Hydrology*, *10*(3), 282–290. https://doi.org/10.1016/0022-1694(70)90255-6

Nealson, K. H., & Saffarini, D. (1994). IRON AND MANGANESE IN ANAEROBIC RESPIRATION: Environmental Significance, Physiology, and Regulation. *Annual Review of Microbiology*, *48*(1), 311–343. https://doi.org/10.1146/annurev.mi.48.100194.001523

Niu, G.-Y., Yang, Z.-L., Dickinson, R. E., & Gulden, L. E. (2005). A simple TOPMODEL-based runoff parameterization (SIMTOP) for use in global climate models. *Journal of Geophysical Research*, *110*(D21), D21106. https://doi.org/10.1029/2005JD006111

Niu, G.-Y., Yang, Z.-L., Mitchell, K. E., Chen, F., Ek, M. B., Barlage, M., Kumar, A., Manning, K., Niyogi, D., Rosero, E., Tewari, M., & Xia, Y. (2011). The community Noah land surface model with multiparameterization options (Noah-MP): 1. Model description and evaluation with local-scale measurements. *Journal of Geophysical Research*, *116*(D12), D12109. https://doi.org/10.1029/2010JD015139

Nõges, P., Nõges, T., Ghiani, M., Paracchini, B., Pinto Grande, J., & Sena, F. (2011). Morphometry and trophic state modify the thermal response of lakes to meteorological forcing. *Hydrobiologia*, *667*(1), 241–254. https://doi.org/10.1007/s10750-011-0691-7

Norgbey, E., Li, Y., Zhu, Y., Nwankwegu, A. S., Bofah-Buah, R., & Nuamah, L. (2021). Seasonal dynamics of iron and phosphorus in reservoir sediments in Eucalyptus plantation region. *Ecological Processes*, *10*(1), 10. https://doi.org/10.1186/s13717-021-00280-x

Nwosu, E. C., Roeser, P., Yang, S., Ganzert, L., Dellwig, O., Pinkerneil, S., Brauer, A., Dittmann, E., Wagner, D., & Liebner, S. (2021). From Water into Sediment—Tracing Freshwater Cyanobacteria via DNA Analyses. *Microorganisms*, *9*(8), 1778. https://doi.org/10.3390/microorganisms9081778

Oliver, R. L., Hamilton, D. P., Brookes, J. D., & Ganf, G. G. (2012). Physiology, Blooms and Prediction of Planktonic Cyanobacteria. In B. A. Whitton (Ed.), *Ecology of Cyanobacteria II* (pp. 155–194). Springer Netherlands. https://doi.org/10.1007/978-94-007-3855-3_6

Orihel, D. M., & Rooney, R. C. (2012). A field-based technique for sediment incubation experiments. *Journal of Limnology*, *71*(1), 25. https://doi.org/10.4081/jlimnol.2012.e25

O'Sullivan, M., Smith, W. K., Sitch, S., Friedlingstein, P., Arora, V. K., Haverd, V., Jain, A. K., Kato, E., Kautz, M., Lombardozzi, D., Nabel, J. E. M. S., Tian, H., Vuichard, N., Wiltshire, A., Zhu, D., & Buermann, W. (2020). Climate-Driven Variability and Trends in Plant Productivity Over Recent Decades Based on Three Global Products. *Global Biogeochemical Cycles*, *34*(12). https://doi.org/10.1029/2020GB006613

Pace, M. L., Batt, R. D., Buelo, C. D., Carpenter, S. R., Cole, J. J., Kurtzweil, J. T., & Wilkinson, G. M. (2017). Reversal of a cyanobacterial bloom in response to early warnings. *Proceedings of the National Academy of Sciences*, *114*(2), 352–357. https://doi.org/10.1073/pnas.1612424114

Paerl, H. (2014). Mitigating Harmful Cyanobacterial Blooms in a Human- and Climatically-Impacted World. *Life*, *4*(4), 988–1012. https://doi.org/10.3390/life4040988

Page, Martin, MacAllister, B., Urban, A., Veinotte, C., MacAllister, I., Pokrzywinski, K., Riley, J., Martinez-Guerra, E., White, C., Grasso, C., Kennedy, A., Thomas, C., Billing, J., Schmidt, A., Colona, B., Pinelli, D., John, C., & Levy, D. (2020). *Harmful Algal Bloom Interception, Treatment, and Transformation System, HABITATS: Pilot Research Study Phase I Summer 2019*.

Pearson, R. K. (2002). Outliers in process modeling and identification. *IEEE Transactions on Control Systems Technology*, *10*(1), 55–63. https://doi.org/10.1109/87.974338

Piccioni, F., Casenave, C., Lemaire, B. J., Le Moigne, P., Dubois, P., & Vinçon-Leite, B. (2021). The thermal response of small and shallow lakes to climate change: New insights from 3D hindcast modelling. *Earth System Dynamics*, *12*(2), 439–456. https://doi.org/10.5194/esd-12-439-2021

Pilla, R. M., Williamson, C. E., Zhang, J., Smyth, R. L., Lenters, J. D., Brentrup, J. A., Knoll, L. B., & Fisher, T. J. (2018). Browning-Related Decreases in Water Transparency Lead to Long-Term Increases in Surface Water Temperature and Thermal Stratification in Two Small Lakes. *Journal of Geophysical Research: Biogeosciences*, *123*(5), 1651–1665. https://doi.org/10.1029/2017JG004321

Pitman, A. J. (2003). The evolution of, and revolution in, land surface schemes designed for climate models. *International Journal of Climatology*, *23*(5), 479–510. https://doi.org/10.1002/joc.893

Pu, J., Yan, K., Zhou, G., Lei, Y., Zhu, Y., Guo, D., Li, H., Xu, L., Knyazikhin, Y., & Myneni, R. B. (2020). Evaluation of the MODIS LAI/FPAR Algorithm Based on 3D-RTM

Simulations: A Case Study of Grassland. *Remote Sensing*, *12*(20), 3391. https://doi.org/10.3390/rs12203391

R Core Team. (2018). *R: A language and environment for statistical computing. R Foundation for Statistical Computing* [Computer software]. https://www.R-project.org/

R Development Core Team. (2008). *A language and environment for statistical computing. R Foundation for Statistical Computing*. http://www.R-project.org/

Rahmani, V., Kastens, J., deNoyelles, F., Jakubauskas, M., Martinko, E., Huggins, D., Gnau, C., Liechti, P., Campbell, S., Callihan, R., & Blackwood, A. (2018). Examining Storage Capacity Loss and Sedimentation Rate of Large Reservoirs in the Central U.S. Great Plains. *Water*, *10*(2), 190. https://doi.org/10.3390/w10020190

Read, J. S., Hamilton, D. P., Jones, I. D., Muraoka, K., Winslow, L. A., Kroiss, R., Wu, C. H., & Gaiser, E. (2011). Derivation of lake mixing and stratification indices from high-resolution lake buoy data. *Environmental Modelling & Software*, *26*(11), 1325–1336. https://doi.org/10.1016/j.envsoft.2011.05.006

Read, J. S., Winslow, L. A., Hansen, G. J. A., Van Den Hoek, J., Hanson, P. C., Bruce, L. C., & Markfort, C. D. (2014). Simulating 2368 temperate lakes reveals weak coherence in stratification phenology. *Ecological Modelling*, *291*, 142–150. https://doi.org/10.1016/j.ecolmodel.2014.07.029

Reichstein, M., Falge, E., Baldocchi, D., Papale, D., Aubinet, M., Berbigier, P., Bernhofer, C., Buchmann, N., Gilmanov, T., Granier, A., Grunwald, T., Havrankova, K., Ilvesniemi, H., Janous, D., Knohl, A., Laurila, T., Lohila, A., Loustau, D., Matteucci, G., … Valentini, R. (2005). On the separation of net ecosystem exchange into assimilation and ecosystem respiration: Review and improved algorithm. *Global Change Biology*, *11*(9), 1424–1439. https://doi.org/10.1111/j.1365-2486.2005.001002.x

Reynolds, C. S., Oliver, R. L., & Walsby, A. E. (1987). Cyanobacterial dominance: The role of buoyancy regulation in dynamic lake environments. *New Zealand Journal of Marine and Freshwater Research*, *21*(3), 379–390. https://doi.org/10.1080/00288330.1987.9516234

Robertson, D. M., Juckem, P. F., Dantoin, E. D., & Winslow, L. A. (2018). Effects of water level and climate on the hydrodynamics and water quality of Anvil Lake, Wisconsin, a shallow seepage lake. *Lake and Reservoir Management*, *34*(3), 211–231. https://doi.org/10.1080/10402381.2017.1412374

Roy Chowdhury, T., Lee, J.-Y., Bottos, E. M., Brislawn, C. J., White, R. A., Bramer, L. M., Brown, J., Zucker, J. D., Kim, Y.-M., Jumpponen, A., Rice, C. W., Fansler, S. J., Metz, T. O., McCue, L. A., Callister, S. J., Song, H.-S., & Jansson, J. K. (2019). Metaphenomic Responses of a Native Prairie Soil Microbiome to Moisture Perturbations. *MSystems*, *4*(4), e00061-19. https://doi.org/10.1128/mSystems.00061-19

Running, S., Mu, Q., & Zhao, M. (2015). *MODIS/Terra Gross Primary Productivity 8-Day L4 Global 500m SIN Grid V061* [dataset]. NASA EOSDIS Land Processes DAAC. https://doi.org/10.5067/MODIS/MOD17A2H.061

Running, S., Mu, Q., & Zhao, M. (2021). *MODIS/Terra Net Evapotranspiration 8-Day L4 Global 500m SIN Grid V061* [dataset]. NASA EOSDIS Land Processes DAAC. https://doi.org/10.5067/MODIS/MOD16A2.061

Schlesinger, W. H., & Jasechko, S. (2014). Transpiration in the global water cycle. *Agricultural and Forest Meteorology*, *189–190*, 115–117. https://doi.org/10.1016/j.agrformet.2014.01.011

Sehgal, V., & Sridhar, V. (2019). Watershed-scale retrospective drought analysis and seasonal forecasting using multi-layer, high-resolution simulated soil moisture for Southeastern U.S. *Weather and Climate Extremes*, *23*, 100191. https://doi.org/10.1016/j.wace.2018.100191

Sheffield, J., Barrett, A. P., Colle, B., Nelun Fernando, D., Fu, R., Geil, K. L., Hu, Q., Kinter, J., Kumar, S., Langenbrunner, B., Lombardo, K., Long, L. N., Maloney, E., Mariotti, A., Meyerson, J. E., Mo, K. C., David Neelin, J., Nigam, S., Pan, Z., … Yin, L. (2013). North American Climate in CMIP5 Experiments. Part I: Evaluation of Historical Simulations of Continental and Regional Climatology. *Journal of Climate*, *26*(23), 9209–9245. https://doi.org/10.1175/JCLI-D-12-00592.1

Singh, P., Bagrania, J., & Haritash, A. K. (2019). Seasonal behaviour of thermal stratification and trophic status in a sub-tropical Palustrine water body. *Applied Water Science*, *9*(5), 139. https://doi.org/10.1007/s13201-019-1011-z

Smith, V. H. (1983). Low Nitrogen to Phosphorus Ratios Favor Dominance by Blue-Green Algae in Lake Phytoplankton. *Science*, *221*(4611), 669–671. https://doi.org/10.1126/science.221.4611.669

Smolders, A. J. P., Lamers, L. P. M., Lucassen, E. C. H. E. T., Van Der Velde, G., & Roelofs, J. G. M. (2006). Internal eutrophication: How it works and what to do about it—a review. *Chemistry and Ecology*, *22*(2), 93–111. https://doi.org/10.1080/02757540600579730

Sommer, U., Adrian, R., De Senerpont Domis, L., Elser, J. J., Gaedke, U., Ibelings, B., Jeppesen, E., Lürling, M., Molinero, J. C., Mooij, W. M., Van Donk, E., & Winder, M. (2012). Beyond the Plankton Ecology Group (PEG) Model: Mechanisms Driving Plankton

Succession. *Annual Review of Ecology, Evolution, and Systematics*, *43*(1), 429–448. https://doi.org/10.1146/annurev-ecolsys-110411-160251

Søndergaard, M., Jensen, J. P., & Jeppesen, E. (2003). Role of sediment and internal loading of phosphorus in shallow lakes. *Hydrobiologia*, *506–509*(1–3), 135–145. https://doi.org/10.1023/B:HYDR.0000008611.12704.dd

Song, J., Her, Y., & Kang, M. (2022). Estimating Reservoir Inflow and Outflow From Water Level Observations Using Expert Knowledge: Dealing With an Ill-Posed Water Balance Equation in Reservoir Management. *Water Resources Research*, *58*(4), e2020WR028183. https://doi.org/10.1029/2020WR028183

Song, K., Xenopoulos, M. A., Buttle, J. M., Marsalek, J., Wagner, N. D., Pick, F. R., & Frost, P. C. (2013). Thermal stratification patterns in urban ponds and their relationships with vertical nutrient gradients. *Journal of Environmental Management*, *127*, 317–323. https://doi.org/10.1016/j.jenvman.2013.05.052

Stefan, H. G., Hondzo, M., Fang, X., Eaton, J. G., & McCormick, J. H. (1996). Simulated long term temperature and dissolved oxygen characteristics of lakes in the north-central United States and associated fish habitat limits. *Limnology and Oceanography*, *41*(5), 1124–1135. https://doi.org/10.4319/lo.1996.41.5.1124

Su, L., Cao, Q., Xiao, M., Mocko, D. M., Barlage, M., Li, D., Peters-Lidard, C. D., & Lettenmaier, D. P. (2021). Drought Variability over the Conterminous United States for the Past Century. *Journal of Hydrometeorology*, *22*(5), 1153–1168. https://doi.org/10.1175/JHM-D-20-0158.1

Tavakol, A., Rahmani, V., & Harrington Jr., J. (2020). Probability of compound climate extremes in a changing climate: A copula-based study of hot, dry, and windy events in the central United States. *Environmental Research Letters*, *15*(10), 104058. https://doi.org/10.1088/1748-9326/abb1ef

Therneau, T., Atkinson, B., & Ripley, B. (2019). *Recursive partitioning and regression trees. R package version 4.1–13* [Computer software]. https://CRAN. R-project. org/package= rpart

Thornton, K. W. (1990). Perspectives on reservoir limnology. In *Reservoir Limnology: Ecological Perspectives* (pp. 1–13).

Wagle, P., Xiao, X., Scott, R. L., Kolb, T. E., Cook, D. R., Brunsell, N., Baldocchi, D. D., Basara, J., Matamala, R., Zhou, Y., & Bajgain, R. (2015). Biophysical controls on carbon and water vapor fluxes across a grassland climatic gradient in the United States. *Agricultural and Forest Meteorology*, *214–215*, 293–305. https://doi.org/10.1016/j.agrformet.2015.08.265

Wagner, T., & Erickson, L. E. (2017). Sustainable Management of Eutrophic Lakes and Reservoirs. *Journal of Environmental Protection*, *08*(04), 436–463. https://doi.org/10.4236/jep.2017.84032

Waldo, S., Beaulieu, J. J., Barnett, W., Balz, D. A., Vanni, M. J., Williamson, T., & Walker, J. T. (2021). *Temporal patterns and biophysical controls on methane emissionsfrom a small eutrophic reservoir: Insights from two years of eddycovariance monitoring* [Preprint]. Biogeochemistry: Greenhouse Gases. https://doi.org/10.5194/bg-2021-36

Weber, M., Rinke, K., Hipsey, M. R., & Boehrer, B. (2017). Optimizing withdrawal from drinking water reservoirs to reduce downstream temperature pollution and reservoir hypoxia. *Journal of Environmental Management*, *197*, 96–105. https://doi.org/10.1016/j.jenvman.2017.03.020

Wei, J., Dirmeyer, P. A., Guo, Z., Zhang, L., & Misra, V. (2010). How Much Do Different Land Models Matter for Climate Simulation? Part I: Climatology and Variability. *Journal of Climate*, *23*(11), 3120–3134. https://doi.org/10.1175/2010JCLI3177.1

Wei, T., Simko, V., Levy, M., Xie, Y., Jin, Y., & Zemla, J. (2017). *corrplot: Visualization of a Correlation Matrix* (0.84) [Computer software]. https://CRAN.R-project.org/package=corrplot

Wei, Z., Yoshimura, K., Wang, L., Miralles, D. G., Jasechko, S., & Lee, X. (2017). Revisiting the contribution of transpiration to global terrestrial evapotranspiration: Revisiting Global ET Partitioning. *Geophysical Research Letters*, *44*(6), 2792–2801. https://doi.org/10.1002/2016GL072235

Welch, E. B., & Cooke, G. D. (2005). Internal Phosphorus Loading in Shallow Lakes: Importance and Control. *Lake and Reservoir Management*, *21*(2), 209–217. https://doi.org/10.1080/07438140509354430

Wilhelm, S., & Adrian, R. (2007). Impact of summer warming on the thermal characteristics of a polymictic lake and consequences for oxygen, nutrients and phytoplankton. *Freshwater Biology*, *0*(0), 226–237. https://doi.org/10.1111/j.1365-2427.2007.01887.x

Williamson, C. E., Saros, J. E., Vincent, W. F., & Smol, J. P. (2009). Lakes and reservoirs as sentinels, integrators, and regulators of climate change. *Limnology and Oceanography*, *54*, 2273–2282. https://doi.org/10.4319/lo.2009.54.6_part_2.2273

Willmott, C., & Matsuura, K. (2005). Advantages of the mean absolute error (MAE) over the root mean square error (RMSE) in assessing average model performance. *Climate Research*, *30*, 79–82. https://doi.org/10.3354/cr030079

Winder, M., & Sommer, U. (2012). Phytoplankton response to a changing climate. *Hydrobiologia*, *698*(1), 5–16. https://doi.org/10.1007/s10750-012-1149-2

Winslow, L. A., Hansen, G. J. A., Read, J. S., & Notaro, M. (2017). Large-scale modeled contemporary and future water temperature estimates for 10774 Midwestern U.S. Lakes. *Scientific Data*, *4*(1), 170053. https://doi.org/10.1038/sdata.2017.53

Winslow, L., Read, J., Woolway, R., Brentrup, J., Leach, T., Zwart, J., Albers, S., & Collinge, D. (2018). *RLakeAnalyzer: Lake Physics Tools. R package version 1.11.4* (1.11.4) [Computer software]. https://CRAN.R-project.org/package=rLakeAnalyzer

Wolf, S., Keenan, T. F., Fisher, J. B., Baldocchi, D. D., Desai, A. R., Richardson, A. D., Scott, R. L., Law, B. E., Litvak, M. E., Brunsell, N. A., Peters, W., & Van Der Laan-Luijkx, I. T. (2016). Warm spring reduced carbon cycle impact of the 2012 US summer drought. *Proceedings of the National Academy of Sciences*, *113*(21), 5880–5885. https://doi.org/10.1073/pnas.1519620113

Woolway, R. I., Meinson, P., Nõges, P., Jones, I. D., & Laas, A. (2017). Atmospheric stilling leads to prolonged thermal stratification in a large shallow polymictic lake. *Climatic Change*, *141*(4), 759–773. https://doi.org/10.1007/s10584-017-1909-0

Woolway, R. I., & Merchant, C. J. (2019). Worldwide alteration of lake mixing regimes in response to climate change. *Nature Geoscience*, *12*(4), 271–276. https://doi.org/10.1038/s41561-019-0322-x

Wurtsbaugh, W. A., Paerl, H. W., & Dodds, W. K. (2019). Nutrients, eutrophication and harmful algal blooms along the freshwater to marine continuum. *WIREs Water*, *6*(5). https://doi.org/10.1002/wat2.1373

Xia, Y., Mitchell, K., Ek, M., Sheffield, J., Cosgrove, B., Wood, E., Luo, L., Alonge, C., Wei, H., Meng, J., Livneh, B., Lettenmaier, D., Koren, V., Duan, Q., Mo, K., Fan, Y., & Mocko, D. (2012). Continental-scale water and energy flux analysis and validation for the North American Land Data Assimilation System project phase 2 (NLDAS-2): 1. Intercomparison and application of model products: WATER AND ENERGY FLUX ANALYSIS. *Journal of Geophysical Research: Atmospheres*, *117*(D3), n/a-n/a. https://doi.org/10.1029/2011JD016048

Xinyou, Y., & Van Laar, H. H. (2005). *Crop systems dynamics: An ecophysiological simulation model of genotype-by-environment interactions*. Wageningen Academic Publishers.

Yang, Z.-L., Niu, G.-Y., Mitchell, K. E., Chen, F., Ek, M. B., Barlage, M., Longuevergne, L., Manning, K., Niyogi, D., Tewari, M., & Xia, Y. (2011). The community Noah land surface model with multiparameterization options (Noah-MP): 2. Evaluation over global river basins. *Journal of Geophysical Research*, *116*(D12), D12110. https://doi.org/10.1029/2010JD015140

Yuan, X., Roundy, J. K., Wood, E. F., & Sheffield, J. (2015). Seasonal Forecasting of Global Hydrologic Extremes: System Development and Evaluation over GEWEX Basins. *Bulletin of the American Meteorological Society*, *96*(11), 1895–1912. https://doi.org/10.1175/BAMS-D-14-00003.1

Zarfl, C., Lumsdon, A. E., Berlekamp, J., Tydecks, L., & Tockner, K. (2015). A global boom in hydropower dam construction. *Aquatic Sciences*, *77*(1), 161–170. https://doi.org/10.1007/s00027-014-0377-0

Zheng, D., Van Der Velde, R., Su, Z., Wang, X., Wen, J., Booij, M. J., Hoekstra, A. Y., & Chen, Y. (2015a). Augmentations to the Noah Model Physics for Application to the Yellow

River Source Area. Part I: Soil Water Flow. *Journal of Hydrometeorology*, *16*(6), 2659–2676. https://doi.org/10.1175/JHM-D-14-0198.1

Zheng, D., Van Der Velde, R., Su, Z., Wang, X., Wen, J., Booij, M. J., Hoekstra, A. Y., & Chen, Y. (2015b). Augmentations to the Noah Model Physics for Application to the Yellow River Source Area. Part II: Turbulent Heat Fluxes and Soil Heat Transport. *Journal of Hydrometeorology*, *16*(6), 2677–2694. https://doi.org/10.1175/JHM-D-14-0199.1

Zhou, Y., & McArdle, J. J. (2015). Rationale and Applications of Survival Tree and Survival Ensemble Methods. *Psychometrika*, *80*(3), 811–833. https://doi.org/10.1007/s11336-014-9413-1